Structure and dynamics of hydrogen in nanocomposite solid acids for fuel cell applications

The research described in this thesis was part of the Delft Institute for Sustainable Energy, performed in the Department of Fundamental Aspects of Materials and Energy at the faculty of Applied Sciences, Delft University of Technology, Mekelweg 15, 2629 JB Delft, The Netherlands.

Structure and dynamics of hydrogen in nanocomposite solid acids for fuel cell applications

PROEFSCHRIFT

ter verkrijging van de graad van doctor
aan de Technische Universiteit Delft,
op gezag van de Rector Magnificus prof. ir. K.C.A.M. Luyben,
voorzitter van het College voor Promoties,
in het openbaar te verdedigen op dinsdag 7 juni 2011 om 12:30 uur

door

Wing Kee CHAN
scheikundig ingenieur
geboren te Hong Kong, China.

Dit proefschrift is goedgekeurd door de promotor:
Prof. dr. F.M. Mulder

Samenstelling promotiecommissie:

Rector Magnificus	voorzitter
Prof. Dr. F.M. Mulder	Technische Universiteit Delft, promotor
Prof. Dr. E.H. Brück	Technische Universiteit Delft
Prof. Dr. S.J. Picken	Technische Universiteit Delft
Prof. Dr. T.J. Dingemans	Technische Universiteit Delft
Prof. Dr. A.P.M. Kentgens	Radboud Universiteit Nijmegen
Prof. Dr. F.A. de Bruijn	Rijks Universiteit Groningen
Prof. Dr. M.R. Johnson	Institut Laue-Langevin, Frankrijk

ISBN 978-90-5335-423-0

Ridderprint Offsetdrukkerij BV
Pottenbakkerstraat 17
2984 AX RIDDERKERK
The Netherlands
Telephone: +31 180 463962
Telefax: +31 180 415471
E-mail: info@proefschriftdrukken.nl

Printed in The Netherlands

Propositions

The propositions accompanying the thesis: *Structure and dynamics of hydrogen in nanocomposite solid acids for fuel cell applications* by Wing Kee Chan

1. In a nanostructured composite with a proton acceptor, the crystalline phase of the solid acid is destabilized, resulting in a partial transition to an amorphous phase.
2. The extent of space charge effects in the solid acid nanocomposites can be estimated through the relative acidity of the composite materials.
3. Proton mobility in the space charge affected crystalline solid acid phase is similar to the proton mobility of the X-ray amorphous phase and as such, both phases contribute significantly to the increase in mobility.
4. Besides increasing the conductivity, solid acid impregnated in Nafion also physically supports the channels, preventing their collapse during dehydration.
5. The hydrogen economy is not threatened by the advances of electricity storage in batteries. Both means of energy storage will coexist, facilitating the implementation of both techniques in e.g. vehicles.
6. Concerning energy in general, most people are reluctant to make concessions. Taking the path of least resistance, one tends to give them what they want, even if it's for luxurious applications.
7. During the initial screening of the potential candidate for the civic integration course the background should also be taken into account. As a result, the people who will not benefit from the course should be sent to a more proper course, usually just a language course.
8. Timedependent effects of nanostructured materials sometimes have a significant impact on certain properties, they are often overlooked.
9. The space charge effect should be used, among others, in battery research since it can have larger impact than generally assumed.

These propositions are considered opposable and defendable and have been approved as such by the supervisor Prof. dr. F.M. Mulder

Stellingen

Stellingen behorend by het proefschrift: *Structure and dynamics of hydrogen in nanocomposite solid acids for fuel cell applications* door Wing Kee Chan

1. In een nanogestructureerd composiet met een proton acceptor, is het kristallijne deel van de solid acid fase gedestabiliseerd, wat resulteert in een gedeeltelijke overgang naar een amorfe fase.
2. De mate van space charge effecten in de solid acid nanocomposieten kan worden geschat via de relatieve zuurgraad van de composiet materialen.
3. Proton mobiliteit in de space charge beïnvloedde kristallijne solid acid fase is vergelijkbaar met de proton mobiliteit van de Röntgen straling amorfe fase en als zodanig, dragen beide fasen significant bij aan de toename in mobiliteit.
4. Naast het verhogen van de geleiding, ondersteunt de solid acid fase geïmpregneerd in Nafion tevens fysiek de kanalen, wat instorting voorkomt tijdens dehydratatie.
5. De waterstof economie wordt niet bedreigd door de vooruitgang van elektriciteitsopslag in batterijmaterialen. Beide middelen van energie-opslag zullen naast elkaar blijven bestaan, wat de implementatie van deze technieken in bijvoorbeeld voertuigen zal faciliteren.
6. Met betrekking tot energie in het algemeen, zijn de meeste mensen onwillig consessies te doen. De weg van de minste weerstand nemend, is men geneigd hen te geven wat ze willen, zelfs al is het voor luxe toepassingen.
7. Tijdens de eerste screening van de potentiële kandidaat voor de inburgeringscursus, moet ook rekening gehouden worden met de achtergrond. Als gevolg hiervan moeten de mensen voor wie de cursus niet nuttig zal zijn doorverwezen worden naar een meer passende cursus, wat meestal slechts een taalcursus betreft.
8. Tijdsafhankelijke effecten van nanogestructureerde materialen hebben soms een aanzienlijke invloed op bepaalde eigenschappen, deze worden vaak over het hoofd gezien.
9. Het space charge effect zou gebruikt moeten worden in onder andere batterijonderzoek, omdat het een groter effect zou kunnen hebben dan in het algemeen aangenomen wordt.

Deze stellingen worden opponeerbaar en verdedigbaar geacht en zijn als zodanig goedgekeurd door de promotor Prof. dr. F.M. Mulder

Dedicated to my Wife Wing, my son Sven and my parents.

Table of Contents

Chapter 1.

Introduction

1.1. General introduction

Many people might not realize this, but we are living in exciting times. We are on the verge of a great change in the way we supply ourselves with energy; the transition from fossil fuels to sustainable sources. If everything goes well, we could consider ourselves fortunate to be part of this historical period. The first usage of coal was recorded as being in the year 2000 BC in China [1]. In the long period up to the present day, fossil fuels have become of increasing importance to the point where it currently dominates our way of life and where we are fully dependent on them. However, the dominance of fossil fuels and especially petroleum is necessarily limited. An inevitably transition from non-renewable to renewable energy sources has to take place. A bright future awaits us where our energy is locally generated from sustainable sources such as solar, wind, hydro and geothermal energy and when necessary stored in hydrogen to be converted back by fuel cells when the need is there. Note that hydrogen is acting as a carrier of energy. The sustainability comes from the sources mentioned above and the abundance of water. This will fundamentally change the society we have created and lived in for the past decades, just as coal and steam did at the beginning of the industrial revolution. However, before reaching that stage there is still much research and development required to facilitate the implementation of renewable energies.

People talk about problems arising in our future fossil based fuel supply, but what are exactly the problems? Fossil fuels lead to climate change, air pollution, and depletion of natural resources. Furthermore, supply shortages, volatile fuel prices and dependence on politically instable countries complicate the matter. Fossil fuels are non-renewable resources, meaning that once they are used they cannot be

replaced or recreated on human timescales. They also present environmental problems during their extraction and transportation, well displayed in April 2010 when a BP oil rig exploded resulting in one of the largest oil spills in history.
Arguing that implementing a hydrogen economy will solve all energy and environmental problems would not be (fully) correct. In truth the matter is much more complex; as the hydrogen needs to be produced in a sustainable and clean way and no exotic, dangerous or environmentally unfriendly materials must be used in the whole trajectory from production till the end usage of the energy. Furthermore, there are issues with energy efficiencies at hand. That said it is still very crucial that a transition to a more sustainable energy infrastructure has to happen in the nearby future.
With such a complex challenge, the solution is so too. It is not possible to propose a single solution for the whole problem, but instead each section of the problem has to be solved separately. One of the large contributors to our problem lies in the transportation sector. More than one third of the global energy use comes from oil and a large part of this oil goes into the transportation sector. Our discussion in this thesis will therefore be referring to the automotive sector with the larger context that if great improvements can be made there, these will easily be transferable to stationary environments.

1.2. Fuel cells

Short history
In 1800 William Nicholson and Anthony Carlisle successfully electrolyzed water using Alessandro Volta's voltaic pile. William Robert Grove reversed this process in 1838 using platinum electrodes with one end immersed in a container of sulfuric acid and the other ends separately sealed in containers of oxygen and hydrogen. The sealed containers held water as well as the gases, and he noted that the water level rose in both tubes as a current flowed between the electrodes. By combining several sets of these electrodes in a series circuit, he created what he called a "gas battery"- the first fuel cell (figure 1.1).

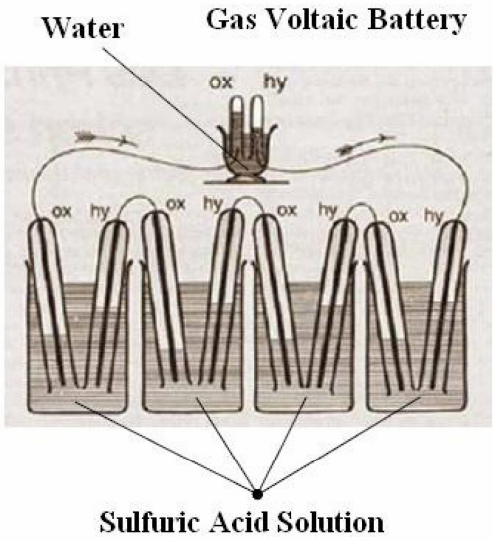

Figure 1.1. The Grove Cell.
Source: [2]

Francis Thomas Bacon began researching alkali electrolyte fuel cells in the late 1930s, which resulted in an initial cell in 1939. In 1955 Willard Thomas Grubb and in 1958 Leonard Niedrach made final modifications to the original alkali fuel cell, nowadays known as the 'Grubb-Niedrach' fuel cell, leading to the first commercial use of the fuel cell in the Gemini space project. In the 1960s, Pratt and Whitney licensed Bacon's patents for use in the Apollo spacecraft to supply electricity and drinking water. During the 1980s, fuel cell technology began to be tested by utilities and automobile manufacturers. Technical breakthroughs during the decade resulted in the first marketable fuel cell-powered vehicle in 1993 by Ballard. Nowadays many fuel cell projects are running and developments on fuel cell powered vehicles are done all over the world. Amongst these is the Honda FCX lease program in California. The FCX Clarity is currently available in Southern California, where plenty of hydrogen refilling stations are available. As of 2010, 19 FCXs are being leased and will increase to a total of 50 with the prospect of expanding to 200 vehicles in the next year.

The fuel cell concept

There are many types of fuel cells. The principle is however generally the same. Hydrogen enters at the anode side, diffuses to the catalyst and dissociates into protons and electrons. The protons conduct through the membrane to the cathode and the electrons are forced through an external circuit because the electrolyte is

electrically insulating. While going through this electrical circuit, it supplies power to the external devices connected to this circuit. Oxygen enters at the cathode side, where it combines with the electrons from the external circuit and the protons that travelled through the electrolyte to form water. A schematic representation of the fuel cell is shown in figure 1.2. The electrolyte plays an important role in this process. It should block electrons and other substances and only allow the appropriate ions to pass with as little resistance as possible.

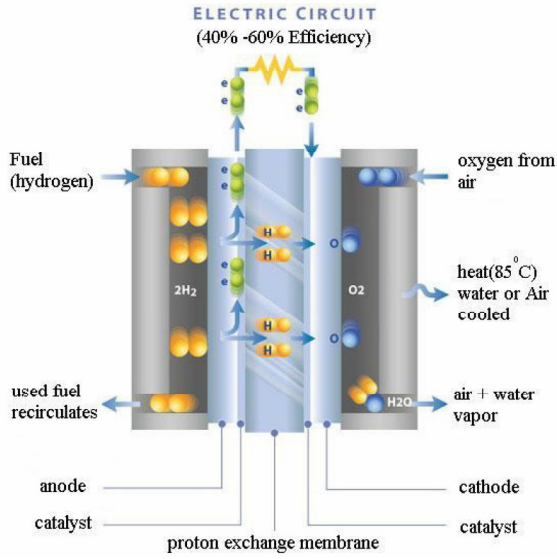

Figure 1.2. Principle of the fuel cell.
Source: [3]

Types of fuel cells [4, 5]
Alkaline fuel cell, AFC. The electrolyte of the AFC consists of potassium hydroxide in water. Effectively OH^- ions and H_2O are being transported through the electrolyte. The operating temperature is between 80 °C and 200 °C. The AFC is being used for power generation on spacecrafts. The use of AFC's is limited because of its high sensitivity to CO_2 (the hydroxides react with CO_2 to precipitate carbonates), which makes it necessary to purify both the hydrogen and oxygen used in the cell.

Proton exchange membrane fuel cell, PEMFC. PEM fuel cells, also called polymer electrolyte membrane fuel cells, are capable to deliver high power density. They possess relatively low weight and volume compared with other fuel cells, fast startup times, low sensitivity to orientation and favorable power-to-weight ratio, making them ideal for transport applications. PEM fuel cells usually have a solid polymer as electrolyte, such as the commercially very successful Nafion, with protons attached

to H_2O (i.e. H_3O^+) being the ions transported. Because it uses liquid H_2O as a vehicle to transport the protons, the operating temperature should remain below 100 °C and normally is around 80 ^{0}C. The PEMFC is sensitive towards impurities in the fuel as it requires a noble metal (platinum) as catalyst in the electrode, which is extremely sensitive to CO poisoning.

Direct methanol fuel cell, DMFC. The DMFC is a variation of the PEMFC as it uses the same type of electrolyte. Instead of using hydrogen, methanol is mixed with steam and fed directly to the fuel cell anode, where the methanol is directly oxidized to CO_2. The major advantage of methanol over hydrogen is the ease of storage, transport and supply using the existing infrastructure. However, the efficiency of the fuel cell is low due to the high permeation of methanol through the electrolyte. This is known as methanol crossover. In addition the power density remains low. The half-reaction at the anode involves the consumption of water and the creation of CO_2, while water is produced at the cathode. This requires additional management of CO_2 and liquid H_2O. Furthermore, during the oxidation reaction of methanol CO is formed, resulting in poisoning of the platinum catalyst.

Phosphoric acid fuel cell, PAFC. PAFC use liquid phosphoric acid as electrolyte. The acid is contained in a Teflon-bonded silicon carbide matrix and the transported ions are protons. The operating temperature is around 200 ^{0}C. It is one of the most mature cell types and commercially the most successful at this moment. They are less sensitive to impurities in the fuel compared to the PEMFC. However, the aggressive medium used requires highly corrosion resistant materials, which results in larger and heavier fuel cells compared to the PEMFCs. The PAFCs are typically used for stationary power supply.

Molten carbonate fuel cell, MCFC. MCFCs are high-temperature fuel cells that use an electrolyte composed of a molten carbonate salt mixture suspended in a porous, chemically inert ceramic lithium aluminum oxide matrix. The conducting species here are CO_3^{2-} ions, effectively transporting oxygen molecules through the electrolyte. These ions combine with protons at the anode to form CO_2 and H_2O. The operating temperature is between 600 and 700 ^{0}C. Because of this, internal reforming of hydrocarbon fuels and the use of non precious metals as catalyst are possible. Also MCFCs are insensitive to carbon monoxide and carbon dioxide poisoning. The primary disadvantage of MCFCs is durability. The high temperatures and the corrosive electrolyte decrease cell life significantly.

Solid oxide fuel cell, SOFC. Yttrium stabilised zirconia is generally used as the solid electrolyte in the SOFC, with O^{2-} as the conducting species. Depending on the electrolyte and the electrodes, the SOFC can be operated between 600 ^{0}C and 1000 ^{0}C. Similar to the MCFC the high temperature removes the need for precious metal

catalyst and allows for internal fuel reforming. Fuels ranging from hydrogen to natural gas and higher hydrocarbons can be used. SOFCs are the most sulfur resistant fuel cell and are insensitive to carbon monoxide, which can even be used as fuel. The high temperature operation however, results in slow startups, durability issues and the need for significant thermal shielding, making them unsuitable for transportation and small portable applications.

Need for better electrolytes

Comparing the PEMFCs to the other types of fuel cells, the PEMFCs operate at much lower temperatures allowing rapid start-up, less stringent material requirements and longer life times. They have relative high efficiency, high power-to-weight ratio, are compact and lightweight, making them the most promising candidate for transportation purposes. However, the low operating temperature of the unit hinders useful cogeneration from waste heat and requires the use of expensive and CO sensitive catalysts such as platinum. Furthermore, optimal performance of the electrolyte requires saturation with water and therefore complex humidification systems. Going to intermediate temperatures, roughly around 120 ºC to 250 ºC would immediately solve some of the problems of the low temperature PEMFCs, without suffering from the problems that accompany high temperature (>600 ºC) operation. Intermediate temperatures come with the following advantages.

No humidification systems required. High temperature inherently excludes the use of liquid water based proton conduction mechanisms, essentially shifting to anhydrous proton conductors. This removes the need for complex humidifying units to keep the electrolyte humid. The only concern of water is with regard to exhaust water, which evaporates.

Improved CO tolerance. Catalyst poisoning occurs through adsorption of the CO on the platinum catalyst. At higher temperatures this adsorption is much less, improving tolerance of the catalyst to CO in the fuel with orders of magnitudes.

Easier heat management. As efficient as fuel cells are, still a large part of the energy is converted to heat. To prevent overheating of the fuel cell, this heat must be removed. As the rate of heat transport is proportional to the temperature difference, in this case with ambient temperature, operating at higher temperatures makes cooling much easier.

Heat recovery. Waste heat recovery at 80ºC is usually unrewarding. The costs are higher than what can be gained from this. Waste heat at higher temperatures can be recovered profitably and be reused for e.g. preheating the fuel or liberating the H_2 from a storage material, improving overall efficiency.

Cheaper and less sensitive catalysts. Higher temperatures lead to enhanced reaction kinetics, which allows the use of less reactive non platinum catalysts.

In summary, these improvements can result in a more compact and less complex fuel cell, which together will be easier and cheaper to produce, operate and maintain.

Therefore much research is being conducted to find the ideal electrolyte for operation at these intermediate temperatures, keeping in mind that also the startup at ambient temperature is important.

1.3. Solid acids

High protonic conduction at intermediate temperatures is found in solid acids, which are acids in the solid crystalline phase. Typical for these materials is a superprotonic phase transition after which the material shows a jump in protonic conductivity of orders of magnitudes. Above this phase transition, these materials have been shown to be applicable as fuel cell electrolyte. In spite of their acidic nature, these solid acids require no special heat or acid resistant construction materials. Solid acids generally can be represented with the chemical formula: $M_aH_b(XO4)_c$, where M is a mono- or divalent cation (e.g. Rb, Cs), XO_4 is a tetrahedral oxy-anion (e.g. SO_4, SeO_4, PO_4) and a, b, c, are integers.

Cesium Hydrogen Sulfate ($CsHSO_4$). One typical solid acid is Cesium Hydrogen Sulfate ($CsHSO_4$) [6]. Depending on the temperature, $CsHSO_4$ exhibits three crystalline phases, usually referred to phase III, II and I. Phase III and phase II are monoclinic, low proton conducting phases, with the differences being in the unit cell volume and the organization of hydrogen bonds. Bulk crystalline $CsHSO_4$ phase II is a metastable phase at room temperature, which will gradually fall back to Phase III. At 141°C $CsHSO_4$ goes through its superprotonic phase transition (from phase II to phase I) to a tetragonal phase, which has a higher crystal symmetry and also increased lattice dimensions. This allows for quasi free rotation of the SO_4^{2-} tetrahedra between crystallographically identical positions, creating six times as many possible proton sites as there are protons available. Proton diffusion occurs through combined rotation of the SO_4^{2-} group and jumps to the next SO_4^{2-} group. This fast process gives the material its high proton conductivity. Based on earlier studies on its conductivity, $CsHSO_4$ has been shown to be applicable as fuel cell electrolyte by Haile et al [7]. A first prototype fuel cell running at intermediate temperatures using $CsHSO_4$ as electrolyte was produced and operated sucessfully.

However, in the low temperature phases below 141°C, the number of protons is equal to the number of available proton sites. The hydrogen atoms are localized with rigid hydrogen bonds between SO_4^{2-} tetrahedral. In ionic materials the mobility of ions strongly depends on the number of available vacant sites to which an ion can move. This explains the low protonic conductivity in these phases. Clearly such low conductivity at ambient temperature is detrimental for the practical use starting from ambient temperature.

Cesium dihydrogen Phosphate (CsH_2PO_4). Another typical solid acid is CsH_2PO_4 [8]. This material sometimes is considered to possess even greater potential due to

its higher phase transition temperature at 230 °C to a cubic phase and the presence of 2 hydrogen atoms in the structure. The definitive confirmation came from Otomo et al showing a working fuel cell based on CsH_2PO_4 [9]. This fuel cell was operational between 230 °C and 300 °C. Besides the low conductivity of the low temperature phase, CsH_2PO_4 is subject to decomposition already at temperatures below its superprotonic phase transition [10]. The decomposition reaction is as follows:

$$nCsH_2PO_4 \Leftrightarrow Cs_nH_2P_nO_{3n+1} + (n-1)H_2O$$

With the most common decomposition product n=2 leading to cesium hydrogen pyrophosphate ($Cs_2H_2P_2O_7$), also referred to as simply pyrophosphate. This dehydration of CsH_2PO_4 can be partially suppressed by humidifying the atmosphere [11]. This would however require unwanted humidification systems.

1.4. Nanostructuring

Adding non-reactive and insulating phases, such as SiO_2, TiO_2, Al_2O_3 to solid acids (and ion conductors in general) initially have been done to improve its mechanical properties. The idea was to sacrifice some of the conductivity to achieve higher mechanical stability. Surprisingly it was observed that in some cases the conductivity of the low temperature phases was enhanced instead. The effect was most profound with the addition of nanoparticles. This nanostructuring is done by simply mixing the ionic conductor with nanoparticles, resulting in increased proton conductivity of orders of magnitude, as shown in figure 1.3. The smaller gap between the conductivity of the phases and the improved low temperature conductivity makes the solid acids even better suitable to be applied as electrolytes in fuel cells.

Still many aspects of nanostructuring remain unclear. It was found that many factors influence the increase in conductivity. These include the history of preparation, particle size of the nanoparticles, type of nanoparticles, the added amount of material and the humidity during operation. Furthermore the amount of amorphous phase formed during preparation is another matter of concern. Many models have been used in attempts to explain this phenomenon, but one in particular generating most interest, is referred to as the space charge model.

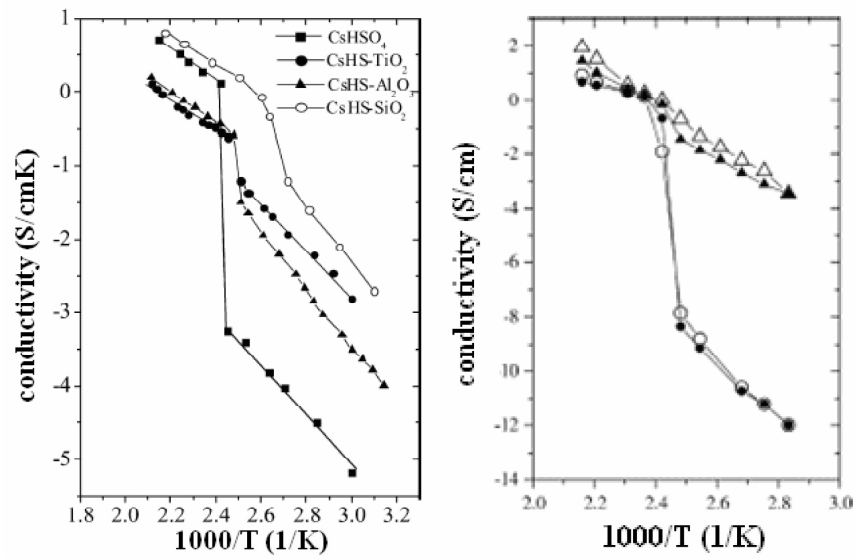

Figure 1.3. Conductivity of bulk and nanocomposite solid acids as function of temperature.
Source: left: [12], right: [13]

Space charge model in nanoionics

Where electro neutrality must be obeyed in bulk material, at interfaces of ionic conductors (or ionic conductor and insulator) a narrow charged zone can be thermodynamically favorable. This narrow charged zone extends to a few times the Debye length, which comes down to a few nanometers up to tens of nanometers and is referred to as space charge layer [14-19]. Due to the difference in chemical potential, mobile charge carriers of the ionic phase physically relocate themselves at the interface or in the alien phase, leaving vacancies in the donating phase. This leaves oppositely charged layers at the interface, resulting in an electric field, which limits the extent of the space charge layer. Upon nanostructuring materials, the distances of the interfaces approach the order of nanometers and the space charge layers overlap, as shown in figure 1.4. Material's properties, such as ionic densities and – most important for fuel cell electrolytes - conductivities are then dominated by the properties in the space charge layers.

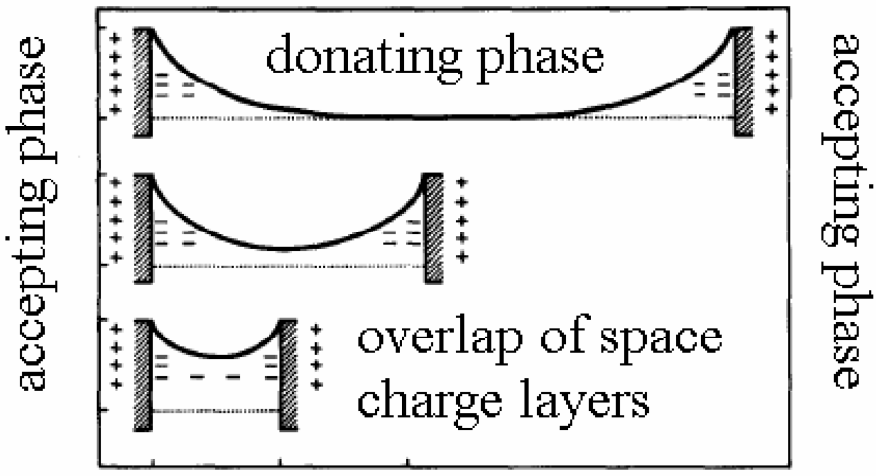

Figure 1.4. Overlapping space charge layers.
Source: [20]

1.5. Research questions and Outline of the Thesis

The concept of intermediate temperature fuel cells shows great promise for future application in transportation purposes. Nanostructuring of solid acids appears to result in materials with potential to be applied in these types of fuel cells from startup temperatures near ambient up to 250°C. The mechanism responsible for the enhanced conductivity is debated in literature, because no microscopic experiments and explanations have resolved their origin unambiguously yet. What exactly happens when nanostructuring these materials? What is the influence on the original conduction mechanism? What factors play a role in the nanostructuring? Can we influence the magnitude of the effects of nanostructuring?
The holy grail of the intermediate temperature electrolyte has not been found yet. Understanding the effects of nanostructuring will provide direction in the search of the holy grail: an ideal intermediate temperature fuel cell electrolyte.
In order to get more insight into this matter, a multi technique approach is applied, using various microscopic techniques. In order to get structural information, X-ray diffraction (XRD) and neutron diffraction (ND) were applied. For information on the dynamics, Quasi Elastic Neutron Diffraction (QENS) and Nuclear Magnetic Resonance (NMR) spectroscopy was used next to dielectric impedance spectroscopy. Ab-initio calculations using the VASP package were performed for insight on both structure and dynamics. These techniques were chosen for their

sensitivity and complementary nature as local probe to different length and time scales.
This thesis is build up of 6 chapters. Chapter 1 is this introductory chapter. Chapter 2 discusses the experimental techniques and methods used in the next 4 chapters. The foundation of this thesis is these following 4 chapters, as they consist of either published or submitted papers. Chapter 3 shows a model study in which, space charge induced $^{2}H^{+}$ densities in TiO_2 are observed directly using neutron diffraction on two different nanoscale particle sizes of anatase immersed in concentrated sulphuric acid. Chapter 4 uses Neutron diffraction on Deuterated nanocomposite solid acid samples with TiO_2. The presence of deuterium ions in the crystal lattice of the TiO_2 nanoparticles is observed, which can only be a result of space charge effects. The formation of an amorphous phase is observed and is believed to be a result from the loss of protons from the solid acid close to the TiO_2. The amorphous phase will also contribute to the high mobility of the hydrogen ions. The influence of the space charge on the crystalline phase is investigated, as this crystalline phase also shows increased proton mobility, which was observed with Quasi Elastic Neutron Scattering and Nuclear Magnetic Resonance spectroscopy. Large fractions of the hydrogen ions show orders of magnitude enhanced mobility in nanostructured composites of $CsHSO_4$ and TiO_2 or SiO_2. Chapter 5 addresses a mechanically stable solid acid electrolyte, as a composite electrolyte of solid acid impregnated Nafion is synthesized. This composite membrane exhibits high proton conductivity above 100 °C in its dry state, making this easy to synthesize electrolyte membrane suitable for intermediate temperature operations. Chapter 6 expands the knowledge gained from the previous chapters to a more general theory, as this research is extended to another solid acid, cesium dihydrogen phosphate CsH_2PO_4. Nanocomposites with different nanoparticles (TiO_2, SiO_2) in various sizes and different solid acids ($CsHSO_4$, CsH_2PO_4) are investigated using Quasi Elastic Neutron Scattering and Nuclear Magnetic Resonance spectroscopy. The large amount of mobile protons is the result of all the solid acid material in the composites being influenced by the nanostructuring. Acidity can be used as indication for the amount of space charge occurring. A summary forms the last part of this thesis.

1.6. Additional Information

Silicon Dioxide (silica) SiO_2
The first industrial uses of crystalline silica were in metallurgical and glass making activities in three to five thousand years BC. It has continued to support human progress, being a key material in industrial developments especially in the glass, foundry and ceramics industries. It is used in a broad range of applications ranging from additive in food to thin film wafers in microelectronics. Silicon is the second

most abundant element in the earth's crust and occurs in many forms including sand, quartz and flint and as silicates in rocks and clays. Silica is hard, chemically inert and has a high melting point, which is a result of the strong bonds between the atoms. It occurs in nine different crystalline forms or polymorphs with the three main forms being quartz, which is by far the most common, tridymite and cristobalite, as well as in amorphous form. It contains silicon atoms bonded tetrahedrally to four oxygen atoms by means of single Si-O bonds. These covalent bonds extend in three dimensions, resulting in gigantic molecules. The empirical formula corresponds to SiO_2 due to each silicon atom being shared equally by two oxygen atoms. Silica is manufactured in several forms including fused quartz, crystal, fumed silica (or pyrogenic silica, trademarked Aerosil), colloidal silica, silica gel and aerogel.

Titanium Dioxide TiO_2

Titanium dioxide was initially used as white pigment in paint. Nowadays it has a wide range of applications, varying from pigment in toothpaste to electron collector in solar cells. Titanium dioxide TiO_2 occurs naturally in three crystalline forms: rutile, anatase and brookite. Rutile is the most common form, but anatase is thermodynamically more stable. Anatase has a tetragonal structure with space group I41/amd and is known for its property to facilitate small ions within the crystal lattice. Anatase is known from lithium insertion in the nowadays very commonly used lithium ion batteries.

Nafion

Nafion is the commercial name for a polymer developed by Dr. Walther Grot at Du Pont in the late 1960's for application as the electrolyte. It is based on Teflon and was the first synthetic polymer developed with ionic properties called ionomers. Nafion combines the physical and chemical properties of Teflon, such as extreme chemical resistance and relative high working temperatures with ionic characteristics, such as high ionic conductivity, acidity and high permeability to water. It is applied in a large range of applications, varying from humidity control of gases for medical purposes to electrolyte membrane in fuel cells.

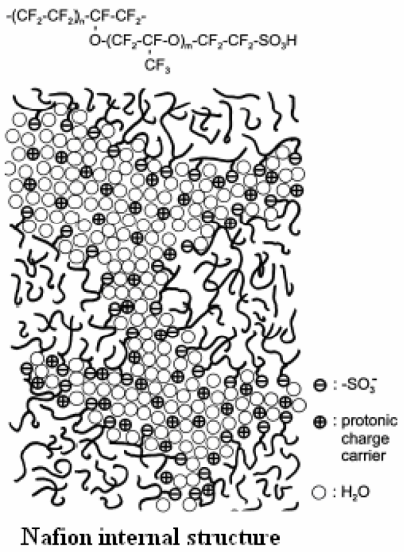

Figure 1.5. Internal structure and conduction mechanism of Nafion.

The proton conductivity mechanism of Nafion has been under discussion for a long time. Nafion conducts protons through water molecules through a vehicle mechanism. A model nowadays agreed upon is that Nafion consists of a Hydrophilic and Hydrophobic structure with an interconnecting network as shown in figure 1.5. In this network of hydrophilic channels the walls consist of sulfonic acid ended tails. The proton then is transported through water in these channels as Hydronium ions by exchange with SO_3H groups. Proton conduction in Nafion is based on the presence of water, and therefore comes with the limitations thereof.

Batteries versus hydrogen/fuel cells for transport applications

A big competitor for the fuel cell as power supply system in vehicles is the battery. Batteries have been getting lots of attention lately, due to recent technological breakthroughs and advances. They are currently considered the solution to power our future cars. Batteries are 3 times more efficient and produced electricity is stored directly and can be used immediately. When using hydrogen and fuel cells, the main problem for transport applications is its low overall efficiency, illustrated in figure 1.6. In the ideal and cleanest case the electricity needs to be generated twice, first for the process of water electrolysis and then again in the fuel cell to produce electricity and heat. On the other hand batteries however possess limited driving range, are slow to charge and require forward planning with recharging the batteries. Hydrogen is the most basic and abundant element in the universe. If made from renewable sources, the whole chain from source to the end consumer (fuel cell car) should not

contain any harmful emissions, with water and heat as the only exhaust products of the car. Fuel cell powered vehicles have long (potential) driving range, short refuel time, and require no changes in lifestyle compared to today's gasoline vehicles. As becomes clear from these arguments, both technologies have their pros and cons. The final solution will very likely be a combination of both, as can be seen from development of Fuel Cell Hybrid Vehicles FCHVs. Such vehicle would use batteries for short distances and high power demands and have a fuel cell as range extender.

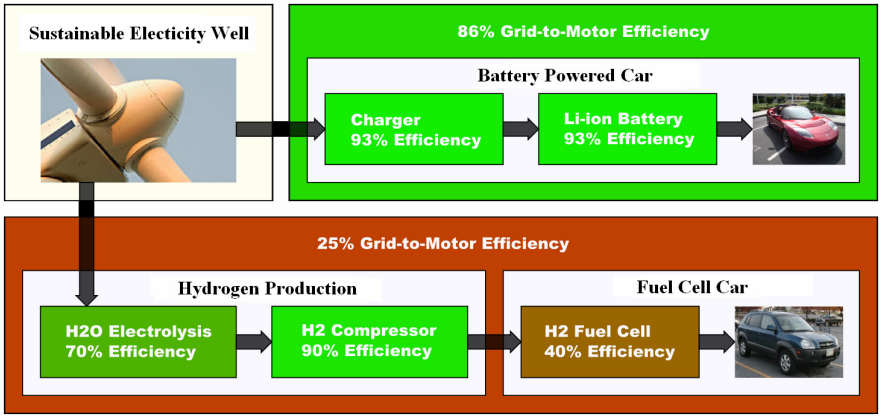

Figure 1.6. Well to wheel efficiency of sustainable electricity.
Source: [21]

Chapter 2.

Experimental, Methods and Theory

This chapter discusses more extensively the experimental details and theory. The experimental details include the preparation methods used in the synthesis of the samples and the type of samples prepared. The theory includes the principles of space charge and the theory behind the several measurement techniques used to investigate the samples. As the last 4 chapters in this thesis are built up of independent papers, the required theory is not always discussed there. This chapter aims to provide the necessary background information.

2.1. Synthesis

The big advantage of solid acids is the relative ease of synthesis. Synthesis generally occurs from aqueous solution, where the proper starting chemicals added in stoichimetric quantities chemically react. In the cases of $CsHSO_4$ and CsH_2PO_4:

Cs_2CO_3 (s) + $2H_2SO_4$ (s) → $2CsHSO_4$ (s) + CO_2 (g) + H_2O (l)
and
Cs_2CO_3 (s) + $2H_3PO_4$ (s) → $2CsH_2PO_4$ (s) + CO_2 (g) + H_2O (l)

Generally the $CsCO_3$ is dissolved in de-ionized water first and the acid is added slowly drop-wise. The solution is stirred for some time and the chemicals are allowed to react. There are various methods to precipitate the solid acid compounds from solution. The simplest cases, heating to evaporate excess water and solvent introduction to exceed the solubility limit of the solid acid are employed. Methanol

is introduced as secondary solvent at elevated temperatures. The solution is cooled in an ice bath afterwards and the crystals formed are separated by filtration.
For the deuterated samples, the same process was applied. However, since exchange of deuterium with protons from water in the air occurs, the synthesis was performed under a dry nitrogen environment. Recrystallization with methanol was not applied; instead the crystals were carefully filtered and dried.
The components for the nanocomposites consisted of the following:
Solid acids: Cesium Hydrogen Sulfate $CsHSO_4$ and Cesium dihydrogen Phosphate CsH_2PO_4; the chemicals for the synthesis of the solid acids, Cs2CO3, concentrated sulfuric acid (98%) and Phosphoric acid (85%) were bought from Sigma-Aldrich.
Nanoparticles: TiO_2 anatase with particle sizes: 7, 15, 24 and 40 nm. SiO_2 Aerosil with particles sizes: 7 and 40 nm. The particles were acquired from Evonik Industries (the 24 nm and 40 nm particles) and Nanoamor (the 7 nm and 15 nm particles).
Polymer matrix: Nafion 117 membrane. This polymer was bought from Du Pont.
Unless otherwise stated, the molar ratio between the solid acid and the nano particles was 1 mol solid acid versus 2 mol nano particles.

2.1.1. Dielectric Impedance Spectroscopy (IS)

The conductivity of the samples was measured by a.c. impedance spectroscopy using an Alpha high resolution dielectric analyzer. The samples were pressed into pellets and a gold layer was sputtered on both sides to improve contact with the electrodes. The frequency range was between 1 Hz and 3 MHz. The measurements were performed under a dry nitrogen atmosphere. After determining the resistivity from the Nyquist plots, the values were converted to geometry independent conductivities through:

$$\sigma = \frac{1}{\rho \frac{A}{L}} \qquad (2.1.1)$$

Where ρ is the resistivity, A is the Area and L is the thickness of the pellet.

Complex Impedance
The most common method used to analyze IS spectra is equivalent circuit modeling. Elements such as electrode double layer capacitances, solution resistances and diffusion layers can be simulated by using different configurations and combinations of electrical components, such as resistors, capacitors and inductors, accurately describing the behaviour of these elements. A simple model for an electrode-sample system is a capacitor and a resistor in parallel. Here the capacitor is

a result of the geometry and the resistor represents the resistivity of the sample. The response to an applied voltage in this circuit results in a current:

$$V(t) = V_0 e^{i\omega t} \tag{2.1.2}$$

$$I_{total} = I_R + I_C = \frac{V(t)}{R} + i\omega C\, V(t) \tag{2.1.3}$$

Here V_0 is the input voltage, ω the angular frequency, I_R the current in the resistor and I_C the current in the capacitor.
The complex impedance is defined as the ratio between the voltage and current:

$$Z = \frac{V(t)}{\frac{V(t)}{R} + i\omega C\, V(t)} = \frac{1}{\frac{1}{R} + i\omega C} \tag{2.1.4}$$

Which can be rewritten into a real part Z', and an imaginary part Z":

$$Z = \frac{\frac{1}{R}}{\left(\frac{1}{R}\right)^2 + (\omega C)^2} - i\,\frac{\omega C}{\left(\frac{1}{R}\right)^2 + (\omega C)^2} = Z' - i\,Z'' \tag{2.1.5}$$

Traditionally, complex impedance is plotted as Z' versus –Z", which is called a Nyquist plot. In this case the Nyquist plot results in a semicircle of radius R/2 in the first quadrant.

In the ideal case, one of strengths of complex impedance spectroscopy is its ability to resolve the electrode, bulk and grain boundary contributions to the resistance. In an ideal sample, this would be modeled as three semicircles. Proton conducting samples however, rarely show this behavior. Instead only two semicircles are present, representing the bulk and grain boundary contributions.
In practice, one semicircle and a nearly straight line was usually observed, shown in figure 2.1. This is caused by a variation of the effective resistance and capacitance of some elements in the circuit with frequency and is a result of the non ideality of the sample. For solid electrolytes, this situation typically refers to the mobile species diffusing through the electrodes. Such a process results in a straight line at 45 degrees to the x-axis and was initially reported by Warburg and described later by Macdonald [22].

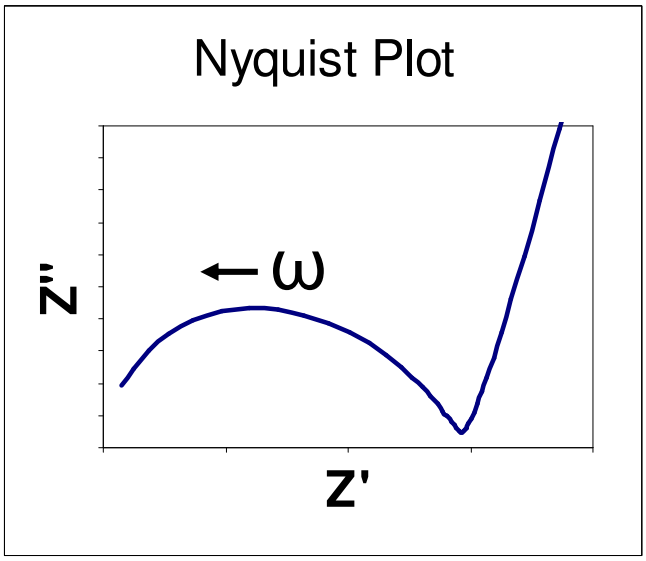

Figure 2.1. Realistic impedance plot showing a depressed semi-circle with center below the real axis and straight line at low frequencies; Both effects are due to the non ideal nature of the sample and can be modeled with inclusion of a constant phase element.

However, lines observed in this work usually deviated from 45 degrees and show depressed semicircles with centers below the x-axis. These deviations can be attributed to the non ideal nature of the samples, such as inhomogeneities in the samples and rough electrode / electrolyte surfaces.
Both these distributed effects can be modeled by introducing a constant phase element (CPE). The constant phase element is a circuit element that was invented while observing the response of real-world systems:

$$\frac{1}{Z_{CPE}} = A(i\omega)^n \qquad (2.1.6)$$

Here A has the numerical value of 1/Z at ω=1rad/s and n is a value between 0 and 1. Implementing the CPE results in an impedance represented by:

$$Z = \frac{V(t)}{\frac{V(t)}{R} + \frac{V(t)}{A(i\omega)^{-n}}} = \frac{1}{\frac{1}{R} + A(i\omega)^n} \qquad (2.1.7)$$

2.1.2. Differential Scanning Calorimetry (DSC)

The DSC measurements were performed on a Perkin Elmer DSC7 machine. Standard aluminium pans were used in a dry nitrogen environment. The heating rate was 10 degrees per minute. For the CsH_2PO_4 measurements, gold plated stainless steel high pressure capsules were used to ensure the containment of moisture. These capsules are able to withstand pressures up to 150 bars.
Differential scanning calorimetry DSC is a thermo analytical technique in which the difference in heat flow between the sample and a reference is measured as a function of temperature. The underlying principle of this technique is that when a sample undergoes a physical transformation, heat is required or released depending on whether the process is exothermic or endothermic. This difference in heat can be measured by a calorimeter, making this technique very suitable to detect phase transitions as the superprotonic phase transition or even more subtle phase changes such as glass transitions.

2.1.3. X-ray diffraction (XRD)

Powder X-ray diffraction measurements were performed on a Panalytical X'pert Pro diffractometer using Cu - Kα radiation and an Anton Paar TTK 450 low-temperature stage.
X-ray diffraction is a technique often used in condensed matter studies. It's very suitable to investigate the structure of samples as their wavelength is close to the length scales of the interplanar distances of crystals. X-rays scatter from the electrons in the sample, therefore the scattering scales with the size of the nucleus. A major advantage of the technique is its non-destructive nature as the radiation and interaction with the sample material is relatively low. Also, as opposed to some other microscopic techniques, the obtained signal represents an average over the whole sample. Furthermore, the penetrating nature of the x-rays allows for all sorts of special setups, enabling a large range of variations in temperature, pressure and other environments. X-rays are easy to produce and the instrumentation is relatively small.
The principle behind X-ray diffraction is based on Bragg's law (also see figure 2.2):

$$n\lambda = 2d \sin \theta \qquad (2.1.8)$$

Here n is an integer, λ the wavelength, d the interplanar spacing and θ the incident angle.
X-rays are scattered from a regular array of atoms in the crystalline material. When the path difference between the waves scattered from successive layers of atoms is a

multiple of the wavelength of the incident beam, constructive interference occurs. This gives rise to a scattering pattern characteristic of the crystal structure probed.

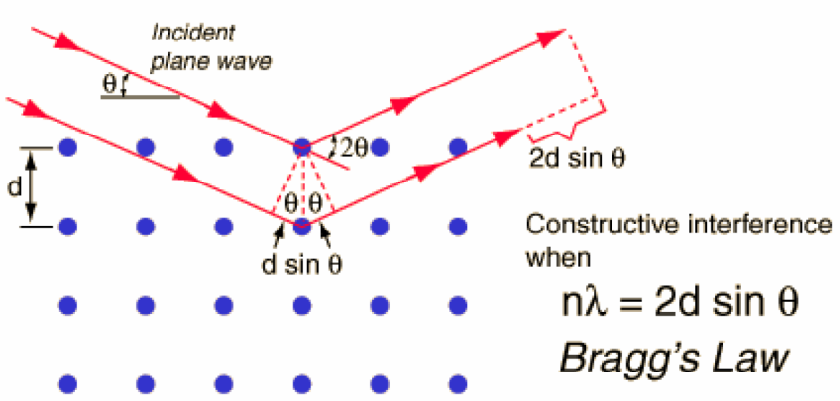

Figure 2.2. Bragg's Law

The obtained diffraction data were treated with Rietveld refinement using the software package GSAS. Information about grain sizes were obtained from peak broadening using the Scherrer Equation:

$$p = \frac{18000 K \lambda}{\pi X} \qquad (2.1.9)$$

Here p is the particle or grain size, K the Scherrer constant, λ the wavelength and X a parameter obtained from fitting the data.
X-ray diffraction has mainly been used to characterize the synthesized samples and to study the more basic parameters such as unit cell parameter and grain sizes. Notably, the presence of an amorphous solid acid phase could be quantified using XRD. This is quite unusual, as amorphous phases show no diffraction pattern. However, in the case of the nanocomposites with TiO_2, the phase fractions of the TiO_2 and the solid acid accurately represent the crystalline phases and the missing intensity of the solid acid represents the amorphous fraction of solid acid.

2.1.4. Inductively Coupled Plasma – Atomic Emission Spectroscopy (ICP-AES)

ICP has been a very small part of the study and has not been intensively used. However, it has played a very important role as it indirectly confirmed the presence of the amorphous phase in the nanocomposites.

Inductively coupled plasma - atomic emission spectroscopy ICP-AES, is a technique that is often used to detect trace metals. An inductively coupled plasma is used to produce excited atoms and ions, which emit radiation at characteristic wavelengths for particular elements. The intensity is a measure for the concentration of the element within the sample. A big advantage of ICP is its ability to accurately quantify low concentrations of a large range of elements, while only a small amount of sample (milligrams) is needed. More sample would increase the accuracy though.
In our case, the ratio between Titanium and Cesium was determined in the nanosamples and compared with the ratio found through diffraction analysis.

2.2. Space charge model for proton conducting composites

This paragraph gives a brief summary of a model describing the space charge theory and is extracted from the paper 'Large Space-Charge Effects in a Nanostructured Proton Conductor' by L.A. Haverkate. It is not the intention to fully describe the theory and its derivation. For a more extensive description of this theory one is referred to the paper [23]. The theory is especially developed based on composites of TiO_2 (or SiO_2) nanoparticles and solid (or liquid) acids [24]. This was necessary because the system differs from the usual Frenkel and Schottky systems as the defects are not present in the pure compounds and the defect density grows very large.
The system in question involves a hetero-junction, where mobile positively charged particles $P^{\bullet}$ diffuse from a site P_D in the donating phase (D) to the phase boundary and penetrate into an accepting phase (A). The charged particle fills an available site V_A in A and leaves an oppositely charged vacancy $V_D{}'$ in D. The equilibrium state at the interface can be described by:

$$(P_A^{\bullet} - V_A) + (V_D{}' - P_D) \rightleftharpoons 0 \qquad (2.2.1)$$

Two equilibrium conditions hold, firstly for the defect chemical equilibrium:

$$\tilde{\mu}_+^a(x^a) + \tilde{\mu}_-^d(x^d) = 0 \qquad (2.2.2)$$

Here $\tilde{\mu}_+^a$ and $\tilde{\mu}_-^d$ are the electrochemical potentials of a positively charged defect in the accepting phase and a negatively charged defect in the donating phase.
Secondly the transport equilibrium holds for mobile defects:

$$\frac{\partial}{\partial x}\ \tilde{\mu}_j(x) = 0 \qquad (2.2.3)$$

For the two defects $j = +\ /-$
The electrochemical potential is split into a chemical part μ and an electric potential φ:

$$\tilde{\mu}_j(x) = \mu_j(x) + z_j e\,\varphi(x) \qquad (2.2.4)$$

Here z_j is the charge number and e the elementary charge.

Typically a Boltzmann distribution would be used to approximate the chemical potential when assuming that the number of defects is much smaller than the number of available states and much larger than one. However, in our case the defect concentrations can become so large that the entropy term needs to be modified resulting in the following expression:

$$\mu_j(x) = \mu_j^0 + k_B T \ln \frac{c_j(x)}{c_j^0 - c_j(x)} \tag{2.2.5}$$

Here μ_j^0 is the free formation enthalpy of one vacancy in the bulk lattice, k_B the Boltzmann constant, $c_j(x)$ the position-dependent concentration of defects and c_j^0 the reference concentration.
Besides the equilibrium conditions (2) and (3), the charged defects are subject to the Poisson equation:

$$\frac{\partial^2}{\partial x^2}\ \varphi(x) = -\ \frac{z_j e\, c_j(x)}{\varepsilon\, \varepsilon_0} \tag{2.2.6}$$

Here $\varepsilon\varepsilon_0$ is the dielectric permittivity.
Furthermore, the following boundary conditions have to be defined:
1. The electric field must be zero in the center of the two phases
2. There is a constant dielectric displacement at the phase boundary
3. There is no free space in between the two phases; no potential drop at the interface

By combining equations (4) and (5) with (3) for the accepting phase and taking z_j = 1 results in:

$$k_B T\ \ln\left[\frac{c_+(x)}{c_{+m}}\ \frac{c_+^0 - c_{+m}}{c_+^0 - c_+(x)}\right] = e\Big(\varphi_m^a\ -\varphi\ (x)\Big) \tag{2.2.7}$$

Here $c_{+m} \equiv c_+(-x_m^a)$ is the centre concentration and $\varphi_m^a \equiv \varphi\ (-x_m^a)$ the electrical potential in the phase centre.
Introducing the terms for concentration enhancements $\zeta_+(x) \equiv c_+(x)\ /\ c_{+m}$ and $\zeta_+^0 \equiv c_+^0\ /\ c_{+m}$ results in:

$$\ln\left[\zeta_+(x)\ \frac{\zeta_+^0-1}{\zeta_+^0-\zeta_+(x)}\right]=\frac{e\left(\varphi_m^a\ -\varphi\ (x)\right)}{k_BT}\equiv Z_+(x) \tag{2.2.8}$$

$Z_+(x)$ is a measure for the potential difference between x and the phase centre, relative to the thermal energy. Isolating $\zeta_+(x)$ gives:

$$\zeta_+(x)=\frac{\zeta_+^0\ \exp\left[\,Z_+(x)\right]}{(\zeta_+^0\ -1)+\exp\left[\,Z_+(x)\right]} \tag{2.2.9}$$

By combining this equation with the Poisson equation a differential equation for the electric potential is derived:

$$\frac{\partial^2}{\partial x^2}\ Z_+(x)=\frac{1}{(\lambda_+)^2}\ \frac{1}{2}\ \frac{\exp\left[\,Z_+(x)\right]}{(\zeta_+^0\ -1)+\exp\left[\,Z_+(x)\right]} \tag{2.2.10}$$

With the Debye length defined as:

$$\lambda_+\ \equiv\sqrt{\frac{\varepsilon_a\,\varepsilon_0\ \ k_BT}{2\ \ e^2\,c_+^0}} \tag{2.2.11}$$

Working out the differential equation applying the boundary conditions and further combining with the equilibrium conditions and the equations (3), (5) and (8) for both the donating and accepting phase results in the following final expressions:

$$x+x_m^a=\lambda_+\int_0^{\frac{e\left(\varphi_a^m\ -\varphi\ (x)\right)}{k_bT}}dZ'\left(\ln\left[\frac{c_{+m}}{c_+^0}\ (e^{Z'}-1)+1\right]\right)^{-\frac{1}{2}} \tag{2.2.12}$$

This describes the potential drop as a function of the position and the concentration c_{+m} in the center of the accepting phase.

$$x-x_m^d=\lambda_-\int_0^{\frac{e\left(\varphi\ (x)\ -\varphi_m^d\right)}{k_BT}}dZ'\left(\ln\left[\frac{c_{-m}}{c_-^0}\ (e^{Z'}-1)+1\right]\right)^{-\frac{1}{2}} \tag{2.2.13}$$

This expression describes the potential drop in the donating phase. Here φ_m^d is the potential in the centre and c_{-m} the centre concentration of negatively charged defects in the donating phase.

$$\frac{\varepsilon_a}{\lambda_+}\sqrt{\ln\left[\frac{c_{+m}}{c_+^0}\left(\exp\left[\frac{e\varphi_m^a}{k_BT}\right]-1\right)+1\right]} = -\frac{\varepsilon_d}{\lambda_-}\sqrt{\ln\left[\frac{c_{-m}}{c_-^0}\left(\exp\left[-\frac{e\varphi_m^d}{k_BT}\right]-1\right)+1\right]} \tag{2.2.14}$$

This describes the potential at the interface.

$$\frac{e\left(\varphi_m^a - \varphi_m^d\right)}{k_BT} = -\frac{\Delta G_F}{k_BT} - \ln\left[\frac{c_{+m}}{c_+^0 - c_{+m}}\,\frac{c_{-m}}{c_-^0 - c_{-m}}\right] \tag{2.2.15}$$

This expression describes the two defect concentrations at the interface in terms of center concentrations.

2.3. Neutron Scattering

2.3.1. Introduction

The Neutron diffraction experiments were performed on deuterated liquid or solid acids mixed with TiO_2 nanoparticles and collected at room temperature on the high flux diffractometer Polaris at the pulsed spallation neutron source ISIS, Rutherford Appleton Laboratories, England.

The Quasi elastic neutron scattering experiments were performed on fully protonated samples on IN5 at the High flux reactor of the Institute Max von Laue-Paul Langevin (ILL). An incident wavelength of 11.5 Å and a resolution function with a full width at half maximum of ~ 6 μeV were used covering a Q range of 0.2 – 0.9 $Å^{-1}$. Air tight, flat, Aluminium sample containers were used.

Neutrons are a very suitable microscopic probe for condensed matter studies. The wavelength of thermal neutrons is of the order of the interatomic distances in condensed matter. While X-rays scatter from the electrons, neutrons interact with the nuclei. The strength of this interaction does not scale with the size of the nucleus, resulting in unexpectedly high sensitivity towards hydrogen. As with x-rays, neutron spectroscopy is a non destructive technique. The neutrality of the neutrons allows for great penetration depth, but also leads to complex instrumentation all around. They are also difficult to produce, resulting in large facilities and relatively low flux.

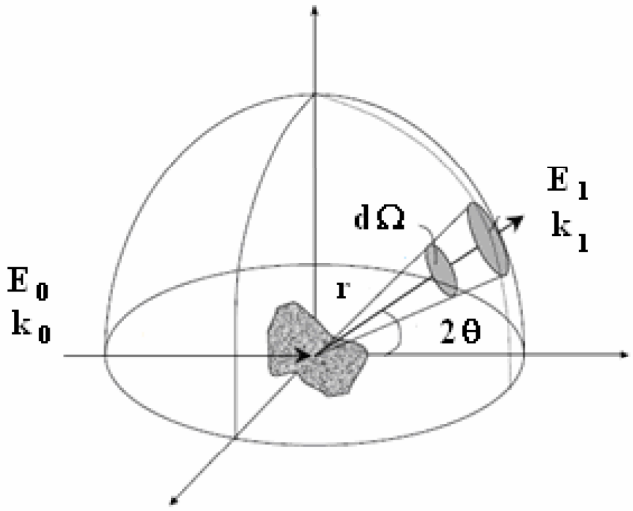

Figure 2.3. Schematic of neutron scattering geometry.

Consider an incident neutron beam with wave vector k_0 and energy E_0 scattering on a sample, resulting in k_1 and energy E_1. The momentum transfer is defined by:

$$\hbar Q = \hbar(k_1 - k_0) \tag{2.3.1}$$

And the energy transfer:

$$\hbar\omega = E_1 - E_0 = \frac{\hbar^2}{2m}\,(k_1^2 - k_0^2) \tag{2.3.2}$$

Here Q is the scattering vector, ħ the reduced Plank constant $\hbar = \frac{h}{2\pi}$ and m the mass of the neutron.
We define an element dΩ at a certain angle relative to the incident beam. The number of neutrons detected in this solid angle element having an energy between E_1 and E_1 + dE_1 and wave vector k_1 is defined as the double differential cross section:

$$\frac{d^2\sigma}{d\Omega dE} = \frac{I}{\Phi dE_1 d\Omega} \tag{2.3.3}$$

Here σ is the so called cross section, Φ the incoming neutron flux and I the number of neutrons per second detected.
Integrating this equation results in the differential cross section, which is an expression for the elastically scattered neutrons:

$$\frac{d\sigma}{d\Omega} = \int_0^\infty \left(\frac{d^2\sigma}{d\Omega dE_1}\right) dE_1 = \frac{I}{\Phi d\Omega} \tag{2.3.4}$$

And finally the total scattering is defined by:

$$\sigma = \int \left(\frac{d\sigma}{d\Omega}\right) d\Omega \tag{2.3.5}$$

2.3.2. Nuclear Scattering

During the scattering process the neutron experiences a potential V at a point r in the sample.

The probability for a transition of the neutron from the initial state Ψ_0 to a scattered state Ψ_1 and of the sample from state n_0 to n_1 can be described by Fermi's golden rule:

$$W_{0\to 1} = \frac{2\pi}{\hbar} \left| \left\langle \Psi_1 n_1 \left| V(r) \right| \Psi_0 n_0 \right\rangle \right|^2 \rho(k_1) \tag{2.3.6}$$

Here ρ(k1) is the density of final scattered states.
A good approximation for the interaction potential is the Fermi pseudo potential:

$$V(r) = \frac{2\pi\hbar^2}{m} \sum_i b_i \delta(r - R_i) \tag{2.3.7}$$

Here R_i is a set of positions for the nuclei and b_i the scattering length, which is a measure for the strength of the interactions between neutron and nucleus.
Combining these with equation (2.3.4) allows us to separate the differential cross section into a coherent and an incoherent term:

$$\frac{d\sigma}{d\Omega} = \left(\frac{d\sigma}{d\Omega} \right)_{coh} + \left(\frac{d\sigma}{d\Omega} \right)_{inc} \tag{2.3.8}$$

With the coherent term being:

$$\left(\frac{d\sigma}{d\Omega} \right)_{coh} = \left| \sum_i < b_i > e^{iQ \cdot R_i} \right|^2 \tag{2.3.9}$$

And the incoherent term:

$$\left(\frac{d\sigma}{d\Omega} \right)_{inc} = \sum_i \left[< \left| b_i \right|^2 > - \left| < b_i > \right|^2 \right] \tag{2.3.10}$$

2.3.3. Coherent scattering

A unit cell can be defined by the set of vectors a_1, a_2 and a_3, with the position of the origin of a certain unit cell defined by three integers:

$$L = l_1 a_1 + l_2 a_2 + l_3 a_3 \tag{2.3.11}$$

The position of an atom i can then be expressed as follows:

$$R_i = r_j + L \tag{2.3.12}$$

Here r_j is the vector from the unit cell origin pointing to the atom i.
After we define the reciprocal lattice vectors b:

$$a_v \cdot b_\mu = 2\pi\delta_{v\mu} \tag{2.3.13}$$

Here v = 1,2,3 and μ = 1,2,3.
A reciprocal lattice vector can be formulated:

$$G_{hkl} = hb_1 + kb_2 + lb_3 \tag{2.3.14}$$

Here h, k and l are integers.
Combining these equations with equation (2.3.9) and the nuclear structure factor:

$$F(Q) = \sum_j < b_j > e^{iQ \cdot r_j} \tag{2.3.15}$$

Results in the following expression:

$$(\frac{d\sigma}{d\Omega})_{coh} = N \ \frac{(2\pi)^3}{v_a} \ \big| F(Q) \big|^2 \ \sum_{G_{hlk}} \delta(Q - G_{hkl}) \tag{2.3.16}$$

Here N is the number of unit cells and v_a is the unit cell volume. Reflections are only found in the directions given by the condition Q = G_{hkl}. The intensities of these reflections are determined by the structure factor, which is dependent on the content of the unit cell.
However, the equations we give here are valid for perfect single crystals. In real life experiments often a powder is measured, where the orientation of the crystals are randomly distributed. This results in Debye-Scherrer cones for the scattered neutrons and actually facilitates the powder diffraction experiment as only one angle suffices to detect many reciprocal lattice vectors. This angle is defined as 2θ.

Thermal motions
Thermal motions also play a role in the scattering experiment. The position of an atom is now given as follows:

$$R_j = r_j + L + u_i \tag{2.3.17}$$

Here u_i is the isotropic displacement of the atom. The Debye-Waller factor can now be incorporated in the structure factor:

$$T_j(Q) = \left\langle e^{iQ\cdot u_j} \right\rangle = e^{-\frac{1}{6}Q^2\left\langle u_j^2\right\rangle} \tag{2.3.18}$$

$$F(Q) = \sum_{j=1} \left\langle b_j \right\rangle e^{-\frac{1}{6}Q^2\left\langle u_j^2\right\rangle} e^{iQ\cdot r_j} \tag{2.3.19}$$

Fourier maps
Combining with knowledge about the space group of the crystal, the measured structure factors F can be used as Fourier coefficients to calculate so called Fourier Maps as follows:

$$\rho(r) = \frac{1}{v_a} \sum_{h,k,l} F(G_{hkl}) e^{iG_{hkl}\cdot r_j} = \frac{1}{v_a} \sum_{h,k,l} F(G_{hkl}) e^{2\pi i(hx_j+ky_j+lz_j)} \tag{2.3.20}$$

This method is a powerful way to determine the real space scattering length density in the unit cell. It is especially useful in the analysis of the diffraction data as it allows for visualization of the atoms in the structure.

2.3.4. Quasi Elastic Neutron Scattering

During an inelastic scattering event momentum and energy transfer occur. This means that the potential V is not only position dependent, but also time dependent $V = V(r,\ t)$.

Again applying Fermi's golden rule and writing the energy law as δ function leads to the following expressions for the double differential cross section.
The coherent differential cross section:

$$\left(\frac{d^2\sigma}{d\Omega dE_1}\right)_{coh} = \frac{k_1}{k_0}\frac{\sigma_{coh}N}{8\pi^2} \int G(r,\ t) e^{i(Q\cdot r-\omega t)} drdt \tag{2.3.21}$$

Here N is the number of particles and G(r,t) the pair-correlation function. It represents the probability of finding any atom at the position r at time t, given there was an atom at the origin at t=0.

And the incoherent double differential cross section:

$$\left(\frac{d^2\sigma}{d\Omega dE_1} \right)_{inc} = \frac{k_1}{k_0} \frac{\sigma_{inc} N}{8\pi^2} \int G_s(r,\ t) e^{i(Q\cdot r - \omega t)} dr dt \qquad (2.3.22)$$

Here $G_s(r,t)$ is the self-correlation function and represents the probability of finding an atom at the position r at time t if it was at the origin at time t=0.
Finally we introduce the expressions for long range diffusion:

$$S_{inc}(Q,\ \omega) = \frac{1}{\pi} \frac{DQ^2}{(DQ^2)^2 + \omega^2} \qquad (2.3.23)$$

Here S_{inc} represents the scattering function and D is the diffusion constant. It can be observed that the spectrum of the scattered neutrons exhibit the shape of a Lorentzian function, with a full width at half maximum (FWHM) that increases with the momentum transfer according to $2DQ^2$. This allows for a rather simple and direct determination of the diffusion coefficient. Care however has to be taken as this method is restricted to small Q values and energy transfers.
Analogous to the Elastic Incoherent Structure Factor EISF, the fraction of diffusion species can be experimentally approximated by the simple relationship:

$$f = \frac{I_{qe}}{I_e + I_{qe}} \qquad (2.3.24)$$

Here I_{qe} is the quasi elastic intentisy and I_e the elastic intensity.

2.4. Nuclear Magnetic Resonance NMR

2.4.1. Introduction

NMR measurements on nanocomposite solid acid samples were performed at the solid-state NMR facility for advanced materials science, which is part of the Radboud University in Nijmegen. A 400 MHz spectrometer was used with a static magnetic field strength of 9.4 T. The ^{1}H and ^{2}H Larmor frequencies were 399.95 and 61.39 MHz respectively. A 3.2mm airtight zirconia rotor was used to measure the Magic Angle Spinning (MAS) ^{1}H or ^{2}H 1D spectra and spin-lattice relaxation times. The spinning frequencies were between 14 and 17 kHz.

Nuclear Magnetic Resonance (NMR) is an excellent technique to study both crystalline and amorphous materials. It offers a way to study the electronic and magnetic environment as well as the local atomic configuration of a large range of nuclei and the influence of its surroundings on them. Furthermore, dynamic processes that influence the relaxation of the nuclear spins can also be studied. All nuclei with spin number $I \neq 0$ are suitable to be detected in this technique. This includes nuclei with an odd atomic mass and nuclei with an even atomic mass and an odd mass number. The former possesses a half integer spin and the latter a whole integer spin.

When an external magnetic field is applied to a nucleus, the nuclear magnetic moment interacts with this field (Zeeman effect) and Quantum mechanics dictates that for a nucleus with spin number I, the nuclear spin energy level will split in 2I + 1 possible energy levels. The initial populations of these energy levels are determined by thermodynamics and follow a Boltzmann distribution. This means that the lower energy level is slightly more populated than the higher level, resulting in a net magnetization, which is parallel or anti parallel to the external magnetic field depending on the sign of the gyromagnetic ratio. In NMR spectroscopy these nuclei are excited from the lower energy level into the higher energy level with r.f. radiation. The frequency of this radiation is determined by the difference in energy between the levels and can be calculated by:

$$\Delta E = \gamma \hbar B \qquad (2.4.1)$$

Here γ is the gyromagnetic ratio, a fundamental constant dependent on the nature of the nuclei, $\hbar$ the reduced Planck constant and B the external static field. It can be seen that the difference in energy between the levels is dependent on the strength of the external field and also that a larger gyromagnetic ratio results in a larger difference in energy.

Usually, an r.f. pulse is applied, such that the net magnetization rotates towards the plane perpendicular to the external magnetic field. This is called a $\pi/2$ pulse. The net magnetization starts precessing in the perpendicular plane with a typical frequency for the nucleus called the Larmor frequency. A coil placed in the precession plane picks up an induced current, which shows as a damped oscillating signal as a function of time, called the free induction decay (FID). Fourier transform of this signal results in the actual frequency dependent spectrum.

2.4.2. Nuclear spin interactions

Many (anisotropic) interactions with the environment modify the nuclear spin energy levels and thus the precession frequencies. As result of these interactions the nuclear magnetic resonance lines are influenced. The following nuclear spin interactions in the solid phase are commonly occurring:

Chemical shielding
Under influence of the external magnetic field currents of the electrons in the molecular orbitals are induced. These induced currents create local magnetic fields around the nuclei shielding it (slightly) from the external field. The strength of these fields scales with the external field and depend on the local chemical environment the nucleus is in, and varies across the entire molecular framework. Variation in Larmor frequency, due to variations in the local electron distribution, are called chemical shifts. The chemical shift is expressed relative to a reference frequency or reference molecule. Generally the chemical shielding can be anisotropic, leading to a different chemical shift when rotating the crystal in the applied field. This is called chemical shift anisotropy. In magic angle spinning of powder samples this leads to spinning sidebands.

Dipolar interaction
Nuclear spins exhibit a dipole moment. The main interaction between the dipole moments of two nuclei is called dipolar coupling. The magnitude of the interaction depends on the nucleus, the internuclear distance and the orientations of the spins with respect to each other and the external magnetic field. The dipolar coupling can be described as follows:

$$d = \frac{\hbar \mu_0 \gamma_1 \gamma_2}{4\pi r^3} \qquad (2.4.2)$$

Here d is the dipolar coupling constant, r the distance between the nuclei, and γ_1 and γ_2 are the gyromagnetic ratios of the nuclei involved. The angular dependence of the dipolar coupling with respect to the external field is given by:

$$D \propto 3\ \cos^2\ \theta - 1 \qquad (2.4.3)$$

Here D is the dipolar coupling and θ is determined by the position of the nuclei with respect to the appied magnetic field.

Quadrupolar interaction
Nuclei with a spin I ≥ 1 have a quadrupole moment as result of non spherical charge distribution of the nucleus. In a crystal with less than cubic symmetry this non sperical charge distribution will interact with an electric field gradient caused by this non-symmetric environment. This results in changes in the energy levels on top of the Zeeman effect. Quadrupolar interactions can be large in size such that they can become comparable to the Zeeman interactions. The first order interaction has a similar angular dependency as the dipolar interaction. The second order interaction however has a more complicated dependency.

Magic Angle Spinning
In solid state NMR the technique called Magic Angle Spinning is frequently applied to reduce the large line widths caused by these (anisotropic) interactions. Three important interactions, chemical shift anisotropy, dipolar interaction and quadrupolar interaction, contain $3\cos^2\theta(t)$ - 1 terms. While in liquid state NMR rapid random tumbling averages these interactions, here an artificial motion is introduced. By rapidly spinning the sample at an angle of $\theta_{rotation}$= 54.74° with respect to the external magnetic field, the time averaged term $<3\cos^2\theta(t) - 1>$ becomes 0. The rotation frequency needs to be at least of the order of the line broadening interaction expressed in Hz. As a result the dipolar interaction and the first order quadrupolar interaction are averaged, ultimately reducing to zero. Spinning side bands become visible if the spinning rate is lower than the magnitude of the (anisotropic) interactions. The intervals between the side bands have the value of the spinning rate. Figure 2.4 illustrates the importance of Magic Angle Spinning.

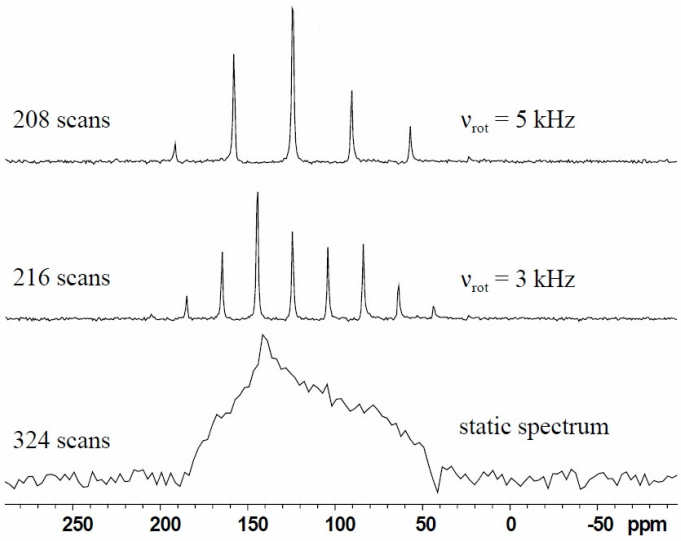

Figure 2.4. Importance of Magic Angle Spinning for the ^{13}C NMR spectrum of a ^{13}C containing solid.

Although the spinning rate here is lower than the magnitude of the anisotropic interaction, the intensity of the signal is localized under the spinning side bands, significantly improving the resolution and the signal to noise ratio of the NMR spectrum.

2.4.3. Relaxation processes

Spin-lattice relaxation

Nuclei in the lattice are subject to vibrational and rotational motions, creating varying interactions. This can cause so called spin-lattice or longitudinal relaxation. The characteristic relaxation time is called the T_1 relaxation time. As the mobility varies, the T_1 relaxation time reaches a minimum when the mobility timescales are approximating the larmor frequency. The dependence of the net magnetization in a saturation recovery experiment on the T_1 relaxation time can be described by the following equation:

$$M(t) = M_0(1-\exp(\frac{-t}{T_1})) \qquad (2.4.4)$$

Here M(t) is the magnetization at time t and M_0 the net magnetization in the equilibrium state. This exponential is illustrated in figure 2.5.

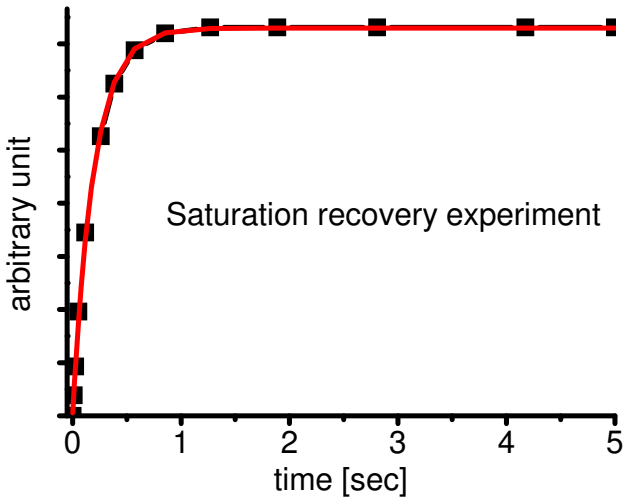

Figure 2.5. T_1 relaxation time in saturation recovery experiment.

Chapter 3.

Model study on hydrogen in TiO_2 anatase nanoparticles

This chapter is based on the published paper:
Direct observation of space charge induced hydrogen ion insertion in nanoscale anatase TiO_2

Wing K. Chan, W.J.H. Borghols, and F.M. Mulder

Abstract

Space charge induced $^2H^+$ densities up to $^2H^+_{0.09}TiO_2$ are observed directly using neutron diffraction on two different nanoscale particle sizes of anatase TiO_2 immersed in sulphuric acid, and consistent with experimental evidence, modelling shows that these ions show rapid self diffusion.

3.1. Introduction

Recently it has been shown that solid acid super protonic conductors that can be applied as fuel cell electrolyte [7] can show enhanced conductivities by blending with nanoparticulates like TiO_2 and SiO_2 [25-30]. Fuel cell membranes made of hybrid organic-inorganic nanocomposites consisting of Nafion and anatase TiO_2 were recently reported [31] and exhibit good proton conductivities and extended

operation temperatures. Not much is known about the charge transport and ionic densities that are present in the nanofilled materials like TiO_2, although there are indications that such material can play a role in the ion transport itself. For instance it was also shown recently that 18 nm thick TiO_2 layers can transport protons [32] at temperatures as low as 80^{o}C in a fuel cell configuration. In order to investigate the hydrogen density and transport inside such nano filler we present here a study on the hydrogen density and mobility inside TiO_2 nanoparticles immersed in sulfuric acid.
An important factor influencing the ionic densities and conductivity of nanostructured ionic conductors in general is the presence of so called space charge effects [19, 33]. The basic mechanism responsible for the creation of space charges is the difference in chemical potential that charged ions have in the different ionic compounds that are in close contact in e.g. a nanocomposite. This difference drives charged ions from one phase to the other, breaking charge neutrality at the interface. The ion flow stops as soon as the electric field that builds up counterbalances the difference in chemical potential. The length scale involved in these interface effects is typically of the order of few tens of nm (Debije length). When the crystallite sizes of the different ionic phases becomes of the order of this space charge layer thickness, the entire particle becomes influenced by the space charge induced ionic density changes and one can then speak of true nanoscale size effects [19]. The effect of the space charges on the ionic conductivity is mainly due to the abundant vacancies and the introduction of mobile ions in the space charge regions of the material. For this reason we investigate here by a direct probe, neutron diffraction, the density of hydrogen inserted in nanoscale TiO_2 crystallites when immersed in concentrated sulfuric acid. Sulfuric acid is used because in sulfonated polymer membranes H_2SO_4 is used to activate the proton conductivity [34]. Because of its acidic nature the proton has a high chemical potential in the acid and space charges can be expected to build up. The result for the location of the inserted ions is compared to ab initio calculations , and in addition less computationally costly force field molecular dynamics symulations are used to estimate the mobility of the ions. To the best of our knowledge this is the first time that the induced ionic density is observed directly.

3.2. Experimental section

For the experiments TiO_2 nanopowders with average size of 7 nm (obtained from NanoAmor) and 24 nm (Nanoaltair) were dried in a vacuum oven and subsequently immersed in liquid D_2SO_4 (98 wt% solution in D_2O, 99.5+ atom % D). Deuterium is used because proton containing samples have an unwanted high background in neutron diffraction due to the large incoherent cross section of ^1H. Neutron diffraction was performed using GEM, a high performance diffractometer at ISIS,

Rutherford Appleton Laboratories (Uxfordshire, UK). The particle sizes were taken from the neutron diffraction linebroadening and were consitent with electron microscopy. Liquid D_2SO_4 was used in order to prevent overlapping spectra of another crystalline phase in this first study that will be used as a benchmark for other studies. Although D_2SO_4 is a liquid, the same arguments about the chemical potential difference hold. The samples were measured at room temperature and the tubes were sealed airtight to prevent exchange of deuterium with protons in humid air. The diffraction data were analyzed with the Rietveld method using the software GSAS [35]. Three dimensional (difference) Fourier maps were generated using the program Fox [36] in order to ellucidate the position of inserted density of deuterons within the structure.

3.3. Results and Discussion

Figure 3.1 shows the diffraction spectra of the 24 nm TiO_2 samples, with and without D_2SO_4. The differences between the spectra are small, but with the high statistics clearly detectable. In the inset a part of the spectra is enlarged to illustrate the subtle differences.

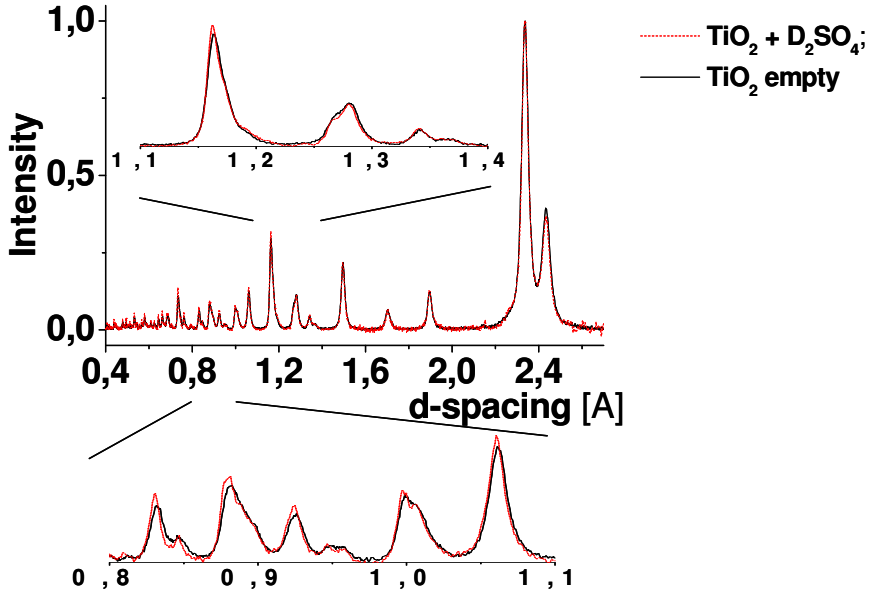

Figure 3.1. Diffraction spectra of 24 nm TiO_2 before and after immersion in D_2SO_4, normalised at the largest peak intensity. Subtle changes in peak intensities occur that

give direct information on the location and density of deuterium nuclei in the TiO_2 lattice.

In figure 3.2 the resulting Fourier map of the 24 nm sample in D_2SO_4 is shown. Appart from the Ti and O atoms from TiO_2 there are clear high density spots visible due to the presence of inserted D ions. This density is located at [0.00, 0.75, 0.43] (fractional coordinates). The distance between the deuteron and the nearest oxygen atom is 0.92 Å. Such distance is comparable to the distance of 0.95 Å between O and H in an OH^- group. The position as well as the occupancy and temperature factor of this deuteron density was refined. The result was a clearly better agreement between the data and the fitted spectrum (5% lower R factor vs. fit without D, wRp: 0.0044, 24 nm sample). Both TiO_2 particle sizes, 24nm and 7nm, were analyzed in this way resulting in occupancies of 0.045 for the former and 0.085 for the latter. This translates in deuteron intercalation of respectively 0.09 and 0.17 per TiO_2.

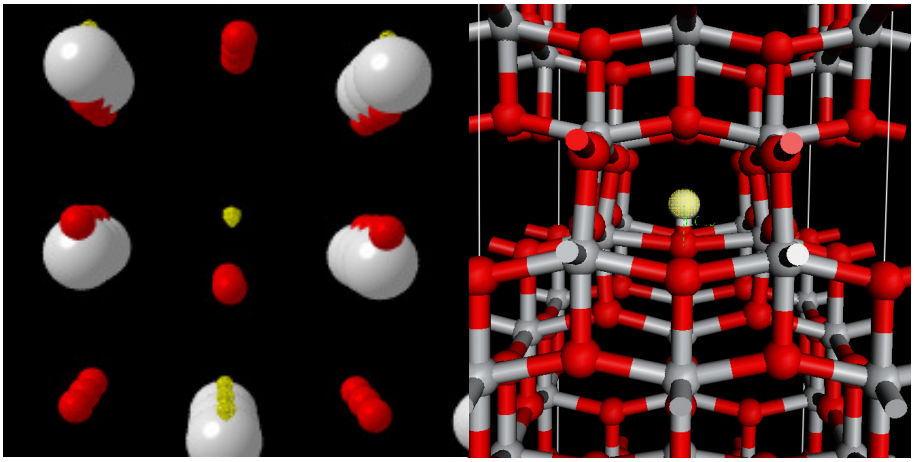

Figure 3.2. ***(Left)*** Fourier difference map showing the deuteron position (yellow shape) from the diffraction experiments (Ti: gray, oxygen: red). ***(Right)*** Calculated H position using VASP. It can be seen that the position resulting from the calculations is the same as the one from the diffraction experiments.

Atom	X	Y	Z	Uiso [Å^2]	occupancy
Ti	0	¾	1/8	0.005±0.005	1
O	0	¾	0.3301	0.007±0.005	1
D	0	¾	0.43	0.06±0.01	0.045±0.005

Table 1. Refined structure of 24 nm anatase D^+ inserted TiO_2 in D_2SO_4 at 293K. The space group is I41/amd (space group no. 141) with a= 3.785 Å and c= 9.508 Å.

The experimental results for the D position are compared to first principles calculations. We calculated the position of protons in TiO_2 using the density functional approach as implemented in the ab-initio package VASP [37-39]. The standard pseudopotentials for Ti, O, and H were used as described in the Generalised Gradient Approximation (GGA). The structure of a 2x2x2 TiO_2 supercell including one proton was minimised in order to determine the minimum energy position of the H. The calculations show a position as in Figure 3.2, with a distance of the proton to the oxygen of 0.99Å. This position is in very good agreement with the results from the diffraction experiments. There are two equivalent sites in the oxygen octahedron with a splitting of 3.95 Å between them. It is essential to use a model in which the H density is not higher than experimentally observed because for high H densities the H atoms will start interacting, which will influence the structure. It is interesting to note that such split position of the H is similar to that of intercalated Li in $Li_{0.02}TiO_2$ anatase [40]: there too Li chooses one of two positions well above and below the centre of the oxygen octahedron. This split position of the Li ion inside the oxygen octahedron can also be reproduced by VASP in the same 2x2x2 model with a Li position of (0, 0.75, 0.520) (this result was not yet reported in [40] but it compares well with the experimental Li position of (0, 0.75, 0.5401)). The distance between the Li and its oxygen neighbour is 1.80 Å, i.e. much larger than the D-O distance, while the splitting between the two Li positions is reduced to 1.92 Å compared to the D-D splitting of 3.95 Å.
The experimentally observed D position agrees with the theoretically predicted one. This indicates that such modelling can reproduce the relevant factors in the structure. In order to model the diffusion of H through the structure using molecular dynamics simulations the ab initio method is too calculational intensive for reaching long simulation times. For this reason we used the ab initio based parametrised force field method COMPASS [41] as implemented in Materials Studio [42]. COMPASS reproduces the minimal energy position of the H atom from the experiment and from VASP. With a time step op 1 fs simulations of the same model were made as above for durations of up to 1200 ps at various temperatures. In figure 3.3 an Arrhenius plot is given of the observed hopping rates in the modeling. The error bars in the graph are calculated as the square root of the observed discrete number of hops. Two types of hops of the H atoms are observed: a small hop inside the same octaeder along the c-axis and a long hop from (the bottom position in) one octaeder to (the top in) a nearest neighbour one. The activation energies resulting from the linear fits

are $1.7x10^3$ K and $2.4x10^3$ K for the intra and inter hopping rates respectively. The temperature dependences of the simulated hopping rates ($1/\tau_{intra}$, $1/\tau_{inter}$) equal respectively $1.50 \cdot \exp[-1.7x10^3/T]$ and $1.37 \cdot \exp[-2.4x10^3/T]$ ps^{-1} for the intra- and inter- octahedron hops. Clearly the hoppingrate from octahedron to octahedron is slower than the intra octahedron one. The long range H diffusion may be viewed as a two step process of relatively fast intra octahedron hops and approximately an order of magnitude slower nearest neighbour octahedron hops. The diffusion coefficient D can be estimated from the inter octahedron hopping time τ and the average distance *l* between two sites in nearest neighbor octahedrons as follows: $D = l^2/4\tau_{inter}$, which equals $0.91x10^{-7}$ cm^2s^{-1} at 300K. Such value is only a factor three smaller than Nafion at 300K as reported in e.g. [43, 44] at 20% relative humidity [45], which may indicate that the diffusion of these protons in anatase nanoparticles is in itself high enough for fuelcell applications at 300K. At increasing temperatures this only improves.

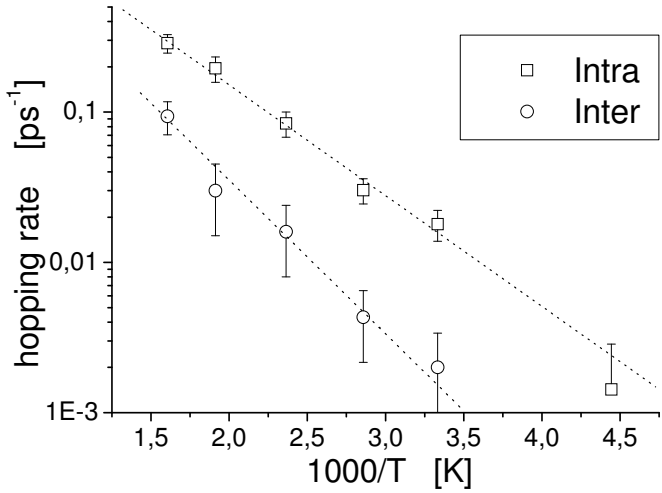

Figure 3.3. Arrhenius plot of the predicted hopping rate of a proton in TiO_2 as a function of temperature. The inter-octahedron hopping rate determines the long range diffusive motion since the intra octahedron hopping model is relatively fast.

It is interesting to note that in the previous study on Li insertion in anatase TiO_2 mentioned above [40] it was also found both experimentally and by using the force field modelling based on COMPASS that the Li position inside the oxygen octaheron was split in two positions. In that study the hopping of the Li ion between these two intra octahedron positions predicted by COMPASS was also observed directly using quasielastic neutron scattering. Such independent methods to measure the proton diffusion in nanoscale TiO_2 is currently developped; however an intrinsic

difficulty is to unravel the signal from the H inside TiO_2 from that in the acid that has to surround the nano particles.
An important observation that indicates that the TiO_2 has taken up positively charged deuterium ions and not the neutral atoms is that the material has not changed color. Upon neutral H and Li insertion in TiO_2 the electric and optical properties change significantly [46-48]. Upon neutral H insertion it appears that a deep electronic energy level is created at 0.52 eV inside the bandgap of 3.75 eV. This leads to the occurrence of strong absorption in the visible light and a blue colloration of the material. With Li insertion this can directly be observed as the original white powder turns blue. In contrast these nano-particle powders keep their white refracting appearance indicating that the deep levels at 0.52 eV are still unoccupied, i.e. the electrons accompanying the deuterium nucleus are missing. Therefore the observed deuterium ion insertion leads to the buildup of a space charge.
In principle such space charge layer extends only a finite length into the TiO_2. The Rietveld refienement assumes a constant average D density, and from the two particle sizes measured and the observed average D insertion density a rough estimate can be made of the typical lengthscale of the D insertion: a 24/7 times larger particle has on average 0.17/0.09 times less D inserted. Using an exponential decay from the surface these numbers are consistent with a typical length scale for insertion of ~ 11 nm with a typical maximum D insertion amplitude of ~0.25 at the surface.
Enhancing ionic conduction due to space charge effects can be benificient for e.g. proton conductors in fuel cell applications. Especially the application as electrolyte membrane in fuel cells operating at intermediate temperatures (120-250ºC), where conventional membranes based on humidified hydrophylic polymers are unable to operate [49] can be considered very promising [19]. Intermediate temperatures are favourable for three reasons. First the higher temperatures facilitate the utilisation of the waste heat, enhancing the overall energy efficiency. Second, the higher temperatures reduce the sensitivity to CO poisoning of the catalysts used. Third, the higher temperature makes cooling against the ambient environment less technologically demanding.

3.4. Conclusion

In conclusion, the presence of deuteron insertion in TiO_2 has been observed directly using neutron diffraction consistent with ab-initio modelling (VASP). A specific position, namely [0.00, 0.75, 0.43] has been found, corresponding with a split position of the deuterons inside the oxygen octahedron. Rietveld refinement shows occupancies at this position of 0.045 and 0.085 for TiO_2 particle sizes of 24nm and

7nm respectively, which translates in deuteron intercalation of 9% and 17%. No color change was observed, indicating that there are no electrons accompanying the deuteron intercalation. The larger occupancy that is observed for the 7nm particle size indicates the finite space charge layer thickness of the order of the particle sizes. Self diffusion as simulated using the force field COMPASS indicates high diffusion rates, comparable to those used in fuel cell electrolytes. Ion intercalation in nanocomposites of TiO_2 and an acidic proton conductor is very likely to occur more generally.

Chapter 4.

Structure and dynamics of hydrogen in nanocomposite solid acids for fuel cell applications

This chapter is based on the published paper:
Direct view on nanoionic proton mobility

Wing K. Chan, Lucas A. Haverkate, Dr. Wouter J. H. Borghols, Dr. Marnix Wagemaker, Prof. Stephen J. Picken, Dr. Ernst R. H. van Eck, Prof. Arno P. M. Kentgens, Prof. Mark R. Johnson, Prof. Gordon J. Kearley, and Prof. Fokko M. Mulder

Abstract

The field of nanoionics is of great importance for the development of superior materials for devices that rely on the transport of charged ions like fuel cells, batteries, and sensors. Nanostructuring often has significant impact on the ionic mobility due to the induced space charge effects. Here the surprisingly large space charge effects in the composites of the proton donating solid acid $CsHSO_4$ and the proton accepting TiO_2 or SiO_2 are studied; these composites have a negative enthalpy of formation for defects involving the transfer of protons from the acid to the acceptor. Very high defect densities up to 10% of the available sites are observed by neutron diffraction. The effect on the mobility of the protons is observed directly using quasi elastic neutron scattering (QENS) and nuclear magnetic resonance (NMR). Surprisingly large fractions of up to 25% of the hydrogen ions show orders

of magnitude enhanced mobility in the nanostructured composites of TiO_2 or SiO_2, both in crystalline $CsHSO_4$ and an amorphous fraction. The presence of deuterium ions in the crystal lattice of the TiO_2 nanoparticles has been observed, directly illustrating these ion transfers in space charge effects. The solid acid $CsHSO_4$ is also chosen for this study because it can operate effectively as fuel cell electrolyte at elevated temperature while the low temperature conductivity is increased upon nanostructuring.

4.1. Introduction

For the transformation of chemical to electrical energy in fuel cells, the chemical storage of electrical energy in batteries, or the transformation of chemical to electrical information (chemical sensors), the field of nanoionics plays an increasingly important role [19, 50-52]. The prospects of future alternative energy sources and the need for environmental protection multiply the need of energy storage and conversion devices in which nanoionic materials can play an important role. In a sense nanoionics is a complementary field to nanoelectronics which has become an indispensable technology for our society, with major applications in computers, (future) solar cells and medical diagnosis [53]. Nanoionics concerns the study and application of properties, phenomena, and mechanisms related with ion transport and storage in (solid state) nanoscale systems. Within this field are systems based on solids with relatively low ionic conductivity, where the implementation of interfaces induce significant concentrations of charged defects, which in turn can have significant effect on the ionic conductivity [54, 55]. Methods to induce such nanoionic phenomena include the blending of ionic conductors with nanoparticles [13, 30], or the deposition of thin layers of different ionic conductors [33].
In order to make a sustainable hydrogen economy feasible the chain that includes hydrogen production, storage and back-conversion using fuel cells [56, 57], requires significant advances on all fronts. Certain types of nanoionic materials have the potential to serve as 'intermediate temperature' fuel cell electrolyte membranes. Most commercially available fuel cells operate using a polymer electrolyte (PEMFC), and operate well below 100^{o}C in order to maintain the humidity of the electrolyte. Fuel cells that operate at intermediate temperatures (100-300°C) are rare. However, reasons to operate at these temperatures are manifold. Waste energy (heat) coming from resistive losses are generated at an intermediate temperature that makes it usable. Integrated systems using this higher quality heat can increase overall efficiency of a fuel cell system from roughly 50% to close to 80%. Furthermore, increased catalytic activity with less (expensive) catalysts is possible (Pt catalyst are used), because at these temperatures less catalyst poisoning by CO occurs, which reduces the requirements for the purity of the fuel and for the catalyst. Inherent to

intermediate temperature fuel cells is a water free conduction mechanism, removing the necessity of auxiliary systems to keep the system cool or moisturized. Due to operation at higher temperature also the relatively large cooling systems that are normally necessary to keep the operation temperature below 100°C need not be installed; cooling against ambient temperatures is easier when operating at higher temperatures. On the other hand when comparing operation at intermediate temperatures with high temperature solid oxide fuel cells, the materials demands are much reduced because the intermediate temperatures are relatively low, and startup times are reduced.

High protonic conduction at intermediate temperatures is found in solid acids [56, 58]. Typical for these materials is a superprotonic phase transition after which the material shows a jump in protonic conductivity of orders of magnitude [59, 60]. Above this phase transition, these materials have been shown to be applicable as fuel cell electrolyte [7, 61, 62]. Below this phase transition nanostructuring is applied to improve the ionic conductivity resulting in values approaching the superprotonic ones [13]. These are solid acidic materials that, in spite of their acidic nature, require no special heat or acid resistant construction materials. Solid acids generally can be represented with the chemical formula: $M_aH_b(XO_4)_c$, where M is a mono- or divalent cation (e.g. Rb, Cs), XO_4 is a tetrahedral oxy-anion (e.g. SO_4, SeO_4, PO_4) and a, b, c, are integers.

One particular solid acid is cesium hydrogen sulphate. Depending on temperature $CsHSO_4$ exhibits three crystalline phases, usually referred to phase III, II and I. Phase III and II are low proton conducting phases. Bulk crystalline $CsHSO_4$ phase II is a metastable phase at room temperature, which will gradually fall back to Phase III. At 414K $CsHSO_4$ goes through its superprotonic phase transition (from phase II to phase I) [63], which has a higher crystal symmetry and increased lattice dimensions. This allows for quasi free rotation of the SO_4 tetrahedra between crystallographically identical positions, creating six times as many possible proton sites as there are protons available. Proton diffusion occurs through combined rotation of the SO_4 group and jumps to the next SO_4 group [64], which is a fast process giving the material its high proton conductivity. For temperatures below 414K, $CsHSO_4$ has a monoclinic symmetry in which the number of protons is equal to the number of available proton sites (phase III and II). The hydrogen atoms are localized with rigid hydrogen bonds between SO_4 tetrahedra and their mobility is low [65, 66]. In ionic materials the mobility of ions strongly depends on the number of available vacant sites to which an ion can move. It is important in this respect that in the high mobility phase I many vacant sites are present while in the low mobility phase II all sites are occupied and mobility is only possible via exchange of ions.

In contrast to bulk material, where electro neutrality must be obeyed, at interfaces between ionic conductors a narrow charged zone, a so called space charge layer, is tolerable and even thermodynamically favourable [67]. Mobile charge carriers of the conducting phase can physically relocate themselves at the interface or in the alien

phase (leaving vacancies in the donating phase), creating oppositely charged space charge layers in the conducting matrix and nanoparticles. The deviation from charge neutrality creates an electrical field that limits the magnitude and spatial extent of the carrier redistribution. In the nanometer range, interfaces are so closely spaced that the space charge layers, which are usually extending on scales of nanometers (several times the Debye length) [20] partially overlap. The impact of the interfaces becomes increasingly significant until it dominates the whole material's properties such as the local ionic densities and conductivities [33]. In these materials the overall impact of the interfacial regions increases with decreasing nanoscale dimension. This leads to true size effects of the nano morphology (in contrast with trivial size effects) as an ion has a shorter diffusion path between phases when the dimensions are decreased.

Although the space charge effect is a widely accepted phenomenon, the effect on the ionic densities in nanostructured materials has to our knowledge never been determined directly by experiments sensitive to these densities. This also holds for the chosen solid acid or any other proton conducting material. Similarly, the effects of nanostructuring solid acids have been investigated previously through macroscopic measurements, but the microscopic, atomic scale defect densities occurring or the effect on the proton dynamics due to nanostructuring have not been probed directly on a microscopic level.

Here we perform a study with direct microscopic probes of the hydrogens on the effect of nanostructuring on dynamics, ionic densities and other structural factors, complementing the macroscopic measurements performed in other studies. Quasi Elastic Neutron Scattering (QENS) and Nuclear Magnetic Resonance (NMR) spectroscopy were performed on the $CsHSO_4$ solid acid and several of its nano composite samples. Both techniques directly observe the protons providing information about the dynamics as well as structural information. To investigate the proton densities neutron diffraction on deuterated samples has been performed. The solid acid has been chosen for this study because it has considerable promise as a fuel cell electrolyte above its superprotonic phase transition.

QENS and NMR measurements have been performed on bulk crystalline $CsHSO_4$ and nanocomposites thereof with SiO_2 and TiO_2. Different proton fractions with varying mobilities were observed between the bulk crystalline and nanocomposites. Also NMR on deuterated samples of the crystalline solid acid and nanocomposites with TiO_2 was performed. In the diffraction study the bulk crystalline solid acid and the nanocomposite thereof with TiO_2 nanoparticles in different sizes and molar ratios were investigated. TiO_2 is chosen as ionic conducting nanocrystalline filler because it is crystalline and therefore can provide structural information using neutron and X-ray diffraction. In a previous study nanoscaled TiO_2 was shown to be prone to hydrogen uptake in pure D_2SO_4 acid [68]. Nanoparticulate TiO_2 of a few different sizes, immersed in D_2SO_4 showed surprisingly large ionic densities at a specific position in TiO_2, namely [0.00, 0.75, 0.43] corresponding with a split

position of the deuterons inside the oxygen octahedron. Rietveld refinement showed occupancies at this position of 0.045 and 0.085 for TiO_2 particle sizes of 24nm and 7nm respectively, which translates in deuteron intercalation of 9% and 17%. Although $CsHSO_4$ is less acidic then sulphuric acid we will see that hydrogen insertion in TiO_2 still takes place and therefore vacancies are created in the solid acid.
Finally the experimental findings are being supported by initial simulation results using ab-initio methods (VASP).

4.2. Experimental Section

The solid acid Cesium Hydrogen Sulfate was synthesized by dissolving Cesium Carbonate (Cs_2CO_3) in demineralized water and slowly adding sulfuric acid (diluted) in the correct stoichiometry [69]. After recrystallization from a methanol/water mixture, the solid acid was filtered and dried in a vacuum oven. After careful drying a part of the $CsHSO_4$ was redissolved in demineralized water and TiO_2 or SiO_2 nanoparticles were added in known quantities. The solvent water was slowly evaporated under stirring. The nanocomposite samples created were then carefully dried in the vacuum oven and subsequently crushed in a mortar resulting in a powder.
The chemicals Cesium Carbonate [reagentplus, 99%] and the sulfuric acid [ACS reagent, 98%] were bought from Sigma-Aldrich. The nanoparticles used were: TiO_2 7nm [supplier: Nanoamor], 15nm [Nanoamor], 24nm [supplier: Evonik], 40nm [Evonik] and SiO_2 7nm [Aerosil300, Evonik] and 40nm [AerosilOX50, Evonik]. The TiO_2 nanoparticles were carefully checked on size, polydispersity and purity with TEM and XRD [70].
The QENS measurements were performed on bulk crystalline $CsHSO_4$ and nanocomposite $CsHSO_4$ with the following nanoparticles; TiO_2 (24nm), SiO_2 (7nm) and SiO_2 (40nm). The molar ratio between solid acid and nanoparticles was 1 to 2.
The nanocomposite with TiO_2 24nm was selected for a temperature dependent ^1H NMR scan ranging up to 433K and compared with the bulk crystalline sample. Other nanocomposite samples, (TiO_2 7nm, 40nm, SiO_2 7nm and 40nm) were measured at room temperature. For comparison with ^2H NMR again the (deuterated) nanocomposite solid acid with TiO_2 24nm was selected for the temperature scan. The deuterated samples were synthesized according to literature in a dry nitrogen environment.
Neutron diffraction data on the $CsDSO_4$ - TiO_2 nanocomposite samples were collected at room temperature on the high flux diffractometer Polaris at the pulsed spallation neutron source ISIS, Rutherford Appleton Laboratories, England. Deuterated samples were used to suppress the incoherent background caused by

protons. The nanocomposite samples consisted of the solid acid with the following particles: TiO_2 7nm, 15nm, 24nm and 40nm. Additionally the TiO_2 24nm composite had an extra sample with a molar ratio of 1:1 (acid:filler referred to as nano241) and the TiO_2 40nm sample had an additional sample with a molar ratio of 1:1/2 (nano401). Analysis was performed using the Rietveld refinement program GSAS.
The QENS experiments were performed on fully protonated samples on IN5 at the High flux reactor of the Institute Max von Laue-Paul Langevin (ILL), with an incident wavelength of 11.5 Å, a resolution function with a full width at half maximum of ~ 6 μeV and covering a Q range of 0.2 – 0.9 $Å^{-1}$. Air tight, flat, Al sample containers were used.
NMR measurements were performed at the solid-state NMR facility for advanced materials science, Radboud University in Nijmegen, The Netherlands. Using a 400 MHz spectrometer with a static magnetic field strength of 9.4 T, the ^1H and ^2H Larmor frequencies were 399.95 and 61.39 MHz respectively. The measurements were performed over a wide range of temperatures from 173K to 433K. A 3.2mm airtight zirconia rotor was used to measure the Magic Angle Spinning (MAS) ^1H or ^2H 1D spectra and spin-lattice relaxation times. The spinning frequencies were between 14 and 17 kHz.
Ionic conductivities were measured on thin pressed pallets of dry powder. A sputtered gold coating was used for optimal contact. Impedance spectroscopy was performed between RT and 160^oC and conductivities extracted. The results (not shown here) are fully in line with what others have reported [12, 26, 29, 62]. The superprotonic transition in a pure bulk $CsHSO_4$ sample shows the three orders of magnitude change in conductivity reported elsewhere [28], while in the composites the conductivity is much increased at low temperatures, leading to the strong reduction of the transition effects on the conductivity.

4.3. Results and Discussion

4.3.1 X-ray characterization of samples and presence of X-ray amorphous phase.

X-ray diffraction was performed to determine the structure and the amount of the crystalline phases formed. Figure 4.1 compares the diffraction of a part of the spectra for a bulk crystalline sample with several nanocomposite spectra. The peaks for the $CsHSO_4$ phase II are still easily observable but it is apparent from the patterns that the peaks become less pronounced (Figure 4.1a) – because there is less $CsHSO_4$ in the composites. However, peak broadening due to decrease of grain sizes in the solid acid phase did not occur either; normalizing the intensity of certain peaks (Figure 4.1b) showed no significant broadening of the peaks of the

nanocomposite sample compared to the peaks of the crystalline bulk samples. This could be a result of complete phase separation between solid acid and nanofiller, which seems unlikely in view of the large changes in proton mobilities. A more likely explanation could be that the nanostructured solid acid is structurally similar to the crystalline bulk sample with a coherently continuing crystal lattice around the nanofiller particles.

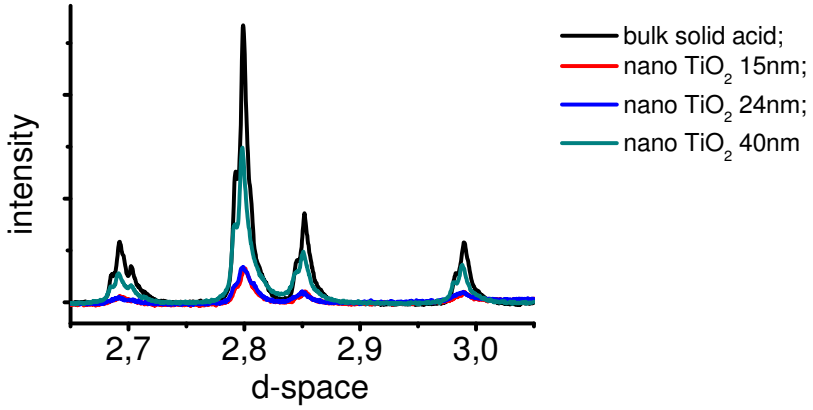

Figure 4.1a. Section of XRD spectra for bulk crystalline- and nano structured solid acid composites showing CsHSO4 peaks.

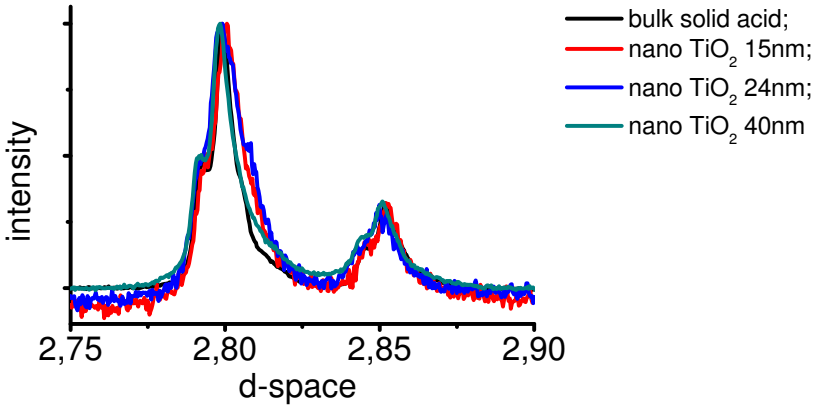

Figure 4.1b. Peaks normalized on intensity showing only limited broadening.

Rietveld analysis of the TiO_2 nanocomposites showed a discrepancy in most of the samples with respect to the ratio between the solid acid and nano TiO_2 filler phases, as there appeared to be much more crystalline TiO_2 present in the composite than was put in during synthesis. Flame Atomic Emission Spectroscopy (FAES)

measurements combined with Inductively Coupled Plasma Optical Emission Spectroscopy (ICP-OES) measurements however, showed the theoretical ratio of $CsHSO_4$ to TiO_2. This is evidence that during preparation of crystalline $CsHSO_4$ an X-ray amorphous phase of the solid acid is also formed. This depends on the presence of the nanofillers and possibly on factors like drying rate or temperature treatments. During the investigations we also observed that for the smallest nanofiller particles the amorphization progresses with time: Figure 4.2 shows 3 diffraction patterns taken in chronological order of a nanocomposite solid acid sample with 7 nm TiO_2 particles. The upper diffraction pattern is taken directly after synthesis, the middle one is taken several weeks afterwards and the lower spectrum several months thereafter. It can be seen clearly that the diffraction pattern in the middle has lost most of the reflections of the solid acid and the lower diffraction pattern shows no reflections belonging to the solid acid phase. Recrystallization of the latter sample results in a diffraction pattern similar to the upper one. This phenomenon was especially profound in the nanocomposites with the smallest nanoparticles and this leads to the conclusion that nanostructuring of the solid acid destabilizes the material so that it gradually turns amorphous, which is X-ray invisible. The first question is why the material becomes partly amorphous in the first place. Contributing factors are the abundant interfaces and the stresses exerted by them on the lattice of $CsHSO_4$. Below we will demonstrate that another important factor in these materials is that the crystalline matrix is altered due to the removal of protons under the influence of space charge effects. Furthermore the progressing destabilization of the solid acid resulting in the 'growth' of the amorphous phase will be aided by the significant mobility in the material at room temperature.

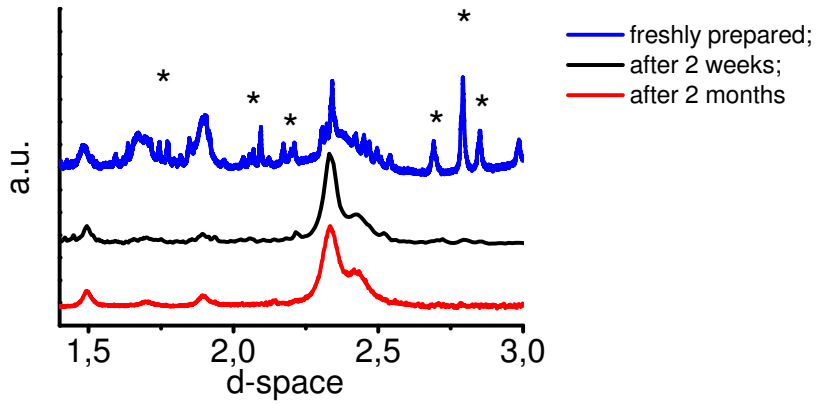

Figure 4.2. Time dependent amorphization of solid acid in nano CsHSO4 and TiO2 7nm composite. Several outstanding peaks belonging to the solid acid phase are being marked by an asterisk.

Another effect of the nanostructuring as seen by x-ray diffraction analysis is that, when formed, phase II of $CsHSO_4$ does not relax back to phase III. The aim of this research however is to study the mechanism that causes enhanced proton mobility in these samples. However, sufficient care was taken to minimize the amount of amorphous phase in order to make comparisons with bulk more straightforward.

4.3.2 Proton dynamics in $CsHSO_4$.

Quasi Elastic Neutron Scattering (QENS) is a direct probe of the time- and length scale of the mobility of protons in the material via respectively the measured energy- and momentum transfer spectra. Figure 4.3a shows QENS spectra of bulk crystalline $CsHSO_4$ and a nanocomposite sample of $CsHSO_4$ mixed with SiO_2 (7 nm) at several temperatures. The broadening at the foot of the peak is a direct indication of the mobility timescale of the protons in the material. As expected [64], the spectrum of the bulk material shows that at 390K its protons are fixed at their lattice positions, while at 463K in the superprotonic phase I they are highly mobile on the ps timescale probed. In contrast, the spectrum of the nanocomposite at 360K shows a proton mobility almost as high as the bulk material in the superprotonic phase at 463K. At 450K the protons possess an even higher mobility compared to the superprotonic bulk phase.

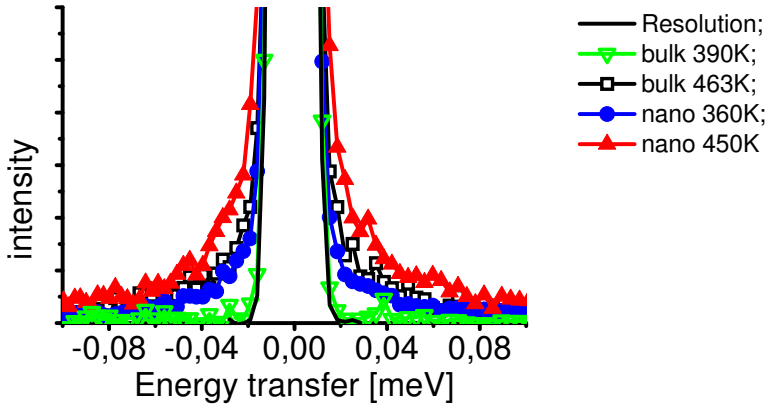

Figure 4.3a. Quasi elastic neutron scattering spectra of bulk $CsHSO_4$ and SiO_2 (7nm) nanocomposite samples with molar ratio 1:2 at Q = 0.61Å^{-1}. The bulk sample at 390K does not show broadening relative to the resolution function. Nanocomposite at 360K shows a signal comparable to the bulk at 463K. The nanocomposite at 450K shows an even broader quasi elastic signal.

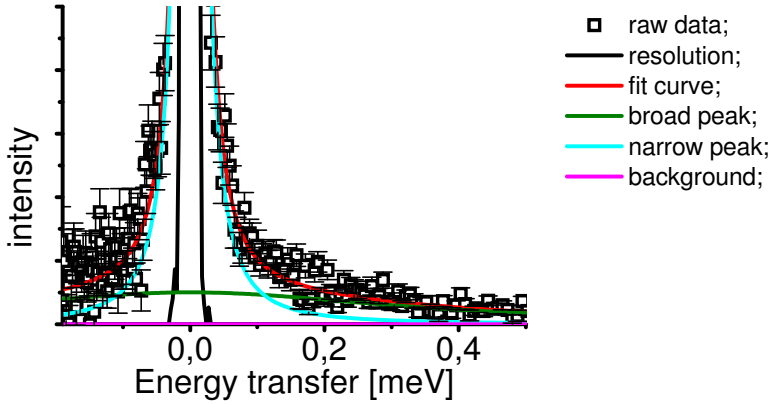

Figure 4.3b. Example of a raw QENS data fit using a convolution of two Lorentzian functions with the resolution function.

Analogous to Belushkin et. Al [64]. quantitative analysis of the spectra uses a convolution of two Lorentzian contributions and a delta function with the resolution function (figure 4.3b). The width of the narrowest Lorentzian shows Q^2 dependence down to small Q values (typically < 0.2Å^{-1}), indicating translational diffusion of the protons (where Q is the scattering vector, a basic quantity used in reciprocal space). The widths plotted in Figure 4.4a indicate that the addition of TiO_2 nanoparticles induces a motion which is on a timescale comparable to the superprotonic diffusive translational motion and which is surprisingly constant over the whole temperature range measured. The SiO_2 nanoparticles result in higher mobility compared to TiO_2 (comparing red and green curves) and smaller particles have more effect on line broadening than bigger ones.

Up to 25 percent of the protons in the low temperature composite phases show translational diffusion (figure 4.4b), whereas there is no sign of mobile protons in the signal of the bulk phase at low temperature (in agreement with) [64]. This mobile fraction will contribute significantly to the ionic conduction in the composite phase. It constitutes a large fraction of mobile protons because it is of the same order of magnitude as the fraction of mobile protons above the superprotonic transition.

While impedance measurements show an enormous increase in conductivity of the nanocomposite samples [28], it cannot provide insight into the microscopic dynamics and mechanisms of conduction. With QENS it is now directly observed that the protons not only are much more mobile in the nanocomposite at low temperatures, but that additionally there is a large fraction of protons that remain mobile when lowering the temperature.

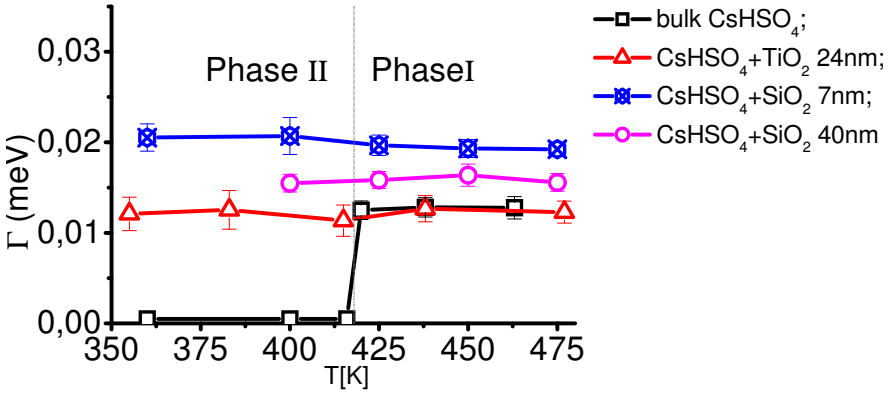

Figure 4.4a. Proton mobility at Q = 1 Å^{-1} for four different samples from QENS measurements. Right: mobile fraction from QENS measurements. Four different samples are bulk $CsHSO_4$, nanocomposite $CsHSO_4$ with TiO_2 24 nm particles, nanocomposite $CsHSO_4$ with SiO_2 40 nm particles and nanocomposite $CsHSO_4$ with SiO_2 7 nm particles. The linewidth (Γ) is a measure used to indicate proton mobility. For jump diffusion at small Q values Γ is related to the diffusion constant as follows:

$\Gamma(Q) = \hbar \frac{l^2}{6\tau} Q^2 = \hbar D Q^2$, where l is the jump length and τ is the residence time.

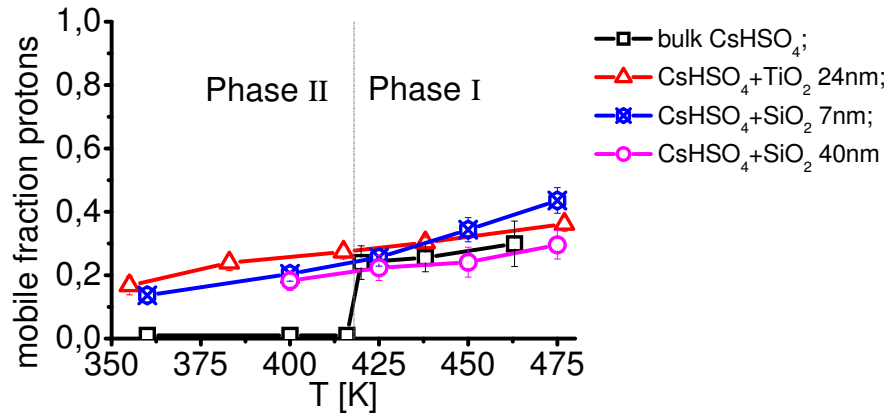

Figure 4.4b. Fraction of mobile protons as function of temperature from QENS measurements.

NMR proton spin lattice relaxation time (T_1) measurements at 400 MHz probe mobilities to within an order of magnitude similar timescales as the QENS measurements and are therefore complementary. The ^1H T_1 relaxation time in bulk $CsHSO_4$ shows a dramatic drop going through the superprotonic phase transition

from phase II to phase I. Using a model calculation, it was shown that in phase I of bulk $CsHSO_4$ T_1 is directly related to the translational motion of hydrogen [59, 65]. The protons undergo a two step diffusion process that involves both a change in orientation of SO_4 groups as well as a transfer between the SO_4 groups. The low values of the T_1 times is caused by the rapid fluctuations of the nuclear dipolar interactions between hydrogens and hydrogen and Cs that result from the three dimensional diffusive motion. In the bulk phase II the diffusion has slowed down orders of magnitude, and the motions are characterised by intra hydrogen bond hopping of protons as well as reorientation of the O-H…O hydrogen and chemical bond [66, 71]. Because the hydrogen bonded network in phase II is represented by zig-zag infinite chains, these motions can be characterized as one dimensional. However, with increasing temperature the reorientations cause the transfer between different chains, leading to more two dimensional motions already below the superionic phase transition [71].

In our experiments the measured bulk crystalline proton T_1 times are in good agreement with literature (differences can be explained by differences in the applied field strength) [65, 66, 72]. In agreement with the rapid diffusive signal observed in the neutron data, the relaxation rates of the nanocrystalline material with TiO_2 24nm particles (figure 4.5) are for a large fraction of the protons orders of magnitude smaller than the corresponding bulk values over the whole temperature range accessed. This again shows that in the nanostructured composite high proton mobility is induced. However, there is also a part of the protons that show long T_1 relaxation times, similar but still roughly two times shorter than the protons in the bulk crystalline phase. This shows the inhomogeneity of the mobility in the sample.

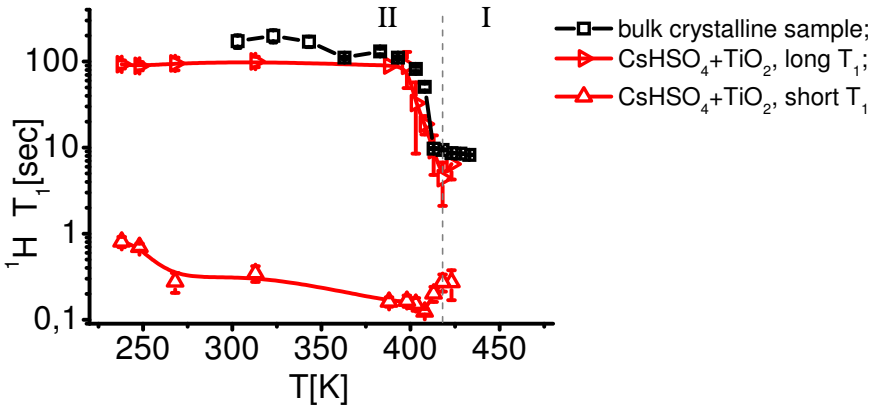

Figure 4.5a. T_1 relaxation times of protons in bulk crystalline $CsHSO_4$ and nanocomposite $CsHSO_4$ with 24 nm TiO_2.

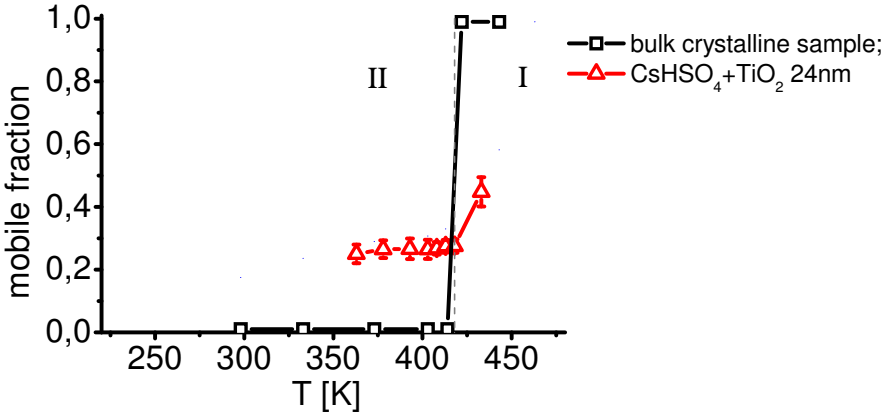

Figure 4.5b. Fraction of mobile protons as function of temperature from NMR measurements.

Further analysis of the ^{1}H NMR spectra showed 2 peaks (figure 4.6a); One at 11.0 ppm, which is expected for the solid acid in phase II [73] and a second peak in a lower ppm region. The second peak is a result of the nanostructuring, since it is absent in the bulk crystalline sample. The position and width of this peak is dependent on the type of nanoparticle used. SiO_2 nanoparticles result in a position around 6.0 ppm and TiO_2 particles give rise to a peak around 6.6-7.4 ppm. In general the large chemical shift at 11 ppm indicates strong deshielding in the solid acid which is caused by the electronegativity of the SO_4^{2-} group. The lower chemical shift peak observed in the composites indicates a higher shielding i.e. less electron density withdrawn from the protons in this environment. In general this would also mean that these protons are in a less acidic environment. In view of the presence of the amorphous phase the peaks at lower ppm are initially attributed to protons in this amorphous phase surrounding the nanoparticles. The shift to lower acidity could be explained by the fact that fewer protons are present in the amorphous phase due to exchange with protons at the surface or in the nanoparticles (present as result of space charge effects, see below). The lower chemical shift value of the amorphous phase in the SiO_2 composite then suggests that SiO_2 is a better 'proton acceptor' (less acidic) than TiO_2 (more acidic). Below it is shown that indeed ^{2}H can be observed inside the TiO_2 phase, as was previously demonstrated for TiO_2 nanoparticles immersed in liquid D_2SO_4 [24].

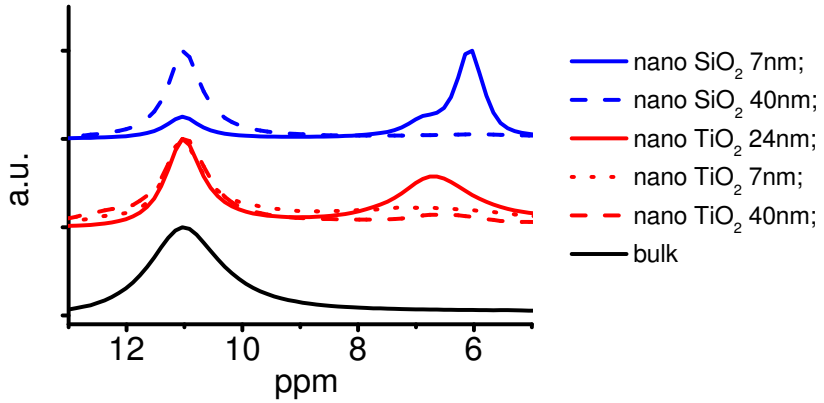

Figure 4.6a. Proton MAS NMR spectra of bulk and nano composite samples with SiO_2 or TiO_2 nano particles showing peaks at 2 different chemical shift regions.

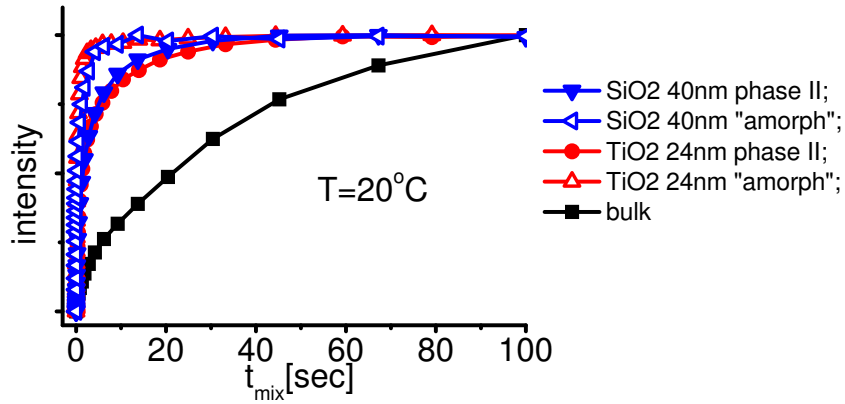

Figure 4.6b. T_1 saturation measurements of bulk, nano composite solid acid with 40 nm SiO_2 and nano composite solid acid with 24 nm TiO_2.

Shown in the right plot of figure 4.6 are results of T_1 saturation measurements of nano composite solid acid with 40 nm SiO_2, 24 nm TiO_2 and the bulk samples showing the intensities of the spectra at certain mixing times. The nanocomposite samples each have two lines representing the phase II (open symbols) and the amorphous/exchanged (closed symbols) peaks. Clearly it can be observed that the phase II peaks of the nano samples possess a short component and a longer one.
Table 1 shows the proton T_1 times of the different samples. The peak assigned to amorphous/exchanging $CsHSO_4$ in the composites (around 6-7.4 ppm) at room temperature was generally well represented by two short T_1 contributions; a longer one around 1 second and a much shorter one, which was dependent on the type of

particle used. One might therefore relate the shorter component to the protons in or at the nanoparticles, as they are observed in neutron diffraction, and the longer T_1 component to the protons in the amorphous $CsHSO_4$. In any case the strongly reduced T_1 clearly shows the enhanced proton mobility in the composites due to nanostructuring. In view of this mobility one should expect also exchange of protons between different regions in the sample that can bring T_1 values together and can influence spectral shapes, depending on the exchange rates. The phase II peak (11 ppm) also shows two T_1 values: a long component in the same order as the bulk phase II T_1 time (roughly around 10 seconds), but, most remarkable, also a component with values in the order of the T_1 time found in the amorphous signal (less than 1 second). Note that this short T_1 time in the crystalline Phase II peak is even slightly shorter than the long T_1 time in the amorphous phase and much shorter compared to the bulk T_1 times of around 40 seconds. This indicates that also the crystalline phase II is influenced by the nanostructuring or rapidly exchanging protons with the shortest T_1 protons in the sample.
The SiO_2 7 nm composite sample differs from the other samples as it does not possess any long T_1 component. This shows that the nanostructuring is able to influence the whole composite sample, increasing the mobility.

sample	$T_{1\text{-}1}$ peak 1 [sec]	$T_{1\text{-}2}$ peak 1 [sec]	$T_{1\text{-}1}$ peak 2 [sec]	$T_{1\text{-}2}$ peak 2 [sec]
Bulk crystalline $CsHSO_4$	42	--	--	--
Composite TiO_2 7 nm	15	0.12	1.0	3.4e-2
Composite TiO_2 24 nm	10	0.62	1.0	0.20
Composite TiO_2 40 nm	10	1.0	1.5	0.15
Composite SiO_2 7 nm	0.50	6.0e-2	4.8e-2	3.1e-3
Composite SiO_2 40 nm	4.5	0.26	1.3	6.2e-3

Table 1. NMR proton T_1 times

In the upper two spectra in figure 4.6a two extreme cases of nanostructuring are depicted. The dashed spectrum represents the nano solid acid composite with 40 nm SiO_2 and the solid line represents the composite with 7 nm SiO_2 nanoparticles. The composite with 40 nm particles shows almost no peak around 6 ppm, while the 7 nm composite shows a relatively small peak in the 11 ppm region. This apparent randomness in intensities of the peaks is attributed to the preparation procedure. With proper care, the samples can be made fully crystalline or amorphous. In this 40 nm composite SiO_2 sample, the high proton mobility, observed with QENS and T_1 measurements therefore can be totally attributed to the protons in the crystalline phase. In conclusion, therefore, the presence of the amorphous phase alone does not explain the altered proton mobility.
Observation of the upper solid spectrum (7 nm SiO_2 nano composite) reveals a second peak in the amorphous phase region around 7 ppm. The origin of this peak is

not known precisely, but it could come from protons in the amorphous phase, while the second and larger peak is a result of protons at the surface or inside the nanoparticles.

4.3.3 Deuterated solid acid.

For investigation of proton densities in the solid acid using diffraction techniques, deuterium is much more suitable than hydrogen. To investigate the motions of hydrogen in the composites in more detail the deuterium isotope is also used, as this nucleus has a sizeable quadrupole moment which interacts with the local electronic distributions.

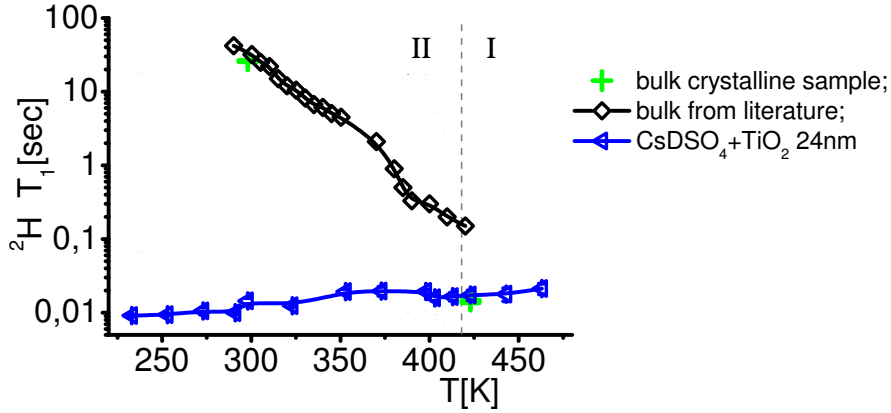

Figure 4.7a. Shortest observable proton relaxation times (T_1) of deuterium ions in bulk (taken from literature [66] and own work) and nanocomposite of $CsDSO_4$ with 24nm TiO_2 nanoparticles.

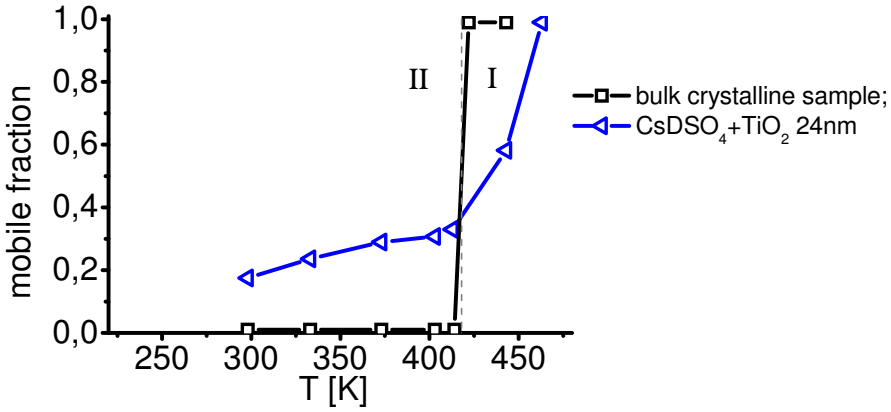

Figure 4.7b. Fraction of deuterium ions having a short T_1, i.e. showing high mobility, in bulk and in nanocomposite $CsDSO_4$.

Figure 4.7a shows the T_1 times of deuterated solid acid samples. Our bulk sample shows similar T_1 values as have been published in much detail in literature [66]. In the composites there is a prominent fraction of the signal that has a short T_1, just as for the protonated samples.
Comparing figures 4.5 and 4.7 it can be seen that the T_1 times of the nanocomposites are an order of magnitude shorter than the T_1's of the proton measurements. Three factors are responsible for this result. First the T_1 relaxation mechanism is now due to the strong fluctuating quadrupolar interactions, instead of the mainly dipolar interactions for the protons. Second, the lower Deuterium resonance frequency in the same applied field means that slower timescales are probed. Third, the isotope effect causes motions to occur on longer timescales. However, from these differences it is clear that there still is the same behaviour: short T_1 above the superprotonic transition in bulk samples, and a significant fraction of the Deuterium that have a short T_1 on all temperatures measured, i.e. also below the transition temperature. Also the mobile fractions found are quite similar to the proton results.

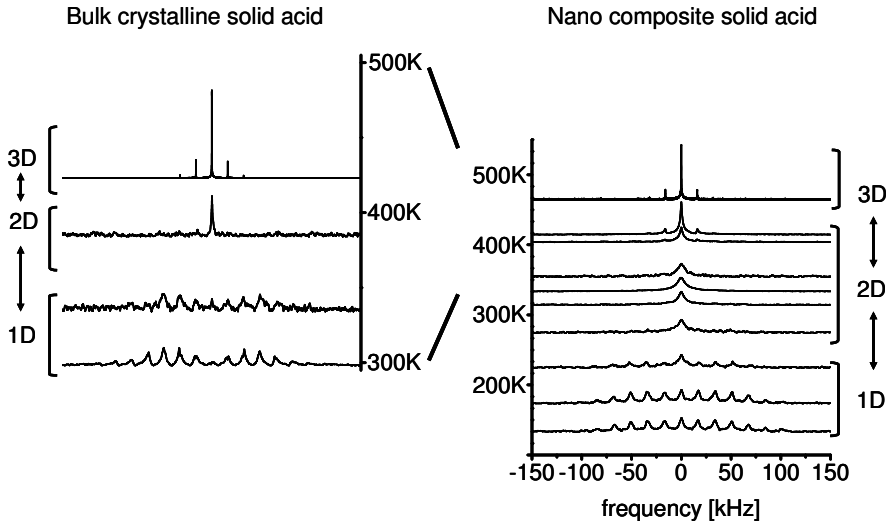

Figure 4.8, left: ^2H MAS NMR spectra of bulk crystalline $CsDSO_4$ for different temperatures. Right: nanocrystalline $CsDSO_4$ with 24 nm TiO_2 particles. The spectra display spinning sideband patterns reflecting the size and symmetry of the ^2H quadrupolar interaction.

Analysis of the ^2H NMR spectra leads to additional insight into the solid acid because the spectra are strongly influenced by quadrupolar interactions that probe the surrounding of the Deuterium nuclei. Figure 4.8 shows the deuterium MAS NMR spectra performed on bulk and on a 24nm TiO_2-$CsDSO_4$ composite. The temperature dependence of the bulk solid acid is in complete agreement with

literature [66]. Already below the superprotonic transition there are specific motions on the timescale probed by the spin precession. From the analysis of single crystal Deuterium NMR [66] it was found that around 385 K the bulk NMR spectrum alters because the Deuterium dynamics change from motion along infinite 1D zigzag chains to motions on a progressively more 2D network. This leads to narrowing of the apparent quadrupolar spectrum. After the superprotonic phase transition temperature the H/D movement takes place on a truly 3D network. The experiments thus show spectra evolving from broad multi sideband spectra (referred to as 1D region) to a single, broadened peak (2D) to very sharp peaks with sidebands in phase I (3D). Compared to the bulk crystalline phase, the nanocomposite solid acid shows a strongly modified temperature dependence. Already at 273K the sidebands disappear and a single broad peak remains. This is at a much lower temperature than in the bulk solid acid. From the settings of the experiment it is clear that we measure both Deuterium in the amorphous/exchanged phase as well as Deuterium in the crystalline phase II or I (depending on the temperature); the fraction of Deuterium in the crystalline phase II that has a long T_1 is suppressed because of the rapid scan rate, but the fraction with a short T_1 is not suppressed. However, discrimination in the spectra between crystalline and amorphous phases is not possible on the basis of the different chemical shifts, basically because of the broad lines that are present. In any case the temperature range between (roughly) 273K and 400K shows essentially a single broad peak, as is observed in the bulk sample around 385K. It is natural to assume similar mechanisms for motion in the crystalline but nanostructured, as well as in the less ordered X-ray amorphous part of the material, but then the transition of 1D to 2D motions has to take place at much lower temperature than before. For this reason the temperature ranges in which the Deuterium motions in the crystalline fraction of the material are mainly 1, 2, or 3D are indicated in figure 4.8. In the 1D (low temperature) region of the nano composite material the measured quadrupolar broadened MAS spectra possess possibly a smaller overall width, leading to a total spectrum which has more intensity in the centre. The lower width, i.e. lower quadrupolar interaction, could indicate that less strong hydrogen bonds are present, leading to less asymmetry in the electron cloud surrounding the Deuterium nuclei. This is consistent with the observation of lower proton chemical shifts measured in the protonated samples. A more detailed analysis lies outside the scope of this manuscript.

4.3.4.1. Deuterium ion intercalation in TiO_2.

Analogous to the model study with liquid D_2SO_4 and TiO_2, in which deuterium ion densities were observed in the TiO_2 nano particles, neutron diffraction measurements were undertaken on the nanocomposite solid acid samples with TiO_2 nanoparticles. Space charge in the composites is modelled as intercalated deuterium nuclei in the TiO_2 lattice [24] and vacancies in the $CsDSO_4$ and fitted as such in the neutron diffraction data using GSAS. The diffraction intensities give direct information on the position and quantity of the Deuterium in TiO_2 and vacancies in the crystalline fraction of $CsDSO_4$. The high quality data (figure 4.9) make it possible to observe small effects on the diffraction intensities caused by nanostructuring. Fitting of the $CsDSO_4$ phase was complicated by the induced effects of nanostructuring, for example, vacancies in the lattice leading to local, structural distortions, in addition to the presence of TiO_2 diffraction peaks. Therefore the errors on the results extracted from these fits are relatively large for $CsDSO_4$. As the TiO_2 lattice hardly changes upon Deuterium insertion, the error margins here are much smaller.

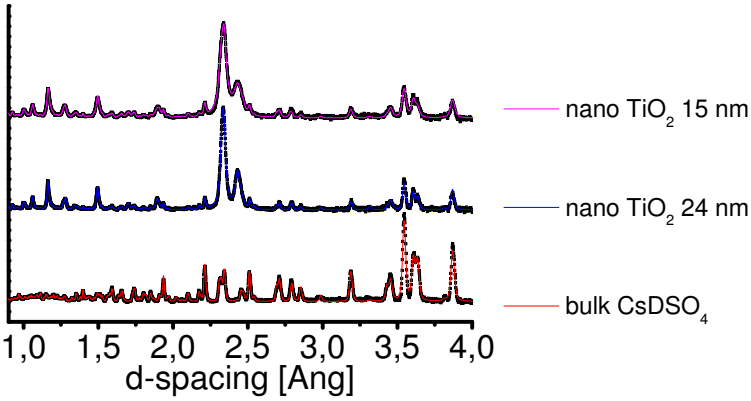

Figure 4.9. Neutron diffraction spectra of bulk and 2 nano samples (TiO_2 15 and 24 nm, $CsDSO_4$: TiO_2 = 1:2), with fitted curve.

The solid acid at room temperature of a fresh sample (i.e. no relaxation towards phase III yet) shows the monoclinic crystalline phase II and could be fitted well, with total wRp values around 0.02 (table 2). As in the model study, here also deuterium ions were observed in the TiO_2 lattice. These deuterium ions could only be a result of deuterium ion migration from the solid acid phase, TiO_2 acting as a hydrogen ion acceptor. From the fitted deuterium concentrations a correlation between the number of intercalated deuterium ions and the sizes of the TiO_2 nanoparticles is observed and plotted in 4.10. With decreasing particle size, very high deuterium ion densities of up to 10% intercalation in TiO_2 were found. When

comparing with the liquid acid D_2SO_4 deuterium ion intercalation, this is still almost a factor of 2 lower. This is explained by the lower acidity of the solid $CsDSO_4$ acid compared to the liquid D_2SO_4 acid.
The position of the intercalated deuterium ions in the TiO_2 (table 2) was found to be around [0.00 0.75 0.43] with a temperature factor around 0.04 $Å^2$, in agreement with the previous model study, and also in agreement with ab initio calculations. No constraints were needed for fitting this position in the different samples, except for the 40 nm particles.

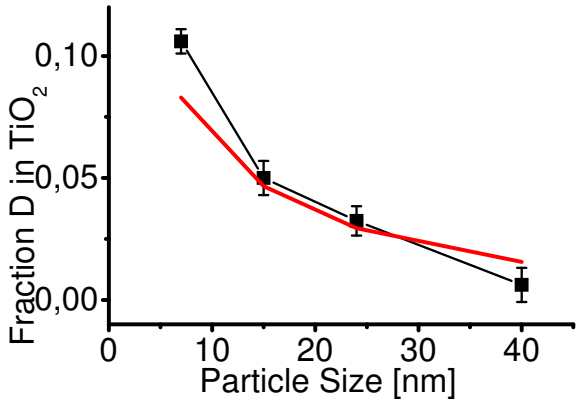

Figure 4.10. Fraction of Deuterium ions intercalated in the TiO2 lattice as a function of the nanoparticle size.

Sample	wRp	Fraction D in TiO_2 [%]	Fraction D out SA [%]	Position in TiO_2	Grain size SA [nm]
bulk	0.0176	--	--	--	--
Nano7	0.0165	10.6±0.5	22±2	0.43±0.01	--
Nano15	0.0144	5.0±0.7	18±2	0.43±0.02	70±6
Nano24	0.0218	3.2±0.6	12±2	0.43±0.01	150±6
Nano241	0.0190	4.3±0.6	5.6±2	0.43±0.01	160±6
Nano40	0.0202	0.36±0.7	1.0±2	0.43	110±7
Nano401	0.0195	1.8±0.7	0.9±2	0.43	280±7

Table 2. Overview Parameters Rietveld Refinement

The effect of the deuterium ion intercalation is also found to be dependent on the molar ratio between the solid acid and the nanoparticles (see table 2). With increasing relative molar amount of TiO_2, the number of inserted deuterium ions in TiO_2 was found to decrease for identically sized nanoparticles, while the vacancy concentration in $CsDSO_4$ seems to increase. This behaviour is intuitively clear since more TiO_2 means that more deuterium ions can be extracted from the $CsDSO_4$,

however, progressive extraction of deuterium from $CsDSO_4$ will be less energetically favourable so the average concentration of deuterium ions in TiO_2 should become lower.

4.3.4.2. Apparent morphology.

Surprisingly, the addition of the small nanoparticles does not seem to impose apparent grain sizes for the solid acid phase that are equally small, observed from the diffraction line widths. However, smaller sizes are noticeable upon addition of the smallest nanoparticles below 24 nm, as shown in table 2. This means that the solid acid structure continues coherently for larger characteristic distances, in spite of the presence of 70 mol % of nanoparticles dispersed through the composite. During preparation all materials have been continuously mixed and the nanoparticles alone have sufficient volume to fill the volume taken up by the sample in a hard sphere packing scheme. Combined with the knowledge of the presence of the amorphous phase and the high intrinsic mobility throughout the materials, we postulate a process for the formation of the nanostructured samples.

After dissolving the solid acid, the nanoparticles are dispersed in the liquid. The solvent water is slowly removed by evaporation. At a certain point the solid acid starts to solidify or crystallize on nucleation sites on the nanoparticles. These solid phases may be amorphous at the start because of perturbing interactions from the TiO_2 / SiO_2 surfaces, either through lattice strains or because of the exchange of protons between the phases. When the layer of solid acid becomes thicker the influence of the nearby nanoparticle surface reduces and the normal crystalline solid acid can start growing. Because this starts from the many different nucleation centres present in the solid acid, phases only keep growing until they confront other solid material (nanofiller or solid acid). The growth of the coherent lattice is facilitated by the high mobility in the material and the annealing that results already at room temperature, giving the relatively large coherent grain sizes, observed by neutron diffraction.

Throughout this coherent phase there will be pockets with the amorphous phase grown around the nanoparticle in a core-shell fashion. The whole picture combined means that the morphology of the nanocomposites is such that the large grains of the solid acid are perforated like a Swiss cheese by small nanoparticles with a shell of amorphous solid acid around them. For the very small nanoparticles the X-ray data above indicate progressive amorphization with time. Sufficient protons are removed from the solid acid to make it X-ray amorphous throughout. The annealing process seems to be contradictory to the amorphization described above. A possible explanation lies in the difference in timescales of these processes, with the amorphization occurring at a much longer timescale.

Attempts to observe the morphology using (cryo) TEM were ineffective, because the samples were not stable under the electron beam, showing rapidly moving objects floating around, related to the high intrinsic mobility in these samples.

4.3.4.3. Induced HSO_4 movement.

Besides the direct intercalation of deuterium ions in the TiO_2 lattice, other effects as a result of the nanostructuring in the conducting solid acid phase were studied. By creating Fourier density maps from the diffraction peak intensities, selected nuclear densities could be observed. It was found that the nuclear densities around the nanocomposite oxygen atoms in the SO_4 tetraeder showed a much more ellipsoidal shape compared to the bulk oxygen densities (figure 4.11), indicating increased librational motions or static displacements of the oxygen atoms in the tetrahedra. Although we assume that there is an amorphous layer in between the crystalline solid acid phase and the nanoparticles, it is clear that due to the nanostructuring, the crystalline part of the solid acid is influenced by the space charge effects, that is protons from the stiff hydrogen bond network of phase II are released conferring orientational freedom on the SO_4 groups. The extraction of protons from the solid acid phase may also destabilize the matrix, favouring amorphization as observed with the x-ray characterization.

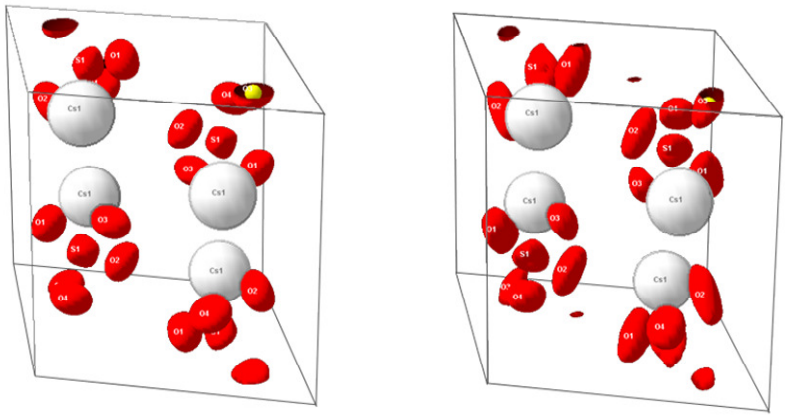

Figure 4.11. left: Fourier maps of nuclear density of bulk $CsHSO_4$. Right: Fourier maps of the nanocomposite with 24nm TiO_2. The levels of the oxygen and Cs isosurfaces are the same. In the nanocomposite the O nuclear densities have more elongated shapes due to positional and dynamic disorder.

4.3.4.4. Ab-initio calculations.

Results from first-principles DFT calculations (further details are reported in [23]) agree well with the determined values for ion insertion in TiO_2, approaching values to within roughly a factor 2 as illustrated in figure 10 by the red line. Important to state here is that also based on theoretical considerations such large proton insertion densities as found here experimentally, can be justified. The essential factor that determines the observed high proton insertion densities is the negative enthalpy of formation for creating defects that involve the transfer of protons from $CsHSO_4$ to TiO_2 or SiO_2.

4.4. Conclusions

The effects of nanostructuring the solid acid $CsHSO_4$ with proton accepting TiO_2 and SiO_2 nanoparticles on the mobility and the mobile fraction of the charge carriers have been observed using direct microscopic probes. Large fractions of protons are mobile at all temperatures measured, and the timescales of motion are much shorter than in the bulk material. This high microscopic mobility underpins the increase in conductivity by orders of magnitude below the superprotonic transition to phase I.

Direct experimental proof of the occurrence of space charge effects in the nanocomposite proton conductor $CsHSO_4$ and nanoparticulate TiO_2, have been shown in the form of deuterium ion intercalation in TiO_2 nanoparticles and Deuterium depletion in $CsDSO_4$. The scale of intercalation is quite substantial up to 10% in 7nm TiO_2 particles. The intercalation is size dependent, decreasing with increasing particle size due to decrease of surface/volume ratios. Though the measurements were done on a solid acid composite, the occurrence of space charges in other systems of proton conductors and nanoparticles is expected to be more general.

Combining the neutron and NMR results yields the following overall picture of the ionic mobility induced by nanostructuring. Due to the space charge effect, vacancies are created in the solid acid at temperatures below the superprotonic phase transition temperature, which allow a large fraction of the hydrogen ions to become as mobile as they are in the superprotonic phase (which has abundant intrinsic vacancies) because there are empty sites available to which ions can move. The vacancies already introduce the high mobility at temperatures approximately 140 degrees lower than observed in bulk. This behaviour also occurs in the amorphous phase, as observed by NMR.

The crystalline part of the solid acid is influenced by the space charges as is observed from enhanced vibrational motions in the SO_4 groups, and from the short ^1H NMR T_1 relaxation times of the bulk crystalline peak (at 11.0 ppm). A fully crystalline nano composite sample was shown to exhibit a similar degree of mobility

compared to a mostly amorphous nano composite sample, as a large fraction of the phase II peak in the NMR spectrum showed a short T_1 time.
The space charge effect in the crystalline bulk phase destabilizes the phase as evidenced by the SO_4 reorientations. This rotational degree of freedom may also contribute to the gradual time dependent transformation of the crystalline phase to the X-ray amorphous phase upon decreasing particle sizes.
Further analysis of the data showed the grain sizes of the solid acids to be roughly a few times bigger than the added nanoparticles. The nanoparticles however, are present in a large space filling quantity. Morphologically this leads to the conclusion that the nanocomposites consist of relatively large solid acid grains, perforated by nanoparticles with an amorphous shell surrounding them. Spontaneous annealing, aided by the high intrinsic mobility, causes larger coherent domains of the solid acid structure.

Acknowledgements
Supporting Information is available online from Wiley InterScience or from the author. Financial support for ISIS beam time was obtained from the Netherlands Organization for Scientific Research (NWO). NWO is furthermore thanked for their financial support of the solid-state NMR facility for advanced materials science at the Radboud University in Nijmegen. This article is the result of joint research in the Delft Research Centre for Sustainable Energy and the 3TU. Centre for Sustainable Energy Technologies. J. van Os, G. Janssen and H. Janssen are acknowledged for technical support with the NMR measurements. The Institute Laue-Langevin is acknowledged for QENS measurement time on IN5.

Chapter 5.

Polymer enhanced solid acid membrane electrolyte

This Chapter is based on the submitted paper:
Highly conductive Solid Acid impregnated Nafion composite fuel cell electrolyte membrane

W.K. Chan, H.C. Patel, T.J. Dingemans, S.J. Picken, and F.M. Mulder

Abstract
A composite electrolyte of solid acid impregnated Nafion is synthesised, exhibiting high proton conductivity above 100 ^{o}C in the inserted, dry and amorphous solid acid (10^{-3} S/cm at 140 °C).

5.1. Introduction

The polymer electrolyte membrane (PEM) fuel cell is currently the most investigated among the fuel cell types for mobile applications. Their superior applicability compared to the competitors lies in their high power density, low weight and volume, fast startup times and low sensitivity to orientation. The fuel cell technology is well established and mature enough to be applied in the automotive industry [57]. A main component of interest in the PEM fuel cell is the polymer electrolyte. The industry standard currently is Nafion, which is based on chemically

stabilized perfluorosulfonic acid/PTFE copolymer in the acid form. The strengths of this polymer electrolyte are stability, selective ion permeability and high proton conductivity. The sulfonic acid group supplies the protons that are conducted through a Grotthus mechanism in the water filled channels. These channels are roughly 4 nm wide [74] and easily accessible for H_3O^+ ions. An important limitation for the operating conditions of Nafion, however, lies in these water filled channels. The presence of water limits the operation temperature to 100 °C, since the cell needs to be humidified at all times in order to keep the electrolyte's high conductivity. From the application point of view several factors make operation at higher temperatures (140 – 200 ^oC) highly desirable. First, higher temperature operation simplifies cooling of the fuel cell and also offers the opportunity to raise efficiencies by producing better quality waste heat. Second, at higher temperatures the catalyst is less sensitive to CO poisoning, reducing fuel purity and catalyst constraints.

Solid acids attract attention for application as fuel cell electrolytes [7, 9]. These materials are inherent solid proton conductors and generally possess high proton conductivity above their superprotonic phase transition. This means that proton conduction in these materials does not rely on the presence of water and takes place at temperatures above 100 °C. An additional benefit is that they are impermeable to H_2, O_2 and methanol. However, these materials show low conductivity at temperatures below the superprotonic phase transition temperature. Also, they are water soluble and possess low mechanical stability.

The low ionic conduction of these materials at temperatures below the superprotonic phase transition temperature can be improved significantly by nanostructuring the material, which leads to orders of magnitude increases in conductivity making them applicable as fuel cell electrolytes. In this study, we combine the Nafion membrane with the solid acid proton conductor by filling the channels of the membrane with the solid acid Cesium Hydrogen Sulfate ($CsHSO_4$). $CsHSO_4$ has its superprotonic phase transition at 141 °C [75, 76]. However, in its nanostructured form also the low temperature conductivity can be high [25, 28, 29]. The resulting membrane is tested for its conductivity in both dry and wet conditions from 20^oC up to 140 ^oC.

5.2. Experimental Section

The solid acid was synthesized according to literature [69]. The chemicals Cesium Carbonate (reagentplus, 99%) and Sulfuric Acid (ACS reagent, 98%) were bought from Sigma-Aldrich and mixed in the correct stoichiometric ratio to form Cesium Hydrogen Sulfate. The $CsHSO_4$ was dried carefully and characterized afterwards with X-ray diffraction (XRD) and differential scanning calorimetry (DSC). The Nafion membrane, Nafion 117, was also bought from Sigma-Aldrich. Impregnation

was done by filling the channels of Nafion with a dilute solution of solid acid in demineralized water. A weighed piece of dry nafion membrane was put in a predetermined amount of solid acid in the solution. Evaporation of all the water afterwards leaves the solid acid in the channels. After drying the nafion membrane doubled in weight with only small amounts of solid acid settled on the outside surface of the nafion membrane. These were wiped off and weighed to ensure the composition of the solid acid nafion composite membrane.
The membrane was characterized by XRD spectroscopy and DSC. X-ray Diffraction measurements were performed on a Panalytical X'pert Pro diffractometer. DSC measurements were performed on a Perkin Elmer DSC 7 with a scan rate of 10 degrees per minute. Nuclear Magnetic resonance (NMR) spectroscopy was done to study the protons at the microscopic level. The NMR measurements were performed using a 400 MHz spectrometer with a static magnetic field strength of 9.4T. The measurements were performed statically. Proton spectra and spin-lattice relaxation times were measured. Ionic conductivity was determined by impedance spectroscopy. Impedance measurements were performed using an Alpha High Resolution Dielectric Analyzer under a dry nitrogen atmosphere. To ensure good contact between the membrane and the electrodes, layers of gold were sputtered on both sides of the membrane. Prior to the actual measurements, the setup was cycled several times between 25 °C and 130 °C. To compare the composite membrane with the commercialized standard, which operates at high humidity, additional impedance measurements in high relative humidity were performed. For the humidified measurements a special cell was used in which a relative humidity of 70% was maintained.

5.3. Results and Discussion

The amount of the solid acid in solution plays a significant role in the filling rate of the Nafion channels. A solution of 60 wt% of the solid acid with respect to the weight of the dry Nafion membrane was found to give the highest filling rate. Membranes consisting of up to 53 wt.% solid acid were prepared in this manner. Using a bulk density of the solid acid of 3.35 g/cm^3 as indication of the volume, results in 38 vol.% of solid acid in the membrane. The pore volume of Nafion based on water uptake of nafion is determined to be around 38-40 % [74, 77]. This would indicate that the channels are almost completely filled.

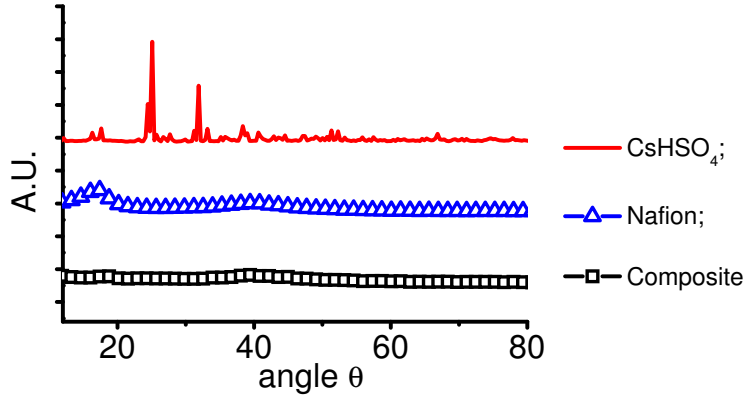

Figure 5.1a. X-ray Diffraction data of solid acid, Nafion, and Solid acid nafion composite membrane

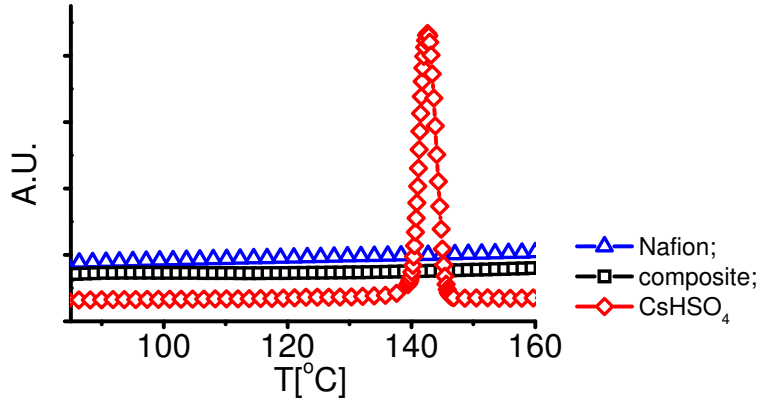

Figure 5.1b. Differential Scanning Calorimetry measurements of Nafion, solid acid nafion composite membrane and solid acid.

The XRD measurements shown in fig 1a show that the solid acid inside the Nafion pores is XRD amorphous in the impregnated sample. Compared to the Nafion sample the composite Nafion peak at around 17° is changed in appearance and position, and is much lower in intensity. In pure Nafion this peak is commonly attributed to the convolution of a peak resulting from hexagonal ordered crystalline domains in Nafion ($2\theta \sim 18^{o}$) and a peak that is referred to as resulting from an amorphous halo ($2\theta \sim 15^{o}$) associated with the PTFE backbone [78, 79]. One may state here that the peak at ~18° is still present while the amorpous signal has reduced. The latter will be a resultant from the altered contrast between the $CsHSO_4$ filled pores and the PTFE backbone; it can hardly be a result from the reduction of the amount of amorphous polymer material.

DSC measurements of the solid acid Nafion composite are plotted and compared with the bulk crystalline solid acid in fig 1b. In the nafion composite there is no phase transition of $CsHSO_4$ throughout the temperature range upto 240 °C. This again confirms absence of crystalline ordered solid acid within the polymer composite.

Results of the impedance measurements on the nafion membrane, the crystalline solid acid and the composite membrane are shown in figure 5.2. Conductivity in S/cm is plotted as function of temperature. The measurements were performed on thoroughly dried samples under a dry nitrogen atmosphere, and on humidified samples. The composite membrane under dry conditions shows an overall increase in conductivity compared to the separate components; close to two orders of magnitude compared to the crystalline solid acid and one order of magnitude relative to the dry Nafion membrane. The increased proton conductivy partially can be explained by the fact that amorphous solid acid possesses a higher proton conductivity than the crystalline form. However, previous reports have shown that proton mobility of solid acids is greatly influenced by nanostructuring [24, 80-82] through space charge effects. Since the channel sizes of nafion are of the order of a few nanometers, it is reasonable to assume interactions occurring between the solid acid and the nafion matrix leading to such nanosize effects.

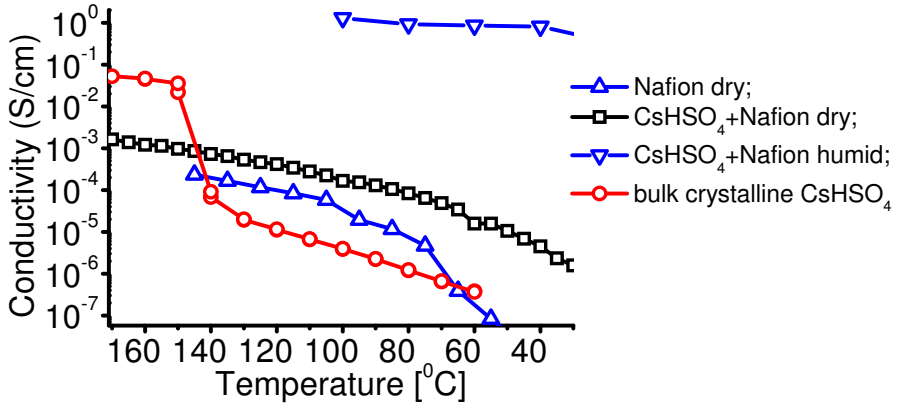

Figure 5.2. Conductivity as a function of temperature for pure Nafion, $CsHSO_4$, and for their composite (in dry and humidified conditions).

Figure 5.3a shows the Nyquist plots of the solid acid Nafion composite membrane at increasing temperatures. Two semi- circles can be observed indicating multiple conductivity contributions, which can be attributed to two mechanisms of proton conduction. The data is analyzed by fitting it to an equivalent electrical circuit model [83, 84]. It appears that only a model containing two resistances in series gives a response which can reproduce the experimental data in the Nyquist plots. Also the variation with temperature can be reproduced (shown in figure 5.3b). A rationale for

a series resistance model may be that at high temperature, where superprotonic conduction through the solid acid is feasible, a low resistance path is present through the solid acid channels. At lower temperatures when the solid acid conductivity reduces apparently a second factor becomes important at positions where the solid acid contact is reduced and the conductivity is bridged possibly through the Nafion walls. It is interesting to note that one of the semicircles disappears at higher temperatures, and reappears as the temperature is reduced again. Apparently the typical relaxation times involved in the slowest process speed up and become similar to the faster process at high temperatures.

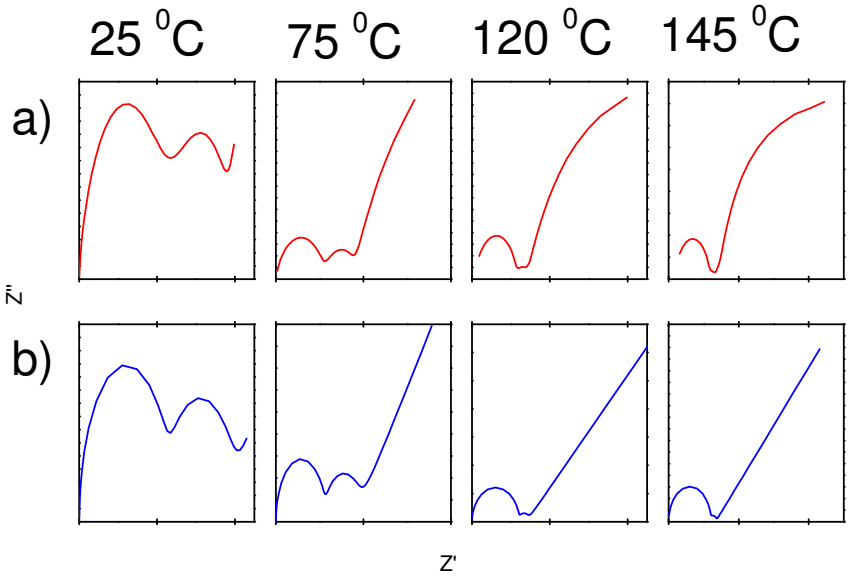

Figure 5.3a. Nyquist plot of $CsHSO_4$ Impregnated Nafion at various temperatures
Figure 5.3b. Modelled response using series circuit at various temperatures.

Figure 5.2 also contains the results of an additional measurement of the composite membrane in high relative humidity. Surprisingly, the conductivity of the humidified composite Nafion, where the channels are filled with solid acid, is of the same order as the conductivity of Nafion with it's channels filled with water. There is still dual conductivity observed, but it is much less pronounced as in the un-humidified measurements. It is likely that mainly the conductivity via the Nafion pore walls is improved since the solid acid can not have dissolved in the low amount of water present.

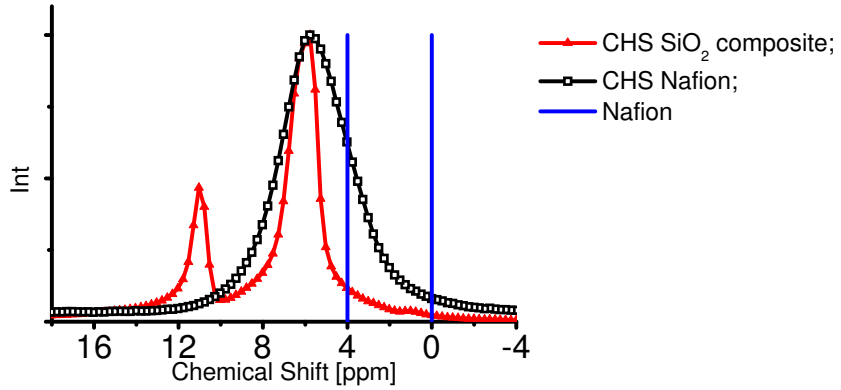

Figure 5.4. Proton NMR spectra of solid acid silica nanocomposite (with spinning speed of 10kHz) and solid acid Nafion composite (static). The vertical lines indicate the position range of protons in water filled nafion membranes.

To obtain more insight in the microcopic composition and mobility ^{1}H NMR measurements were performed on the solid acid-Nafion composite. Due to the nature of the sample, these measurements were done statically. The spectrum is shown in figure 5.4 together with the range of the chemical shifts observed for protons in pure (humidified) Nafion (between the vertical lines) as reported in literature. The latter signal position is dependent on the water uptake [85]. The signal from the solid acid-Nafion composite results from protons belonging to the solid acid because of their high density present in the channels; in fact the signal of fully dried Nafion is negligible because of lack of protons, as is also reported in [85]. In figure 5.4 also a spectrum of a nanostructured $CsHSO_4$ – SiO_2 sample is shown (closed triangles). Note that this spectrum was measured while spinning at 10kHz. As is shown in another publication [24] the peak at 11 ppm for this material comes from crystalline $CsHSO_4$ and the peak around 6 ppm is attributed to mobile protons in or at the surface of the nanoparticles, or in an amorphous fraction of the solid acid. In view of the highly mobile nature of these protons they will also be exchanging between those different positions leading to some averaging of the signals. The resulting peak position from the solid acid-Nafion composite resembles the one of this amorphous solid acid. The shift towards higher ppm values than in pure Nafion can be explained on the basis of the higher acidity of the system when water is replaced by the solid acid; higher acidity leading to higher chemical shift values. There is a slight shoulder in the solid acid - Nafion composite peak, suggesting a small contribution closer to the normal Nafion peak range.
Analysis of the T_1 relaxation times shows values in the range of miliseconds, in contrast to bulk crystaline $CsHSO_4$ with T_1 times of roughly 40 seconds [24, 59, 65]. This clearly illustrates the high mobility of the protons in the solid acid-Nafion composite. The T_1 values are similar to the T_1 times of the 6ppm peak of the SiO_2-

solid acid composite, see table 1. The solid acid in the SiO_2 nanocomposite samples are under influence of strong space charge effects (similar to TiO_2 nano composites [23, 24]), leading to relocation of proton densities towards the less acidic SiO_2 component. Considering the similarities of the T_1 values, and chemical shift ranges, we may expect that a similar relocation of protons occurs where protons from the solid acid spend part of their time on the less acidic $–[O\text{-}CF_2\text{-}CFCH_3]_n\text{-}O\text{-}CF_2CF_2SO_3H$ side branches of Nafion, reducing the average chemical shift to around 6 ppm. E.g. the O in the side chains may provide sites on which H^+ can spend some time.

	Peak	$T_{1\text{-}1}$ [ms]	Frac	$T_{1\text{-}2}$ [ms]	Frac
Solid acid-SiO_2 composite	11 ppm	500	0.68	60	0.32
	6 ppm	50	0.74	3.1	0.26
Solid acid-Nafion composite		30	0.65	3.1	0.35

Table 1. T_1 times comparison at 30 °C. The nanostructured solid acid T_1 times for the peaks at 11 and 6 ppm compared with the solid acid Nafion composite T_1 timese.

5.4. Conclusions

It is shown that the conductivity of the solid acid-Nafion composite at low T in humid environment is similar to pure Nafion although the pores are now filled with solid acid. The conduction mechanism shows two processes likely through the solid acid, and along the Nafion internal surface. In addition at high temperature the incorporated solid acid leads to higher conductivity than dry Nafion. Major advantages of this membrane are its straightforward synthesis and its operation with sufficient conductivity above the boiling point of water.

Chapter 6.

Influence on solid acid Cesium Dihydrogen Phosphate

This chapter is based on the submitted paper:
Particle dependent impact of nanostructuring on ionic mobility in proton conducting solid acids

Wing K. Chan, David I. van der Stok, Ernst R.H. van Eck, Arno P.M. Kentgens, Fokko M. Mulder

Abstract

Nanostructured solid acids are interesting candidates for intermediate temperature fuel cell electrolyte materials. The effect of nanostructuring on the conductivity can be explained by the presence of space charges, which has been shown previously for $CsHSO_4$ composites. This work extends the research towards the less acidic solid acid, cesium dihydrogen phosphate CsH_2PO_4. Nanocomposites with different nanoparticles (TiO_2, SiO_2) in various sizes and different solid acids ($CsHSO_4$, CsH_2PO_4) were investigated using Quasi Elastic Neutron Scattering and Nuclear Magnetic Resonance spectroscopy. Acidity is found to be indicative for the size of space charge effects occurring. SiO_2 is a better proton acceptor than TiO_2 and $CsHSO_4$ is a better proton donor than CsH_2PO_4. The space charge effect manifests itself in the occurance of vacancies and mobile protons. The amount of mobile protons is the key factor in the improved conductivity. Using the acidity combined with calculations [23], it can be understood that large space charge effects are present in CsH_2PO_4 : SiO_2 and $CsHSO_4$: SiO_2 or TiO_2, while effects are much smaller in CsH_2PO_4 : TiO_2.

6.1. Introduction

With the threat of an energy crisis and environmental issues, the change to an alternative energy source and carrier is inevitable. Within this context, the shift to pure hydrogen from sustainable sources seems almost natural. Fuel cells play an important role in the back conversion to electricity. Where sustainable hydrogen production and storage still seem in their infancy [86], the fuel cells have basically outgrown this phase and rapid increase of the use of fuel cells can be noticed [57]. This does not only apply to the traditional stationary power backup, but also increasingly in automotive and smaller scale applications this trend is perceivable. Advancement is not limited to implementation, since technological advances of the fuel cell are also still rapidly evolving. Current generation fuel cells for automotive and smaller applications still run on conventional polymeric proton exchange membranes based on migration of hydronium ions. However, many water free candidates have been considered for next generation fuel cells [34, 87], preferably operating at intermediate temperatures (373 K -573 K). Intermediate temperatures eliminate the need for humidification and complex water management systems. Additionally this implies enhanced catalysis rates and higher tolerance to catalyst poisoning. Furthermore, easier waste heat recovery and the profitable reuse of this energy for e.g. preheating the fuel or liberating the H_2 from a storage material, improve the overall efficiency.

Solid acids are a class of material that has caught attention due to their high proton conductivity (>10^{-2} S/cm) above their superprotonic phase transition at intermediate temperatures. They are acids in solid crystalline form and generally can be represented with the chemical formula: $M_aH_b(XO_4)_c$, where M is a mono- or divalent cation (e.g. Rb, Cs), XO_4 is a tetrahedral oxy-anion (e.g. SO_4, SeO_4, PO_4) and a, b, c, are integers. At low temperatures they are not different from 'normal' salts, however at a certain (intermediate) temperature; these salts undergo a phase transition to a more disordered structure in which the conductivity is increased by orders of magnitudes. This is explained by the fact that at low temperatures, the XO_4 tetrahedral is fixed at its position by stiff hydrogen bonds, but at elevated temperatures, this group is allowed to rotate almost freely as a result of the change in structure [88]. Apart from the rotation of the tetrahedrals the protons also hop from 1 tetrahedral to the next, inducing proton diffusion in the material. Haile et. al. has shown the feasibility of a fuel cell based on the solid acid $CsHSO_4$, which showed very promising performance [7]. In recent years, research has been performed on another solid acid material CsH_2PO_4 [89, 90], which is considered to possess even greater potential due to its higher phase transition temperature and the presence of 2 hydrogen atoms in the structure, with the definitive confirmation by Otomo et al showing a working fuel cell based on CsH_2PO_4 [9]. This fuel cell was operational

between 503 K and 573 K, however not at lower temperatures, which unveils the poor low temperature conductivity of these systems. A solution for this problem was found in the form of nanostructuring [26, 55, 91]. Mixing these solid acids with nanoparticles can result in largely improved conductivity, especially in the temperature range below the superprotonic phase transition.

One of the critical points that will be a deciding factor for the success of solid acids for fuel cell application is the thermal stability. Some solid acids possess inferior stability compared to polymer electrolyte materials and specifically CsH_2PO_4 is subject to decomposition already at temperatures below its superprotonic phase transition [10]. This decomposition reaction is as follows:

$$nCsH_2PO_4 \Leftrightarrow Cs_nH_2P_nO_{3n+1} + (n-1)H_2O$$

With the most common decomposition product n=2 leading to cesium hydrogen pyrophosphate ($Cs_2H_2P_2O_7$), also referred to as simply pyrophosphate. This dehydration of CsH_2PO_4 can be partially suppressed by humidifying the atmosphere [11]. This would however require humidification systems.

In previous work, the microscopic effects of nanostructuring on $CsHSO_4$ have been studied [24]. The huge increase in conductivity was attributed to the fact that a huge fraction of protons becomes highly mobile in the low temperature phase upon nanostructuring with TiO_2 or SiO_2 particles as a result of space charge effects. Space charge occurs at interfaces between the solid acid and these ionic conductors [14, 20, 92-95]. Due to the acidic nature of the solid acid, it is energetically favourable for an H^+ to relocate in the proton accepting TiO_2 or SiO_2. However, due to the charge of the H^+ and the e^- left behind, an electric field builds up that at a certain stage stops the further build up of charge. Then the space charge layers have formed in the conducting matrix and nanoparticles. In the nanometer range, interfaces are that closely spaced that the space charge layers partially overlap. The impact of the interfaces becomes increasingly significant until it dominates the whole material's properties such as the local ionic densities and conductivities [33].

In this work we investigate the effects of nanostructuring using two different types of nanoparticles TiO_2 and SiO_2, combined with two types of solid acid proton conductors $CsHSO_4$ and CsH_2PO_4, in order to extend and generalize the required space charge model for different types of solid acids and proton acceptors. To study the microscopic effects Quasi Elastic Neutron Scattering (QENS), Nuclear Magnetic Resonance (NMR) spectroscopy and X-ray diffraction (XRD) spectroscopy have been applied. The conductivity was measured with Impedance Spectroscopy. A ratio of 1 mol solid acid to two moles of nanoparticles was chosen. In this way one can anticipate that when the nanoparticles form a closed packed set of spheres the solid acid can fill the space between the spherical particles.

6.2. Experimental

Bulk CsH_2PO_4 and bulk $CsHSO_4$ were prepared as described in literature [69], where a Cs_2CO_3 solution and H_3PO_4 or H_2SO_4 were mixed in stoichiometric quantities, respectively. The CsH_2PO_4 and $CsHSO_4$ were recrystallized and dried thoroughly afterwards, in order to make weighing of the solid acid as accurate as possible. X-ray diffraction showed the low temperature phase of CsH_2PO_4 and $CsHSO_4$. Nanoparticles TiO_2 (24nm, 40nm) or SiO_2 (7nm, 40nm) were added afterwards into an aqueous solution in the molar ratios of 1 mol solid acid versus 2 mol nanoparticle. The samples were dried carefully again afterwards. To avoid confusion, the samples will be referred to in the following format: nanoparticle type, size and solid acid type, e.g. TiO_2 24nm phosphate is the nanocomposite consisting of 24 nm TiO_2 particles and CsH_2PO_4. The QENS experiments were performed on IN5 at the High flux reactor of the Institute Max von Laue-Paul Langevin (ILL), with an incident wavelength of 11.5 Å, a resolution function with a full width at half maximum of ~ 6 μeV and covering a Q range of 0.2 – 0.9 $Å^{-1}$. Air tight Al sample containers were used. NMR measurements were performed at the solid-state NMR facility for advanced materials science, Radboud University in Nijmegen, The Netherlands. Using a 400 MHz spectrometer with a static magnetic field strength of 9.4 T, the ^1H Larmor frequency was 399.95 MHz. The measurements were performed at room temperature. A 3.2mm airtight zirconia rotor was used to measure the Magic Angle Spinning (MAS) ^1H spectra and spin-lattice relaxation times. The spinning frequencies were around 10 kHz. The X-ray powder diffraction measurements were performed on a PANanalytical X'pert PRO diffractometer with the optional TTK450 closed oven installed. Spectra were taken at temperatures ranging from 298 K to 523 K using a Cu Kα source. For the Impedance measurements, the bulk and nanocomposite samples were pressed at roughly 2 ton/cm^2 to form dense pellets with 13mm diameter and thicknesses of around 1 mm. To improve electrical contact a thin gold layer was sputtered on both sides of the pellets. The conductivity measurements were performed by means of ac impedance spectroscopy using a Hewlett Packard impedance analyzer in the frequency range from 3 MHz to 1 Hz. The samples were heated from 303 K to 523 K, in steps of 10 or 30 degrees, and cooled down again to 303 K.

6.3. Results and Discussion

The freshly synthesized samples were characterized with X-ray diffraction. The initial XRD spectra showed a clean phase of Cesium dihydrogen phosphate. However after one temperature cycle, the spectra started showing additional peaks.

After detailed analysis the pollutant phase was identified as mainly consisting of the decomposition product pyrophosphate. The decomposition appeared to be larger in the nanocomposite samples. Figure 6.1 compares the phase fraction of pyrophosphate in bulk and TiO_2 24nm phosphate sample. On the x-axis the temperature during the cycles are shown. The nanocomposite during the first heating run is much more subdue to decomposition, forming almost twice as much pyrophosphate. This phase decreases slightly during the cooling run, confirming the partial reversibility of the pyrophosphate formation reaction in the presence of water. The difference in decomposition rate becomes much less profound during the next few cycles. The reason for the relative stabilization might be attributed to the formation of a pyrophosphate shell around the sample. The shell could be observed by eye due to a difference in color and a more solid structure. This might retain the moisture somewhat, which would stabilize the samples. Still, after 3 cycles the phase fraction of pyrophosphate reaches over 0.4, which will greatly influence the conductivity.

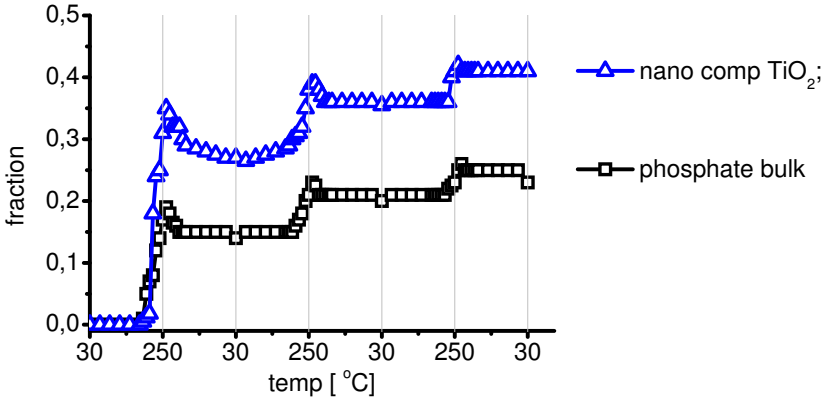

Figure 6.1. Pyrophosphate formation of bulk phosphate and TiO_2 24nm phosphate during temperature cycles from 30°C-250°C, 250°C-30°C, etc. Note that decomposition starts at around 200°C.

The increased decomposition in the nanomaterials may be related to a higher mobility in the nanostructured sample. However, increased proton mobility is the goal inherent to improving conductivity in these samples.
During the measurements great care was taken to minimize the decomposition of the samples. Measuring at temperatures below the superprotonic phase transition temperature was therefore crucial. Careful analysis of the XRD spectra showed a phasefraction of TiO_2 that was consistently larger than the theoretical values. However, Flame Atomic Emission Spectroscopy (FAES) measurements combined with Inductively Coupled Plasma Optical Emission Spectroscopy (ICP-OES) measurements showed the expected theoretical ratios. The explanation here lies in the fact that part of the solid acid becomes X-ray amorphous, which made the

fraction of TiO_2 appear relatively larger. The aforementioned destabilization of the crystalline phosphate matrix due to space charges, appears to result in amorphization of the solid acid. The presence of an amorphous phase was taken into account during the synthesis, measurements and analysis of the samples. The solid acid $CsHSO_4$ has been characterized and analyzed in a previous publication [24]. While it does possess an amorphous phase, decomposition did not occur.

The impact of nanostructuring on the solid acids is also studied with impedance spectroscopy measurements. Figure 6.2 shows the conductivity of TiO_2 24nm phosphate and sulfate, SiO_2 7nm phosphate and sulfate and the bulk crystalline samples of CsH_2PO_4 and $CsHSO_4$ as function of temperature. The conductivity pattern of the phosphates and the sulfates are very similar although shifted in temperature. The bulk samples show a superprotonic phase transistion, where the conductivity increases with orders of magnitude. At high temperature the nanocomposite samples possess inferior conductivity compared to the bulk crystalline phases. This suggests that the nanostructuring inhibits the conductivity at high temperatures. Explanations will be the smaller amount of solid acid present due to increased pyrophosphate formation and the addition of the high concentration of filler particles. The conduction at temperatures below the superprotonic phase transition however is much improved. Though the increase is relatively low compared to the superprotonic bulk phase, it is still a few orders of magnitude higher compared to the low temperature bulk phase. It should be noted that here the composition with large amounts of nanoparticles was chosen to study the effect on the solid acid, and not to optimise the conductivity. Furthermore it is interesting to note that the effect on the conductivity for the SiO_2 and TiO_2 is similar for $CsHSO_4$, but quite different for CsH_2PO_4. There the TiO_2 has a much reduced effect at temperatures below the transition temperature.

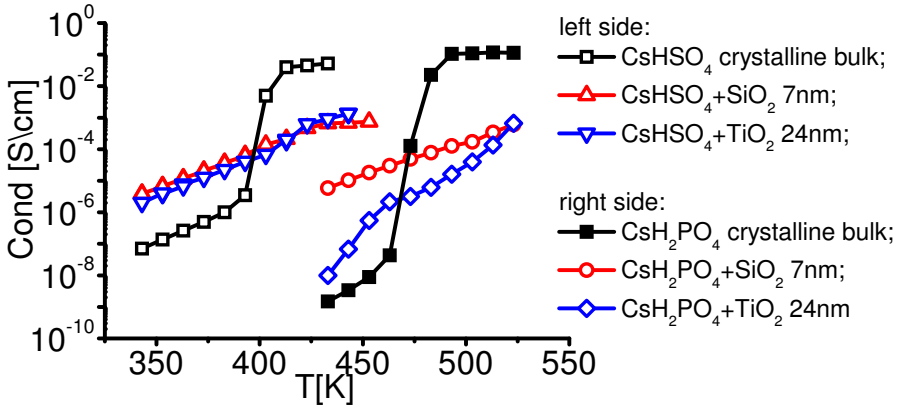

Figure 6.2. Conductivity measurements of various sulfate and phosphate nanocomposite samples compared with bulk crystalline samples.

In an attempt to get a better understanding about the influences of nanostructuring on the intrinsic proton mobility, QENS measurements were performed. Special attention is paid to the temperatures below 200°C, where decomposition to pyrophosphate is absent. This technique directly probes the mobility of the protons in the sample and also yields timescales and lengthscales of the mobility through the energy and momentum transfer measurements. The width and intensity of the broadening is a measure for proton mobility. QENS previously has been used to investigate the bulk crystalline $CsHSO_4$ [64] and nano structured $CsHSO_4$ [24]. The protons in the $CsHSO_4$ undergo a two step diffusion process, which involves a change in orientation of the SO_4 group and a transfer between SO_4 groups. This is modelled using a convolution of two Lorentzian contributions and a function representing the resolution function. The narrow Lorentzians show Q^2 dependence down to small Q values (typically < $0.2Å^{-1}$, where Q is the scattering vector), indicating translational diffusion of the protons over lengthscales of many Ångströms. The broad Lorentzians were having a constant width as a function of Q, indicating a vibrational motion, attributed to the reorientation of the SO_4 groups. The presence of two protons per oxy-anion group in the phosphate will lead to a slightly more complex diffusion process. However, it is believed that the QENS spectra of CsH_2PO_4 will have similar features.

Figure 6.3a illustrates the broadening at the feet of the QENS spectra, which is a measure for proton mobility. The spectra plotted here are the resolution function, the bulk crystalline CsH_2PO_4, TiO_2 24nm phosphate at 350K and 450K and SiO_2 7nm phosphate at 350K and 450K. Note that all temperatures are below the superprotonic phase transition and in 6.3a both below the decomposition temperature. The bulk crystalline CsH_2PO_4 spectrum, as expected shows almost no broadening at the foot compared to the resolution function, i.e. no proton mobility is detected on a nanosecond timescale. The TiO_2 24nm phosphate at 350K shows a broadening, but this is very small compared to the other spectra, with the SiO_2 7nm phosphate at 450K showing most broadening. Comparing the mobility from QENS with the conductivity results above, one observes the same trend: more mobility for the SiO_2 than for the TiO_2 samples and both more than the bulk (at low temperatures). Careful fitting resulted in the narrow Lorentzian function showing Q^2 dependence. The broad Lorentzian functions with a width in the range of meVs however, have too low intensity to determine the Q dependence. The fits for the narrow Lorentzian functions are shown in figure 6.3b and 6.3c. Figure 6.3b shows the width of the narrow Lorentzians as function of the temperature and figure 6.3c shows the intensities, which represents the fraction of mobile protons in the samples.

As can be observed from figure 6.3b, the linewidth related to the mobility of the protons in each individual sample measured, is quite constant over the whole temperature range. The mobility in TiO_2 24nm phosphate is surprisingly higher compared to the other nanocomposite samples. However, the intensity is relatively

small. For all samples the fraction of mobile protons increases with increasing temperature. The slopes in the sulfate samples seem steeper, indicating stronger temperature dependence. When nearing the superprotonic phase transition temperature of the phosphate samples going above 473K, a slight decrease in mobility as well as mobile fraction is observed. This is due to water vapor pressure buildup in the sample holder, due to decomposition of the phosphates resulting in a loss of signal in this energy window.

Note the difference between the mobile proton fractions of the TiO_2 24nm nanosamples of $CsHSO_4$ and CsH_2PO_4. While it is higher than the SiO_2 nanosamples for the TiO_2 24nm sulfate, the mobile fraction of the TiO_2 24nm phosphate is much lower. In terms of space charge, this will mean that fewer protons are being drawn by the TiO_2 nanoparticles from the phosphate. This results in fewer vacant positions in the phosphate and therefore fewer protons are able to move. As for the conductivity, it seems that the fraction of mobile protons plays a much bigger role in improving the conductivity than the mobility of the protons itself. The mobility of the protons in TiO_2 24nm phosphate is much higher compared to the other samples (figure 6.3c), however the conductivity is lowest. For the TiO_2 24nm sulphate the proton mobility is lower compared to SiO_2 7nm sulphate, however it possesses a higher mobile fraction, resulting in a similar conductivity as the other two SiO_2 nanosamples.

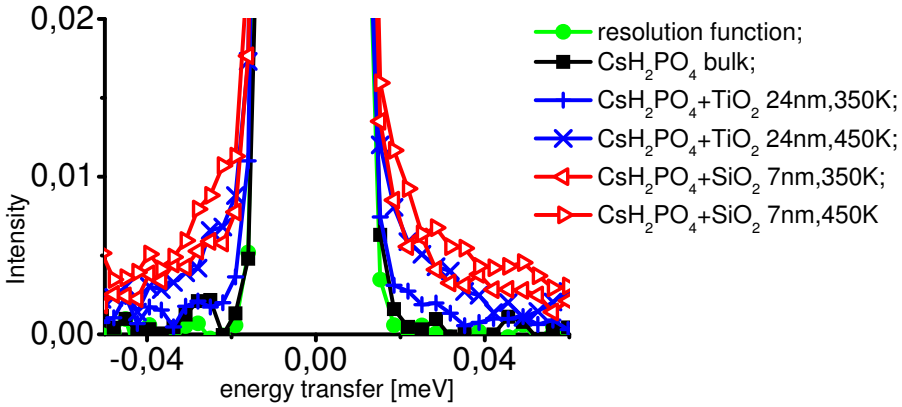

Figure 6.3a. QENS spectra at Q = 1 $Å^{-1}$ of resolution function, bulk phosphate, TiO_2 24nm phosphate at 350 K, TiO_2 24nm phosphate at 450 K, SiO_2 7nm phosphate at 350 K and TiO_2 7nm phosphate at 450 K.

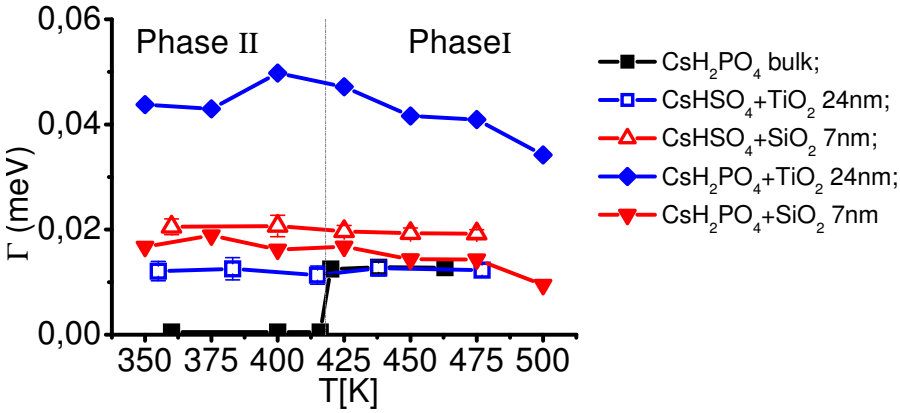

Figure 6.3b. Results of QENS fits. Linewidth of mobile protons in the sulphate and phosphate samples.

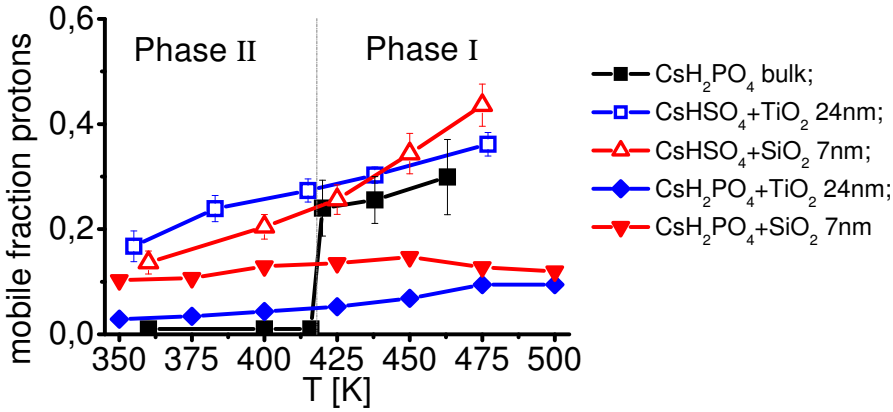

Figure 6.3c. Results of QENS fits. Fraction of mobile protons in sulfate and phosphate samples.

NMR is a complementary technique to QENS and probes via the T_1 relaxation similar timescales of motion to within an order of magnitude as QENS. The NMR spectra were taken around room temperature to obtain more insight in the large difference in conductivity. Bulk phosphate possesses two peaks in MAS NMR; one at 14.33 ppm and one at 10.67 ppm. These are attributed to the two proton sites present in CsH_2PO_4 (and will be referred to as 'solid acid peaks'). Figure 6.4 shows the proton spectra of the phosphate and sulfate nanocomposite samples, normalized at 1 for the peak with highest intensity. TiO_2 40nm phosphate and SiO_2 40nm sulfate are also measured to make comparison possible. The nanosamples show the expected peaks at 14.33 ppm and 10.67 ppm, but also possess an additional peak at lower chemical shift (from here on referred to as 'nanopeak'). The same is true for

the sulfate samples. The bulk sulfate possesses a single peak at 11.04 ppm, attributed to the single proton site in $CsHSO_4$ [24]. The nanocomposite sulfate samples also show an additional peak at lower chemical shift, as seen in figure 6.4b. The positions of the solid acid peaks are not influenced by the nanostructuring; they are nearly identical for all samples. The position of the extra nanopeak however, depends on the type of solid acid and the type of nanoparticle used.

In general a large chemical shift indicates strong deshielding of the protons. In this case it is caused by the electronegativity of the oxy-anion groups. The lower chemical shifts in the nanopeaks of the composites therefore indicate that these protons are in a less acidic environment. Comparing the nanopeak positions, the TiO_2 nanopeaks generally possess a higher chemical shift with respect to the SiO_2 nanopeaks. The TiO_2 sulfate peaks are over 0.5 ppm higher than the SiO_2 sulfate peaks and the TiO_2 phosphates are positioned more than 1 ppm from the SiO_2 phosphates. In terms of acidity, it can be said that the sulfates are most acidic, e.g. they are better proton donors than the phosphates. Likewise, this makes SiO_2 the better proton acceptors compared to TiO_2. Note that donating and accepting protons is necessary to create space charge layers and that besides the acidity, the number of active sites at the surface plays a role in this effect.

The intensities of these nanopeaks seem to depend strongly on the particle size. The samples mixed with 40nm particles roughly show the same intensities for the nanopeaks, while the samples with 7nm particles show much larger nanopeak intensities than the samples with 24nm particles. Note that the nanopeak intensity is strongly related to the presence of the amorphous phase, which in its turn is dependent on sample preparation and history [9, 29]. However, under similar synthesis conditions one would assume that the nanopeak intensity is also strongly dependent on the nanoparticle size.

Taking into account the impedance measurements, the following would explain the low conductivity of the TiO_2 24nm phosphate. Based on acidity, it turns out that the worst combination (in our case) would be phosphate as proton donor and the TiO_2 as proton acceptor. The difference between acidity appears to be too low to generate a large (space charge) effect.

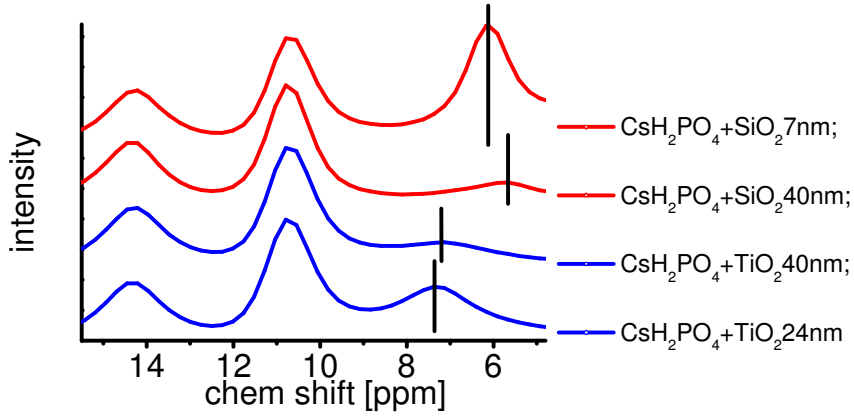

Figure 6.4a. ^{1}H NMR spectra of Cesium dihydrogen phosphate nanocomposite samples.

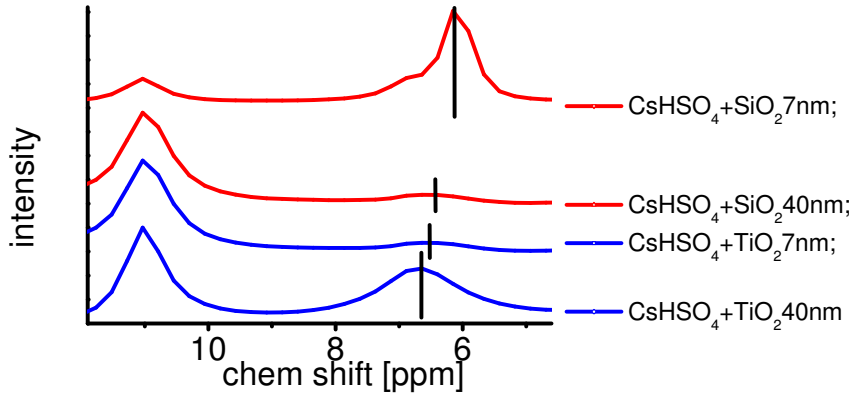

Figure 6.4b. ^{1}H NMR spectra of Cesium hydrogen sulfate nanocomposite samples.

T_1 saturation recovery experiments have been performed. T_1 relaxation time analysis of the individual peaks resulted in table 1 and table 2. Table 1 shows the T_1 times and the respective fractions for the three peaks of the phosphate samples, while Table 2 shows these results for the sulfate samples. The bulk crystalline phosphate showed a long T_1 time of roughly 40 seconds, but surprisingly also a short component in the order of 1 second. Analysis of the nanocomposite sample peaks gave best fits with two T_1 components for each resonance line. A longer component referred to as $T_{1\text{-}1}$ and a shorter one, $T_{1\text{-}2}$. The influence of the nanostructuring is significant, as not only the nanopeaks show reduced and short T_1 times, but also the solid acid peak T_1 times are reduced clearly compared to the bulk phosphate. This decrease is very prominent with the long components. A clear trend is observable as

TiO_2 leads to T_1 times roughly 4 times shorter compared to the bulk phosphate T_{1-1} and SiO_2 results in 10 times shorter T_{1-1} times. As no long component (around 40 seconds) is present in the nanocomposites, this suggests that all of the solid acid present in the nanosamples is influenced by the nanostructuring.

For a physical meaning of these components, one might suggest that the long T_{1-1} time represents the protons in the crystalline solid acid, which are becoming more mobile due to the vacancies created by the space charge. The larger the space charge effect, the more this long component is influenced. The fitted T_1 times of the nanopeaks were 10 to 100 times shorter than the T_1 times of the bulk solid acid peaks. These components are attributed to protons in the amorphous phase and protons in or at the surface of the added TiO_2 and SiO_2 nanoparticles [24]. The behavior of the sulfate samples is similar to the phosphate samples with respect to T_1 times. The long component T_{1-1} decreases significantly. However, SiO_2 7nm sulfate seems to undergo even stronger reduced T_1 times and it shows the strongest nano peak.

	Peak 1 (14.3 ppm)				Peak 2 (10.7 ppm)				Peak 3 (nanopeak)			
Sample	T_{1-1} [sec]	Frac T_{1-1}	T_{1-2} [sec]	Frac T_{1-2}	T_{1-1} [sec]	Frac T_{1-1}	T_{1-2} [sec]	Frac T_{1-2}	T_{1-1} [sec]	Frac T_{1-1}	T_{1-2} [sec]	Frac T_{1-2}
Bulk	41	0.73	1.1	0.27	35	0.74	0.96	0.26	--	--	--	--
TiO_2 40nm	11	0.37	0.58	0.63	35	0.53	0.56	0.47	2.4	0.16	0.17	0.84
TiO_2 24nm	8.0	0.59	0.92	0.43	15	0.55	1.0	0.45	0.44	0.89	0.07	0.11
SiO_2 40nm	3.7	0.78	0.57	0.22	5.8	0.69	0.63	0.31	0.42	0.64	0.08	0.36
SiO_2 7nm	1.9	0.66	0.67	0.34	2.0	0.69	0.53	0.31	0.66	0.57	0.18	0.43

Table 1. Proton T_1 times of Phosphate samples.

	Peak 1 (11.0 ppm)				Peak 2 (nanopeak)			
Sample	T_{1-1} [sec]	Frac T_{1-1}	T_{1-2} [sec]	Frac T_{1-2}	T_{1-1} [sec]	Frac T_{1-1}	T_{1-2} [sec]	Frac T_{1-2}
Bulk	41	0.89	0.92	0.11	--	--	--	--
TiO_2 40nm	10	0.31	1.0	0.69	1.7	0.65	0.14	0.35
TiO_2 24nm	10	0.47	0.62	0.53	1.0	0.43	0.20	0.57
SiO_2 40nm	4.7	0.68	0.26	0.32	1.3	0.61	0.0062	0.39
SiO_2 7nm	0.51	0.68	0.057	0.32	0.048	0.74	0.0031	0.26

Table 2. Proton T_1 times of Sulfate samples.

T_1 times analysis of the nanocomposites seems to be in agreement with what was concluded from the chemical shift analysis. SiO_2 nanoparticles result in samples with shortest T_1 times. The T_1 times for the nanocomposite sulfates and phosphates appear to be of similar order, which is in line with the finding from the QENS analysis that the timescale of the induced dynamics is similar for these materials.

6.4. Conclusion

The large improvement in conductivity observed in nanocomposites of CsH_2PO_4 and $CsHSO_4$ with TiO_2 or SiO_2 at temperatures below the superprotonic phase transition is mainly due to the increased amount of protons moving. The actual mobility of the mobile protons seems to play a less significant role. All of the solid acid phase in the composite is influenced by nanostructuring, as the T_1 times are all reduced. Using the acidity, SiO_2 is a better proton acceptor than TiO_2 and hydrogen sulfate a better proton donor than hydrogen phosphate. Acidity is a useful way to predict the extent of the space charge effect that lead to the transfer of H^+ to the nanoparticles and the creation of vacancies. This understanding, combined with calculations as described in [23] will facilitate the search for the optimal combination for electrolyte membrane material in fuel cell applications.

Acknowledgement
NWO is thanked for their financial support of the solid-state NMR facility for advanced materials science at the Radboud University in Nijmegen. J. van Os, G. Janssen and H. Janssen are acknowledged for technical support with the NMR measurements. This article is the result of joint research in the Delft Research Centre for Sustainable Energy and the 3TU. Centre for Sustainable Energy Technologies. The Department of Nanostructured materials, Delft Chem Tech at the Delft University of Technology is thanked for making the Impedance Spectroscopy measurements possible. The Institute Laue-Langevin is acknowledged for QENS measurement time on IN5.

Bibliography

[1] R.Heinberg, *The Party's over*, New Society Publishers, **2005**.
[2] www1.eere.energy.gov, **2010**.
[3] www.ballard.com, **2010**.
[4] B.C.H.Steele, *Journal of Materials Science* **2001**, *36*, 1053.
[5] R.Anahara, S.Yokokawa, M.Sakurai, *Proceedings of the Ieee* **1993**, *81*, 399.
[6] A.V.Belushkin, M.A.Adams, S.Hull, L.A.Shuvalov, *Solid State Ionics* **1995**, *77*, 91.
[7] S.M.Haile, D.A.Boysen, C.R.I.Chisholm, R.B.Merle, *Nature* **2001**, *410*, 910.
[8] K.Yamada, T.Sagara, Y.Yamane, H.Ohki, T.Okuda, *Solid State Ionics* **2004**, *175*, 557.
[9] J.Otomo, T.Tamaki, S.Nishida, S.Q.Wang, M.Ogura, T.Kobayashi, C.J.Wen, H.Nagamoto, H.Takahashi, *Journal of Applied Electrochemistry* **2005**, *35*, 865.
[10] Y.K.Taninouchi, T.Uda, Y.Awakura, A.Ikeda, S.M.Haile, *Journal of Materials Chemistry* **2007**, *17*, 3182.
[11] D.A.Boysen, *Thesis* **2004**.
[12] V.G.Ponomareva, G.V.Lavrova, *Solid State Ionics* **2001**, *145*, 197.
[13] J.Otomo, H.Shigeoka, H.Nagamoto, H.Takahashi, *Journal of Physics and Chemistry of Solids* **2005**, *66*, 21.
[14] J.Maier, *Solid State Ionics* **1987**, *23*, 59.
[15] J.Maier, *Solid State Ionics* **1994**, *70*, 43.
[16] J.Maier, *Journal of the European Ceramic Society* **1999**, *19*, 675.
[17] J.Maier, *Electrochemistry* **2000**, *68*, 395.
[18] J.Maier, *Solid State Ionics* **2003**, *157*, 327.
[19] J.Maier, *Nature Materials* **2005**, *4*, 805.
[20] J.Maier, *Progress in Solid State Chemistry* **1995**, *23*, 171.
[21] A.Mari Svensson, S.M°ller-Holst, R.Gl÷ckner, O.Maurstad, *Energy* **2007**, *32*, 437.
[22] J.R.Macdonald, *Impedance Spectroscopy*, John Wiley & Sons, New Jersey, **2005**.
[23] L.A.Haverkate, W.K.Chan, F.M.Mulder, *Adv. Funct. Mater.* **2010**, *20*, 4018.
[24] W.K.Chan, L.A.Haverkate, W.J.H.Borghols, M.Wagemaker, S.J.Picken, E.R.H.van Eck, A.P.M.Kentgens, M.R.Johnson, G.J.Kearley, F.M.Mulder, *Adv. Funct. Mater.* **2011**, *21*, 1364.
[25] V.G.Ponomareva, G.V.Lavrova, L.G.Simonova, *Solid State Ionics* **1999**, *119*, 295.
[26] V.G.Ponomareva, G.V.Lavrova, *Solid State Ionics* **1998**, *106*, 137.
[27] V.G.Ponomareva, N.F.Uvarov, G.V.Lavrova, E.F.Hairetdinov, *Solid State Ionics* **1996**, *90*, 161.

[28] S.Q.Wang, J.Otomo, M.Ogura, C.Wen, H.Nagamoto, H.Takahashi, *Solid State Ionics* **2005**, *176*, 755.
[29] J.Otomo, N.Minagawa, C.J.Wen, K.Eguchi, H.Takahashi, *Solid State Ionics* **2003**, *156*, 357.
[30] V.G.Ponomareva, G.V.Lavrova, L.G.Simonova, *Solid State Ionics* **1999**, *118*, 317.
[31] A.Sacca, A.Carbone, E.Passalacqua, A.D'Epifanio, S.Licoccia, E.Traversa, E.Sala, F.Traini, R.Ornelas, *Journal of Power Sources* **2005**, *152*, 16.
[32] H.Ekstrom, B.Wickman, M.Gustavsson, P.Hanarp, L.Eurenius, E.Olsson, G.Lindbergh, *Electrochimica Acta* **2007**, *52*, 4239.
[33] N.Sata, K.Eberman, K.Eberl, J.Maier, *Nature* **2000**, *408*, 946.
[34] M.L.Di Vona, Z.Ahmed, S.Bellitto, A.Lenci, E.Traversa, S.Licoccia, *Journal of Membrane Science* **2007**, *296*, 156.
[35] A.C.Larson, R.B.Dreele, *LAUR* **1994**, 86.
[36] V.Favre-Nicolin, R.Cerny, *Journal of Applied Crystallography* **2002**, *35*, 734.
[37] G.Kresse, J.Furthmuller, *Computational Materials Science* **1996**, *6*, 15.
[38] G.Kresse, J.Furthmuller, *Physical Review B* **1996**, *54*, 11169.
[39] G.Kresse, D.Joubert, *Physical Review B* **1999**, *59*, 1758.
[40] M.Wagemaker, G.J.Kearley, A.A.van Well, H.Mutka, F.M.Mulder, *Journal of the American Chemical Society* **2003**, *125*, 840.
[41] H.Sun, S.J.Mumby, J.R.Maple, A.T.Hagler, *Journal of Physical Chemistry* **1995**, *99*, 5873.
[42] "Materials Studio Modeling", Accelrys, **2005**, Ch. 3.2.
[43] K.D.Kreuer, S.J.Paddison, E.Spohr, M.Schuster, *Chemical Reviews* **2004**, *104*, 4637.
[44] A.Venkatnathan, R.Devanathan, M.Dupuis, *Journal of Physical Chemistry B* **2007**, *111*, 7234.
[45] P.J.James, J.A.Elliott, T.J.McMaster, J.M.Newton, A.M.S.Elliott, S.Hanna, M.J.Miles, *Journal of Materials Science* **2000**, *35*, 5111.
[46] C.Bechinger, S.Ferrer, A.Zaban, J.Sprague, B.A.Gregg, *Nature* **1996**, *383*, 608.
[47] M.Wagemaker, A.P.M.Kentgens, F.M.Mulder, *Nature* **2002**, *418*, 397.
[48] M.Wagemaker, A.A.van Well, G.J.Kearley, F.M.Mulder, *Solid State Ionics* **2004**, *175*, 191.
[49] F.de Bruijn, *Green Chemistry* **2005**, *7*, 132.
[50] R.Waser, M.Aono, *Nature Materials* **2007**, *6*, 833.
[51] N.Ohta, K.Takada, L.Q.Zhang, R.Z.Ma, M.Osada, T.Sasaki, *Advanced Materials* **2006**, *18*, 2226-+.
[52] V.V.Zhirnov, R.K.Cavin, *Nature Nanotechnology* **2008**, *3*, 377.
[53] High Level Group, *Nanoelectronics at the center of change* **2004**, *6*, 1.
[54] J.Jamnik, J.Maier, *Physical Chemistry Chemical Physics* **2003**, *5*, 5215.
[55] P.Knauth, *Solid State Ionics* **2006**, *177*, 2495.
[56] A.I.Baranov, *Crystallography Reports* **2003**, *48*, 1012.
[57] H.J.Neef, *Energy* **2009**, *34*, 327.

[58] A.V.Belushkin, M.A.Adams, S.Hull, A.I.Kolesnikov, L.A.Shuvalov, *Physica B* **1995**, *213*, 1034.
[59] S.Hayashi, M.Mizuno, *Solid State Ionics* **2004**, *171*, 289.
[60] C.R.I.Chisholm, R.B.Merle, D.A.Boysen, S.M.Haile, *Chemistry of Materials* **2002**, *14*, 3889.
[61] S.M.Haile, C.R.I.Chisholm, K.Sasaki, D.A.Boysen, T.Uda, *Faraday Discussions* **2007**, *134*, 17.
[62] G.V.Lavrova, M.V.Russkikh, V.G.Ponomareva, N.F.Uvarov, *Russian Journal of Electrochemistry* **2005**, *41*, 485.
[63] A.I.Baranov, L.A.Shuvalov, N.M.Shchagina, *Jetp Letters* **1982**, *36*, 459.
[64] A.V.Belushkin, C.J.Carlile, L.A.Shuvalov, *Journal of Physics-Condensed Matter* **1992**, *4*, 389.
[65] R.Blinc, J.Dolinsek, G.Lahajnar, I.Zupancic, L.A.Shuvalov, A.I.Baranov, *Physica Status Solidi B-Basic Research* **1984**, *123*, K83-K87.
[66] D.Arcon, R.Blinc, J.Dolinsek, L.A.Shuvalov, *Physical Review B* **1997**, *55*, 8961.
[67] J.Maier, *Solid State Ionics* **2002**, *154*, 291.
[68] W.K.Chan, W.J.H.Borghols, F.M.Mulder, *Chemical Communications* **2008**, 6342.
[69] A.V.Belushkin, I.Natkaniec, N.M.Pakida, L.A.Shuvalov, J.Wasicki, *Journal of Physics C-Solid State Physics* **1987**, *20*, 671.
[70] M.Wagemaker, W.J.H.Borghols, F.M.Mulder, *Journal of the American Chemical Society* **2007**, *129*, 4323.
[71] S.Hayashi, M.Mizuno, *Solid State Communications* **2004**, *132*, 443.
[72] Y.Daiko, S.Hayashi, A.Matsuda, *Chemistry of Materials* **2010**, *22*, 3418.
[73] M.N.Kislitsyn, "Materials Chemistry of Superprotonic Solid Acids", California Institute of Technology, **2009**.
[74] K.A.Mauritz, R.B.Moore, *Chemical Reviews* **2004**, *104*, 4535.
[75] A.V.Belushkin, W.I.F.David, R.M.Ibberson, L.A.Shuvalov, *Acta Crystallographica Section B-Structural Science* **1991**, *47*, 161.
[76] C.R.I.Chisholm, Y.H.Jang, S.M.Haile, W.A.Goddard, *Physical Review B* **2005**, *72*.
[77] M.Cappadonia, J.W.Erning, S.M.S.Niaki, U.Stimming, *Solid State Ionics* **1995**, *77*, 65.
[78] H.F.Xu, X.Wang, Z.G.Shao, I.M.Hsing, *Journal of Applied Electrochemistry* **2002**, *32*, 1337.
[79] Y.H.Luan, H.Zhang, Y.M.Zhang, L.Li, H.Li, Y.G.Liu, *Journal of Membrane Science* **2008**, *319*, 91.
[80] A.V.Belushkin, R.M.Ibberson, L.A.Shuvalov, *Journal of Molecular Structure* **1996**, *374*, 161.
[81] C.R.I.Chisholm, S.M.Haile, *Solid State Ionics* **2000**, *136*, 229.
[82] V.G.Ponomareva, E.S.Shutova, A.A.Matvienko, *Inorganic Materials* **2004**, *40*, 721.
[83] P.M.Faia, A.J.Ferreira, C.S.Furtado, *Sensors and Actuators B-Chemical* **2009**, *140*, 128.
[84] J.E.Bauerle, *Journal of Physics and Chemistry of Solids* **1969**, *30*, 2657-&.

[85] J.Kawamura, K.Hattori, T.Hongo, R.Asayama, N.Kuwata, T.Hattori, J.Mizusaki, *Solid State Ionics* **2005**, *176*, 2451.
[86] L.B.Brentner, J.Peccia, J.B.Zimmerman, *Environ Sci Technol* **2010**, *44*, 2243.
[87] Y.Kozawa, S.Suzuki, M.Miyayama, T.Okumiya, E.Traversa, *Solid State Ionics* **2010**, *181*, 348.
[88] A.V.Belushkin, C.J.Carlile, W.I.F.David, R.M.Ibberson, L.A.Shuvalov, W.Zajac, *Physica B* **1991**, *174*, 268.
[89] Y.Yamane, K.Yamada, K.Inoue, *Solid State Ionics* **2008**, *179*, 483.
[90] H.S.Lee, M.E.Tuckerman, *Journal of Physical Chemistry C* **2008**, *112*, 9917.
[91] J.Jamnik, J.Maier, S.Pejovnik, *Solid State Ionics* **1995**, *75*, 51.
[92] J.Maier, *Solid State Ionics* **2000**, *131*, 13.
[93] J.Maier, *Solid State Ionics* **2004**, *175*, 7.
[94] J.Maier, *Faraday Discussions* **2007**, *134*, 51.
[95] J.Maier, *Progress in Solid State Chemistry* **1995**, *23*, 171.

List of publications

- *Direct observation of space charge induced hydrogen ion insertion in nanoscale anatase TiO_2*
  W.K. Chan, W.J.H. Borghols, F.M. Mulder, Chemical Communications, 2008, 6342

- *Direct view on nanoionic proton mobility*
  W.K. Chan, L.A. Haverkate, W.J.H. Borghols, M. Wagemaker, S.J. Picken, E.R.H. van Eck, A.P.M. Kentgens, M.R. Johnson, G.J. Kearley, F.M. Mulder, Advanced Functional Materials, 2011, 21, 1364

- *Large Space-Charge Effects in a Nanostructured Proton Conductor*
  L.A. Haverkate, W.K. Chan, F.M. Mulder, Advanced Functional Materials , 2010, 20, 4018

- *Highly conductive Solid Acid impregnated Nafion composite fuel cell electrolyte membrane*
  W.K. Chan, H.C. Patel, T.J. Dingemans, S.J. Picken, and F.M. Mulder, submitted to Chemical Communications

- *Particle dependent impact of nanostructuring on ionic mobility in proton conducting solid acids*
  W.K. Chan, D.I. van der Stok, E.R.H. van Eck, A.P.M. Kentgens, F.M. Mulder, to be submitted

Summary

The transition to sustainable energy sources is inevitable. If in this scenario hydrogen becomes the primary energy carrier, fuel cells will play a very important role in the conversion of the hydrogen back to electricity. The technology behind the fuel cell however, still has significant room for improvement. Note that our discussion about the fuel cell is with an eventual implementation in the automotive sector in mind. A next step in the improvement of the fuel cell is the realisation of so called intermediate temperature fuel cells. Current polymer electrolyte fuel cells operate below 100 °C due to the inherent limitation of the conduction mechanism of the electrolyte, which is based on the presence of liquid water. Solid acids have been shown to be promising candidates for fuel cell electrolytes as they possess high proton conductivity in the intermediate temperature range, from ambient up to 250 °C. One major problem of the solid acids is the low proton conduction at temperatures below their superprotonic phase transition. This has been solved by nanostructuring these materials, after which the conductivity increases with orders of magnitude. The mechanism responsible for the enhanced conductivity however, is debated in literature and microscopically not much is known about the occurring phenomena. There have been no reports about microscopic experiments or physical explanations in literature.
This thesis presents a multi-technique approach, using various techniques operating at the molecular or microscopic scale in order to get more insight into this matter. The solid acids $CsHSO_4$ and CsH_2PO_4 with nanoparticulate TiO_2 or SiO_2 have been studied. The solid acids were in protonated and deuterated form. The nanoparticulate TiO_2 consisted of the sizes 40 nm, 24 nm, 15 nm down to 7 nm and the SiO_2 varied in size between 40 nm and 7 nm. For structural information, X-ray diffraction (XRD) and neutron diffraction (ND) were applied. For information on the dynamics, Quasi Elastic Neutron Diffraction (QENS) and Nuclear Magnetic Resonance (NMR) spectroscopy were used next to dielectric impedance spectroscopy. Ab-initio calculations using the VASP package were performed for insight on both structure and dynamics. These techniques were chosen for their sensitivity and complementary nature as local probe to different length and time scales.

Deuterium intercalation in TiO_2 anatase nanoparticles
Spontaneous hydrogen density in nanoparticles were studied through neutron diffraction on TiO_2 anatase nanoparticles of sizes 24 and 7 nm immersed in liquid D_2SO_4. Liquid D_2SO_4 was used in order to reduce background signal as liquids do

not show complex diffraction patterns and deuterium possesses a relatively small incoherent cross section compared to hydrogen.
The presence of deuterons in TiO_2 has been observed at the position [0.00, 0.75, 0.43], which corresponds with a split position of the deuterons inside the oxygen octahedron. Modeling using VASP showed a similar position. The occupancy extracted from Rietveld refinement translates to deuteron intercalation of 9% and 17% for the 24nm and 7nm particles respectively. Lithium intercalation in TiO_2 is accompanied by a color change; the TiO_2 turns blue due to the presence of electrons from the lithium ions. With the acid no color change was observed, indicating that there are no electrons accompanying the deuteron intercalation. Furthermore, self diffusion of Hydrogen in TiO_2 was simulated showing diffusion rates comparable to those in fuel cell electrolytes.

Structure and dynamics of hydrogen in nanocomposite solid acids
Analogous to the electrolyte being the hart of the fuel cell, chapter 4 is the hart of the thesis. The chapter presents a wide array of techniques ranging from neutron diffraction to quasi elastic neutron scattering to nuclear magnetic resonance spectroscopy performed on a wide range of composite solid acids consisting of $CsHSO_4$ with TiO_2 or SiO_2 and the deuterated versions thereof. The presence and effects of nanostructuring on the solid acid $CsHSO_4$ with nanoparticulate proton accepting TiO_2 and SiO_2 were observed using these microscopic probes, as the mobility and mobile fraction of the protons were both much influenced at all temperatures probed.
Direct experimental proof of the occurrence of space charge effects in these nanocomposites was shown in the form of deuterium ion intercalation in TiO_2 nanoparticles together with deuterium depletion in the solid acid phase. Very high proton densities of up to 10% in the 7 nm TiO_2 particles have been found. These densities decrease as the particles sizes increase due to lower surface to volume ratios. The space charge effects in the crystalline bulk phase have been found to destabilize this phase, through observed increased rotational movement of the SO_4 tetraeders. This was attributed to weakening of the hydrogen bonded network as result of the physical removal of hydrogen. This destabilization also contributes to the with time increasing transformation of the crystalline phase to the X-ray amorphous phase.
The actual influences of the space charge effects on the mobility of the protons were observed using quasi elastic neutron scattering and nuclear magnetic resonance spectroscopy. QENS experiments showed fractions of up to 25% of the hydrogen ions at temperatures below the superprotonic phase transition to possess mobilities similar to the protons above this transition. NMR showed similar fractions as well as T_1 relaxation times of roughly 2 orders of magnitude shorter compared to the bulk

crystalline solid acids. Similar and consistent results have been found in the protonated and the deuterated samples.
Previously it was believed that only the amorphous phase contributes to the improvement in mobility and thus conductivity, however here it was shown that the crystalline part of the solid acid was directly influenced by the space charge effects as well. NMR experiments showed much shorter T_1 relaxation times of the protons in the crystalline phase of the composites compared to the protons of the bulk solid acid phase. Furthermore, a fully crystalline nanocomposite sample was shown to possess similarly short T_1 relaxation times compared to a with time mostly amorphisized nanocomposite sample, thus exhibiting a similar degree of mobility.
Further study into the morphological properties showed that the grain sizes of the solid acids in the composite samples were roughly a few times bigger than the added nanoparticulate material. These filler materials however, were present in large space filling quantities. This leads to the conclusion that the composites consist of relatively large solid acid grains, perforated by nanoparticles with an amorphous shell surrounding them. An explanation for these coherent domains of solid acids is spontaneous annealing of the material, which will be aided by the high intrinsic mobility.
The final conclusion from the neutron and NMR experiments concerning the induced ionic mobility due to nanostructuring was that because of the space charge effect, vacancies are created in the solid acid at temperatures below the superprotonic phase transition temperature. These empty sites allow a large fraction of the hydrogen ions to move, to such an extent that they become almost as mobile as in the superprotonic phase. This is however still limited to movement in a 2D network, as no phase transition has taken place. In the superprotonic phase the protons move through a 3D network of intrinsic vacancies. In the nanostructured materials increased mobility has already been found to occur 140 degrees lower compared to the bulk crystalline phase. This behaviour was also found to occur in the amorphous phase, as observed by NMR.

Polymer matrix

A composite electrolyte of solid acid $CsHSO_4$ and Nafion was synthesized by impregnation of the Nafion membrane with a solid acid solution. Optimal filling was achieved by using an amount of solid acid, which was 1.5 times the weight of the Nafion used. The Nafion pores were shown to be almost completely filled with solid acid. The fully transparent composite electrolyte membrane showed good mechanical strength and exhibited similar proton conductivity to pure Nafion at low temperatures in a humid environment. Furthermore, the composite membrane showed high conductivity of 10^{-3} S/cm at intermediate temperatures around 140 °C, where Nafion filled with water is inoperable. The conduction mechanism showed two processes as a result of conduction through the solid acid and along the Nafion

internal surface. The solid acid appeared to be fully X-ray amorphous in the composite. The advantages of this membrane are its straightforward synthesis and its operation with sufficient conductivity above the boiling point of water.

Cesium Dihydrogen Phosphate and acidity

The effects of nanostructuring on the conductivity have been attributed to the presence of space charges, shown for the $CsHSO_4$ composites. The investigation is further extended to another solid acid: Cesium dihydrogen phosphate CsH_2PO_4. Composites of this solid acid and nanoparticulate TiO_2 or SiO_2 were synthesized and studied using the same techniques and compared to the $CsHSO_4$ composites.

The huge improvement in conductivity of the CsH_2PO_4-SiO_2 composites at low temperatures has been found to be mainly due to the increased amount of mobile protons. Such a large increase in the amount of mobile protons is possible because all of the solid acid phase in the composite is influenced by the nanostructuring. Acidity was found to be indicative for the amount of space charge occurring. SiO_2 was found to be a better proton acceptor than TiO_2 and $CsHSO_4$ is a better proton donor than CsH_2PO_4. The results indicate a reduced space charge effect in CsH_2PO_4-TiO_2 composites consistent with the reduced acidity of CsH_2PO_4 and lower proton accepting capacity of TiO_2 compared to SiO_2. Using the acidity combined with computer calculations might be a useful way to predict the extent of space charge in future research towards the optimal combination for electrolyte membrane material.

Samenvatting

De overgang naar duurzame energie bronnen is onvermijdelijk. Indien waterstof een onderdeel uitmaakt van dit scenario, zullen brandstofcellen een zeer belangrijke rol spelen voor het converteren van de waterstof naar electriciteit. Er is echter nog veel ruimte voor verbetering in de brandstofcel technologie. Opgemerkt moet worden dat gedurende onze discussie over de brandstofcel, de toepasbaarheid voor de automobiel industrie in het achterhoofd is gehouden. Een volgende stap in de verbetering van de brandstofcel is het realiseren van de zogenaamde intermediaire temperatuur brandstofcellen. Huidige brandstofcellen gebaseerd op polymeer elektrolyten zijn genoodzaakt de bedrijfstemperatuur onder de 100 °C te houden door de inherente beperking van het geleidingsmechanisme van het elektrolyt, dat de aanwezigheid van vloeibaar water vereist.
Zuren in vaste fase, de zogenaamde solid acids zijn veelbelovende materialen voor toepassing als brandstofcel elektrolyten door hun hoge protonen geleiding bij intermediaire temperaturen van kamertemperatuur tot 250 °C. Een groot probleem bij deze solid acids is de lage protonen geleiding bij temperaturen onder hun superprotonische faseovergang. Het nanostructureren van deze materialen biedt de oplossing en verbetert de geleiding met ordes van grootte. Het mechanisme hierachter is nog onder discussie en microscopisch is er niet veel bekend over dit optredende fenomeen. Er is weinig literatuur over microscopische experimenten of fysische verklaringen hiervoor.
Dit proefschrift presenteert een multi-techniek aanpak, waarbij een verscheidenheid aan technieken is gebruikt om op moleculair of microscopisch niveau inzicht te verkrijgen in deze materialen en de betrokken processen. De solid acids $CsHSO_4$ en CsH_2PO_4 met nanodeeltjes TiO_2 of SiO_2 zijn bestudeerd, zowel in geprotoneerde als in gedeutereerde vorm. De TiO_2 nanodeeltjes bestaan uit de groottes 40 nm, 24 nm, 15 nm en 7 nm en de SiO_2 nanodeeltjes variëren in de groottes 40 nm en 7 nm. Structurele informatie is verkregen door het toepassen van Röntgen diffractie en Neutronen diffractie. Informatie over de dynamica is verkregen middels Quasi Elastische Neutronen Verstrooiing en Nucleaire Magnetische Resonantie spectroscopie naast Dielectrische Impedantie spectroscopie. *Ab initio* berekeningen, gebruik makend van het pakket VASP, zijn uitgevoerd om inzicht te krijgen in zowel structuur als dynamica. Deze technieken zijn gekozen voor hun gevoeligheid en vanwege hun complementaire aard om op lokaal (microscopisch) niveau verschillende lengte- en tijdschalen te bestuderen.

Deuterium intercalatie in TiO_2 anatase nanodeeltjes

Spontane waterstof dichtheid in nanodeeltjes is bestudeerd met neutronen diffractie op TiO_2 anatase nanodeeltjes met groottes van 24 nm en 7 nm gemengd met vloeibaar D_2SO_4. Vloeibaar D_2SO_4 is gebruikt, om het achtergrond signaal zo klein mogelijk te houden. In tegenstelling tot de vaste zuren, geeft vloeibaar D_2SO_4 namelijk geen complex diffractie patroon en de incoherente cross sectie van deuterium is relatief klein ten opzichte van waterstof.

De aanwezigheid van deuterium ionen in TiO_2 is waargenomen op de positie [0.00, 0.75, 0.43], wat overeen komt met een gespleten positie van de deuterium ionen in de zuurstof octaëder. *Ab initio* modellering laat een vergelijkbare positie zien. De bezetting van deze posities, verkregen uit data analyse via de Rietveld methode, vertaalt zich tot deuterium ion intercalatie van respectievelijk 9% en 17% voor de 24 nm en 7 nm deeltjes. Lithium intercalatie gaat gepaard met een karakteristieke kleur verandering; TiO_2 wordt blauw door de aanwezigheid van elektronen van de lithium ionen. Bij de intercalatie van het zuur is geen kleurverandering opgemerkt, wat erop wijst dat er geen elektronen meegaan met de deuterium ionen intercalatie. Verder is zelfdiffusie van H in TiO_2 gesimuleerd, wat diffusiesnelheden laat zien vergelijkbaar met de waardes in de brandstofcel elektrolyten.

Structuur en dynamica van waterstof in nanocomposiete solid acids

Analoog aan hoe het elektrolyt het hart is van de brandstofcel, is hoofdstuk 4 het hart van dit proefschrift. Dit hoofdstuk presenteert een breed scala aan technieken, variërend van neutronen diffractie tot quasi elastische neutronen verstrooiing tot nucleaire magnetische resonantie spectroscopie toegepast op een breed scala van composiet solid acids, bestaande uit $CsHSO_4$ met TiO_2 of SiO_2 en de gedeutereerde versies ervan. De aanwezigheid en effecten van de nanostructurering op $CsHSO_4$ met TiO_2 en SiO_2 zijn waargenomen met deze op microscopische schaal opererende technieken. Zowel de mobiliteit als de mobiele fractie van protonen zijn sterk beïnvloed door de nanostructurering bij alle gemeten temperaturen.

Direct experimenteel bewijs voor het optreden van space charge effecten in deze nanocomposieten is geleverd in de vorm van deuterium ion intercalatie in TiO_2 nanodeeltjes tezamen met het verdwijnen van deuterium in de solid acid fase. Zeer hoge protonen dichtheden tot 10% in de 7 nm TiO_2 deeltjes zijn gevonden. Deze dichtheden worden lager naarmate de deeltje groter worden door de lagere oppervlakte volume verhoudingen. De space charge effecten in de kristallijne bulk fase blijken de fase te destabiliseren, wat is opgemaakt uit de toegenomen roterende bewegingen van de SO_4 tetraëders. Dit is toe te schrijven aan het verzwakte netwerk van waterstofbruggen dat het gevolg is van het fysiek verwijderen van waterstof. Deze destabilisatie draagt ook bij aan de tijdsafhankelijke transformatie van de kristallijne fase naar de Röntgen amorfe fase.

De daadwerkelijke invloed van de space charge effecten op de mobiliteit van de protonen zijn bestudeerd met quasi elastische neutronen verstooiing en nucleaire magnetische resonantie spectroscopie. QENS experimenten laten fracties zien tot 25% van de waterstof ionen bij temperaturen onder de superprotonische faseovergang, die vergelijkbare mobiliteit vertonen als de protonen boven de superprotonische faseovergang. NMR liet vergelijkbare fracties zien en tevens T_1 relaxatie tijden van ongeveer 2 ordes korter vergeleken met de bulk kristallijne solid acids. Vergelijkbare en consistente resultaten zijn gevonden bij zowel de geprotoneerde- als de gedeutereerde materialen.
Eerder werd aangenomen dat enkel de amorfe fase bijdraagt aan de verbetering in mobiliteit en geleiding. Hier is aangetoond dat het kristallijne deel van de solid acid ook direct is beïnvloed door het space charge effect. NMR experimenten laten veel kortere T_1 relaxatie tijden zien van de protonen in de kristallijne fase van de composieten vergeleken met de protonen in de bulk solid acid fase. Verder bleek een volledig kristallijn nanocomposiet een vergelijkbaar korte T_1 relaxatietijd te bezitten als een grotendeels amorf nanocomposiet en aldus een vergelijkbare mate van mobiliteit te vertonen.
Verdere studie in de morfologische eigenschappen laat zien dat de korrelgrootte van de solid acids in de composieten grofweg een aantal malen groter is dan de toegevoegde nanodeeltjes. Echter, dit vulmiddel is aanwezig in zeer grote hoeveelheden. Dit leidt tot de conclusie dat de composieten bestaan uit relatief grote solid acid korrels, geperforeerd door nanodeeltjes omhuld met een amorfe schil. Een verklaring voor deze coherente domeinen van solid acids is spontane annealing, wat wordt vergemakkelijkt door de hoge intrinsieke mobiliteit.
De laatste conclusie die volgt uit de neutronen en NMR experimenten, betreffende de geïnduceerde mobiliteit van de ionen door nanostructurering, is dat door het space charge effect er vacatures zijn gecreëerd in de solid acid bij temperaturen onder de superprotonische fase overgangs temperatuur. Deze lege sites maken beweging voor een grote waterstof fractie mogelijk, in zulke mate dat deze vergelijkbare mobiliteit vertoont als de waterstof in de superprotonische fase. Deze bewegingen zijn echter beperkt tot het bestaande 2D netwerk, omdat er nog geen fase overgang heeft plaatsgevonden. In de superprotonische fase bewegen de protonen via een 3D netwerk van intrinsieke vacatures. In de nanogestructureerde materialen treedt toegenomen mobiliteit al 140 graden lager op ten opzichte van de bulk kristallijne fase. Dit gedrag geldt ook voor de amorfe fase, wat is aangetoond met NMR.

Polymeer matrix

Een composiete elektrolyt van solid acid $CsHSO_4$ en Nafion is gesynthetiseerd door impregnatie van de Nafion membraan met een solid acid oplossing. Een overmaat solid acid dat overeenkomt met 1.5 keer het gewicht van Nafion, resulteert in een

optimale vulling van het membraan met solid acid. De Nafion poriën zijn dan grotendeels geheel gevuld met solid acid. De volledig transparante composiet elektrolyt membraan bezit goede mechanische eigenschappen en vertoont een protonen geleiding vergelijkbaar met die van het pure Nafion bij lage temperatuur in een vochtige omgeving. Verder vertoont het composiet-membraan een hoge geleiding van 10^{-3} S/cm bij intermediaire temperaturen rond 140 °C, waar Nafion gevuld met water niet kan functioneren. Het geleidings-mechanisme bestaat uit twee processen, zijnde geleiding door de solid acid en langs het interne oppervlak van Nafion. De solid acid blijkt geheel Röntgen amorf te zijn in het composiet. De voordelen van dit membraan zijn het gemak van de synthese en het functioneren boven het kookpunt van water.

Cesium diwaterstof fosfaat en zuurgraad.

De effecten van nanostructurering op de geleiding worden toegeschreven aan de aanwezigheid van space charge, wat is aangetoond met de $CsHSO_4$ composieten. Het onderzoek is verder uitgebreid naar een andere solid acid, CsH_2PO_4. Composieten van deze solid acid en de nanodeeltjes TiO_2 of SiO_2 zijn gesynthetiseerd en bestudeerd met dezelfde technieken en vergeleken met de $CsHSO_4$ composieten.

De enorme verbetering in geleiding van de CsH_2PO_4-SiO_2 composieten bij lage temperaturen is hoofdzakelijk toe te schrijven aan de toegenomen hoeveelheid mobiele protonen. Een dergelijke toename is mogelijk doordat de gehele solid acid fase in het composiet beïnvloed is door de nanostructurering. De zuurgraad blijkt een indicatie te geven over de hoeveelheid space charge dat optreed. SiO_2 blijkt een betere proton acceptor dan TiO_2 en $CsHSO_4$ is een betere proton donor dan CsH_2PO_4. De resultaten wijzen op een verminderd space charge effect in CsH_2PO_4-TiO_2 composieten, consistent met de lagere zuurgraad van CsH_2PO_4 en de lagere capaciteit om protonen te accomoderen van TiO_2 ten opzichte van SiO_2. De combinatie van zuurgraad en computer berekeningen kan resulteren in een methode om de mate van space charge te voorspellen in toekomstig onderzoek naar de optimale combinatie voor elektrolyt membraan materialen.

Words of gratitude

After much consideration I came to the conclusion that there are so many people I want to express my gratitude to, that it would take many pages to do so. Therefore instead I have decided to start off with a general thanks to everyone who has contributed in one or another way to the realization of this thesis.

Naturally there are people to whom such a general thanks does not suffice. Most notably would be my promotor and daily supervisor Fokko Mulder. He has been very supportive and patient. Fokko was always enthusiastic and very optimistic. I'm glad I had him as my guide.

During my research I have had fruitful collaborations with Mark Johnson from the Institut Laue-Langevin, Stephen Picken from Delft Chem Tech and Ernst van Eck and Arno Kentgens from the department of Physical Chemistry at the Radboud University in Nijmegen. I would like to thank them and the people from the corresponding institutes for their help. Additionally I would like to thank Don Kearley, who was my promotor during the first part of my PhD and Ignatz de Schepper who, for a period of time, also was involved in my research.

It was always nice to be in the hall of FAME (and NPM2). Even more so after Ekkes arrived with his group. At the secretary, there was Marianne and later Nicole, Ellen and Ilse. I could always go to Michel if I needed something for the lab or the X-ray machine. Computer problems were always solved by Jouke and with scientific questions I could always bother Marnix or anyone from the staff. Enrique was a great consultant not only scientifically, but also on topics such as inburgering and babies. And so was Lian. There have been lots of master and PhD students and some postdocs I had contact with. Some left already like Wouter, Sarita and Robert. Others have left but came back, like Lambert and Jeroen. David and Patel were unique experiences. Anna and Luana were always nice to talk to. Lunch with Swapna, Anca, Markus and Jose were enjoyable. As were the breaks at the coffeemachine. With Lucas I have shared the office and have had good scientific collaborations. Furthermore there was Deepak the expert and Ou who's too friendly. Both I have become good friends with. Of course there was also Dr. Ir. Van Heijkamp. I could fill a whole thesis writing about Leon.

Badminton has played a major role during my time in Delft. It was useful to relieve stress, it has kept me in shape reasonably well, but above all it was made a lot of fun by all the people. Here I want to thank my friends at badminton.

My family has been an important factor in my life. My parents have always been very understanding. They have supported me in more occasions than I can remember and in more ways than I can count. Creating the most ideal environment for me to do the things I want or need to do. My family consists of more members; my brother and his wife, my sister and her husband and my dear little niece and nephew Joey and Joeyin. They are all very important to me and I know I can count on them in times of need. Furthermore I need to thank my parents in law for many things, but especially for coming and taking care of Sven when I was busy finishing this thesis.

Last but not least are my wife Wing and my son Sven. Love you both very much.

About the author

Wingkee was born on February 18th 1977 in Hong-Kong and came to The Netherlands before the age of 2. He went to the primary school 'De Meerpaal' in Leiden and did his secondary school also in Leiden at the 'Louise de Coligny College', which later became the 'Da Vinci College'. During these years he also attended Chinese Saturday school in Leiden. After secondary school he went to Delft to study Chemical Engineering at the Delft University of Technology. In 2003 he started his MSc project at the department of Polymer Materials and Engineering working for Professor Stephen Picken and supervised by Dr. Adam Best. This very enjoyable period lead to his decision to do a PhD after his graduation in 2004.
He applied for a position in the group of Fundamental Aspects of Materials and Energy (FAME) at the Faculty of Applied Sciences of the Delft University of Technology in Delft. He got accepted and started his PhD in 2005, initially working for Professor Don Kearley and later for Professor Fokko Mulder. This thesis is the result of many pleasant years at the department of FAME.